LEAP: A BALLOON-BORNE SEARCH FOR LOW-ENERGY COSMIC RAY ANTIPROTONS

by

Anne Rosalie Myers Moats

A Dissertation Submitted to the Faculty of the

DEPARTMENT OF PHYSICS

In Partial Fulfillment of the Requirements
For the Degree of

DOCTOR OF PHILOSOPHY

In the Graduate College

THE UNIVERSITY OF ARIZONA

1 9 8 9

Order Number 8919046

LEAP: A balloon-borne search for low-energy cosmic ray antiprotons

Moats, Anne Rosalie Myers, Ph.D.

The University of Arizona, 1989

U·M·I
300 N. Zeeb Rd.
Ann Arbor, MI 48106

LEAP: A BALLOON-BORNE SEARCH FOR LOW-ENERGY COSMIC RAY ANTIPROTONS

by

Anne Rosalie Myers Moats

A Dissertation Submitted to the Faculty of the

DEPARTMENT OF PHYSICS

In Partial Fulfillment of the Requirements
For the Degree of

DOCTOR OF PHILOSOPHY

In the Graduate College

THE UNIVERSITY OF ARIZONA

1 9 8 9

THE UNIVERSITY OF ARIZONA
GRADUATE COLLEGE

As members of the Final Examination Committee, we certify that we have read the dissertation prepared by Anne Rosalie Myers Moats

entitled LEAP: A BALLOON-BORNE SEARCH FOR LOW-ENERGY COSMIC RAY ANTIPROTONS

and recommend that it be accepted as fulfilling the dissertation requirement for the Degree of Doctor of Philosophy.

Theodore Bowen	14 April 1989
Theodore Bowen	Date
Carl T. Tomizuka	14 April 1989
Carl T. Tomizuka	Date
Jose D. Garcia	14 April 1989
Jose D. Garcia	Date
Henry A. Hill	14 April 1989
Henry A. Hill	Date
Ke Chiang Hsieh	14 April 1989
Ke Chiang Hsieh	Date

Final approval and acceptance of this dissertation is contingent upon the candidate's submission of the final copy of the dissertation to the Graduate College.

I hereby certify that I have read this dissertation prepared under my direction and recommend that it be accepted as fulfilling the dissertation requirement.

Theodore Bowen	14 April 1989
Dissertation Director	Date

STATEMENT BY AUTHOR

This dissertation has been submitted in partial fulfillment of requirements for an advanced degree at The University of Arizona and is deposited in the University Library to be made available to borrowers under rules of the Library.

Brief quotations from this dissertation are allowable without special permission, provided that accurate acknowledgment of source is made. Requests for permission for extended quotation from or reproduction of this manuscript in whole or in part may be granted by the head of the major department or the Dean of the Graduate College when in his or her judgment the proposed use of the material is in the interests of scholarship. In all other instances, however, permission must be obtained from the author.

SIGNED Lynne Rosalie Myers Woates

ACKNOWLEDGMENTS

I would like to thank my major professor, Prof. Theodore Bowen. His love of Physics inspired me and his experience and knowledge guided me. He allowed me independence when I wanted it, gave me an extra push when I needed it, and, above all, patiently helped me when I asked for it.

I would also like to thank all the people who have helped me along the way. I thank Dr. R. Huffman for use of his optical equipment. I thank the members of the University of Arizona machine shop for their expert construction of the Cherenkov counter. I also extend my appreciation to the other members of the LEAP team: Dr. R. Golden, Dr. J. Ormes, Dr. R. Streitmatter, S. Stochaj, and all the others that assisted me during our long stay in Canada and Las Cruces, NM.

I also thank those that helped me here at the University of Arizona during the construction phase: P. Halverson, S. Syracuse and M. Damento.

Finally, the person who has supported me and helped me the most has been my husband, William, and to him go my deepest appreciation and thanks.

TABLE OF CONTENTS

TABLE OF CONTENTS--continued

LIST OF ILLUSTRATIONS

LIST OF ILLUSTRATIONS--continued

LIST OF ILLUSTRATIONS-continued

LIST OF TABLES

ABSTRACT

The LEAP (Low-Energy Antiproton) experiment is a search for cosmic-ray antiprotons in the 120 MeV to 1.2 GeV kinetic energy range. The motivation for this project was the result announced by Buffington et al. (1981) that indicated an anomolously high antiproton flux below 300 MeV; this result has compelled theorists to propose sources of primary antiprotons above the small secondary antiproton flux produced by high energy cosmic-ray collisions with nuclei in the interstellar medium.

LEAP consisted of the NMSU magnet spectrometer, a time-of-flight system designed at Goddard Space Flight Center, two scintillation detectors, and a Cherenkov counter designed and built at the University of Arizona. Analysis of flight data performed by the high-energy astrophysics group at Goddard Space Flight Center revealed no antiproton candidates found in the 120 MeV to 360 MeV range; 3 possible antiproton candidate events were found in the 500 MeV to 1.2 GeV range in an analysis done here at the University of Arizona. However, since it will be necessary to sharpen the calibration on all of the LEAP systems in order to positively identify these events as antiprotons, only an upper limit has been determined at present. Thus, combining the analyses performed at the University of Arizona and Goddard Space Flight Center, 90% confidence upper limits of 3.5×10^{-5} in the 120 MeV to 360 MeV range and 2.3×10^{-4} in the 500 MeV to 1.2 GeV range for the antiproton/proton ratio is indicated by the LEAP results.

LEAP disagrees sharply with the results of the Buffington group, indicating a low antiproton flux at these energies. Thus, a purely secondary antiproton flux may be adequate at low energies.

CHAPTER 1

INTRODUCTION

On August 21, 1987, the balloon-borne LEAP (Low Energy Antiproton) experiment was launched from Prince Albert, Canada, for a 20 hour flight at 119,000 feet. During this flight, the cosmic-ray antiproton flux in the 120 MeV to 1.2 GeV kinetic energy range was measured with an experimental setup that included the New Mexico State University (NMSU) magnet spectrometer, a time-of-flight system designed and built by the high energy astrophysics group at Goddard Space Flight Center (GSFC), and a Cherenkov counter, designed and built by our group at the University of Arizona. In this dissertation, I will describe the design and performance of the Cherenkov counter in the context of the overall experiment. This description appears in Chapter 5. This counter was indispensible to the identification of antiprotons above 500 MeV, since the time-of-flight system was not sufficiently accurate at those energies to separate antiprotons from the lighter cosmic-ray cascade background particles. Thus, a portion of the data analysis, specifically the 500 MeV to 1.2 GeV kinetic energy range data, was performed here at the University of Arizona. In addition, the Cherenkov counter served as a veto for the analysis of the lower energy data and I will discuss this in a summary of the data analysis performed at GSFC. In Chapter 6 I will discuss the analysis and the results that have been obtained to date. In the final chapter, I will discuss the implications of these results.

But, to fully appreciate these implications, I will first summarize the previous antiproton searches in this general energy range (Chapter 2) and briefly sketch the

conventional model of collisionally-produced secondary antiprotons and the sources of possible primary antiprotons in Chapters 3 and 4. These sources were originally proposed in an attempt to reconcile the surprising results of Buffington, Schindler, and Pennypacker (1981) that disagreed with the general theory that the low-energy antiproton/proton ratio should be less than 10^{-5}. Thus, the main impetus for the LEAP experiment was just that result and the scarcity of measurements of low-energy antiprotons.

CHAPTER 2

THE SEARCH FOR LOW-ENERGY COSMIC RAY ANTIPROTONS PRIOR TO 1987

2.1. Nuclear Emulsion Searches

Most of the early searches for galactic antiprotons used nuclear emulsions. Two examples are the experiments of Apparao et al. (1967; 1985) (a 1962 flight) and Rao and Yock (1987) (a 1963 flight). These were flown during a solar minimum, just as LEAP was flown during the solar minimum of 1987 in order to measure the low-energy flux during a period of maximum penetration of low-energy particles.

In both of these experiments, an emulsion stack is the main detecting device. In the case of Rao and Yock, for example, 71 plates, each 15 cm x 15 cm x 625 micrometers, of Ilford G-5 emulsion was the experimental stack. Antiproton annihilation stars were searched for at a depth of 3.5 cm to 4.5 cm from the top edge of the stack. Antiproton events appeared as one black or grey track starting from the top of the stack and traveling downward (the flight direction obtained from the density change of each track along its path in the emulsion). The antiproton would then annihilate in a collision with a nucleus in the emulsion, emitting several fast large-angle tracks in a characteristic annihilation star. The mass of the possible antiproton track was determined by the grain density of each possible antiproton track at two points along the track separated by a constant distance. These densities and the rate of change of these densities were compared to the calibrated results of the same grain density changes of proton tracks. Proton

tracks were identified as the tracks that emerged from various interaction stars and stopped in the stack after a two centimeter or longer path.

In the experiment of Rao and Yock, four possible annihilation events were seen. However, all four were identified as high-energy alpha particle events. Thus, no antiproton events were seen in that experiment, just as no antiproton events in 3000 proton events were seen in the experiment of Apparao et al. except for one secondary antiproton (a product of an interaction within the emulsion itself). Thus both experimental groups only obtained upper limits. In Rao and Yock's case, it was an upper limit of 3×10^{-3} for the antiproton/proton ratio in the 120 MeV to 220 MeV kinetic energy range. Apparao's group reported an upper limit of 3×10^{-4} for the antiproton/proton ratio in the 100 MeV to 150 MeV kinetic energy range.

For these types of experiments, it is a grave handicap that other particles, such as alpha particles, can mimic antiproton events and there is no easy way to distinguish the true antiproton events. Since the antiproton flux is low, longer exposure time would be advantageous. The use of nuclear emulsions in balloon experiments would appear to be increasingly clumsy for these longer exposure times. Thus, hoping to be more sensitive, many of the newer experiments employed different methods.

Two experimental groups then went on to use magnetic spectrometers to look at the antiproton flux at slightly higher energies.

2.2. Magnetic Spectrometer Experiments

A series of high-altitude balloon experiments were carried out by a group headed by E.A. Bogomolov in the 1970's (Bogomolov et al. 1971; 1979) and more

recently during the summers of 1984-1985 (Bogomolov et al. 1987). In the most recent flight, his group searched for the primary antiproton flux in the 200 MeV to 5 GeV kinetic energy range using a magnetic spectrometer which employed a 100 kilogram permanent magnet with a gap volume of 5 x 15 x 34 cm^3 and average bending power of 7.3 x 10^4 gauss cm. To trace the particles' trajectories in the magnetic field, the Bogomolov group used four spark chambers viewed through a lens and mirror system by two cameras. Each spark chamber had four gaps and was filled with neon to 1.2 atmospheres. To determine the identity of the detected particles, they used a series of scintillating detectors and two Cherenkov counters - a gas counter filled with ethylene at 15 atmospheres and a lucite counter. The gas Cherenkov counter was used much in the same way ours was used (see Chapter 5). Basically, particles lighter than protons in the apparent kinetic energy range of interest for antiprotons radiated at nearly the maximum Cherenkov light intensity, while protons (and antiprotons) radiated very little light. In the case of Bogomolov et al., this gas Cherenkov counter was then used as a veto. The lucite Cherenkov counter was used to select singly-charged particles and, with its position at the bottom of the experimental stack, eliminated albedo protons (protons traveling upwards through the balloon gondola) using time-of-flight analysis. The geometric factor of the telescope was rather small (about 1.1 cm^2 sr), but a number of flights were undertaken.

In the summer of 1970, three flights with a total flight time of twenty hours were completed. 2850 proton and 22 possible antiproton events were gathered in the 2.3 - 5.2 GeV kinetic energy range, indicating a possible antiproton/proton ratio of 1.1 x 10^{-2} as a 95% confidence level upper limit. After subtracting out the background due to gas counter inefficiency, the Bogomolov group reported an

antiproton/proton ratio of 3 (±3) x 10^{-3}.

Then, in the mid-seventies, three more launches were made. A total of 3400 (±40) primary protons and 2 antiproton events were detected in the 2 - 5 GeV energy range, giving an antiproton/proton ratio of 6 (±4) x 10^{-4}.

Finally, during the summer of 1984 - 1985, four balloon flights for a total of 108 hours of flight time were accomplished. Since these flights were launched from beyond the polar circle where the earth's magnetic field did not preclude low-momentum particles, a lower energy range could be examined. In the 200 MeV to 2 GeV kinetic energy range, 17,800 galactic protons and one antiproton event were found in the data processed as of 1987. After correcting for atmospheric background, the resulting antiproton/proton ratio in the 200 MeV to 2 GeV range was 6 (+14/-5) x 10^{-5}. In the 2 to 5 GeV range, no antiproton events had been found among 2200 protons which, combined with the previous measurements, give an antiproton/proton ratio of 3 (+4/-2) x 10^{-4}. Their result in the 2-5 GeV range is shown in Fig. 1. Since the measurement below 2 GeV was not announced until the summer of 1987, I have shown the lower energy data in Fig. 40.

At a slightly higher energy range of 4.7 GeV to 11.6 GeV, R. L. Golden et al. (1979) also used a magnet spectrometer, employing in this case a superconducting magnet producing 10 - 40 kilogauss in the detector region. The geometric factor for the trigger was 315 cm^2 sr. The high altitude (5.4 g/cm^2) balloon was launched from Palestine, Texas, in June of 1979, reaching an altitude of 5.4 g/cm^2 of air. The trajectories of the particles were traced with eight multi-wire proportional counters (MWPCs). This magnet and MWPC set-up was also used in the LEAP experiment and is thus discussed in Chapter 5. The MWPC arrangement identified the charge sign and rigidity. Two scintillators (designated S1 and S2) were used to

determine the charge Z. A gas Cherenkov counter was used, as in the case of Bogomolov et al., to screen out the lighter particles. A set-up of seven scintillators (P1 - P7), each separated by 1.2 radiation-lengths of lead, isolated and identified electrons which would cascade in this stack. In addition, two of the scintillators (S1 and P7) determined the time-of-flight.

Antiprotons were isolated as the particles of negative charge (based on MWPC trajectory), heavy mass (based on the apparent rigidity in the magnetic field trajectory and time-of-flight or the absence of Cherenkov counter output), which did not cascade in the lead.

During this 1979 flight, 46 events were observed. Golden et al. estimated that of these, 11.1 events could be attributed to a general background of albedo protons, spillover of positively-charged events into the negative charge region during data processing, and nuclear interactions of other particles with the experimental apparatus. In addition, they estimated 6.5 of these events to be secondary antiprotons produced in the atmosphere above the experimental gondola in a process described in Chapter 3. That left 28.4 primary antiproton events, with an apparent antiproton/proton ratio of 5.2 ($\pm$1.5) x 10^{-4} in the kinetic energy region of 4.7 GeV to 11.6 GeV.

Later, Golden's group (Golden, Mauger, Nunn, and Horan, 1984) published results where the data set was divided into separate energy bins. Thus, they were able to obtain a more detailed antiproton spectrum, but with an increase in the uncertainty of the flux in each of these separate energy bins. Their results are also shown in Fig. 1.

2.3. Results of Buffington et al.

Then, a controversial and suprising result was reported by Buffington, Schindler, and Pennypacker (1981). They did not use a magnet spectrometer, but looked for the annihilation radiation of an antiproton - nucleus collision in a spark chamber using a selective trigger to bypass many of the particle identification problems encountered in nuclear emulsion experiments and enrich their data with antiproton candidates.

This selective trigger was composed of four scintillators and a solid plastic Cherenkov counter. Each trigger event was required to exceed threshold values in the four scintillators, without exceeding a set threshold on the Cherenkov counter. With such a trigger, only heavily-ionizing, massive particles such as protons and alpha particles could both satisfy the trigger and penetrate a significant distance into the spark chamber lead. However, it would take an interacting particle, such as an antiproton, in the lead to produce high-energy secondaries, mainly pions, that could penetrate to the lowest spark chamber after passage through the lead, and still not exceed the Cherenkov counter threshold. Thus, the data set was enriched in antiproton candidates. Buffington et al. estimated that 8% of the antiprotons in the 100 to 300 MeV range satisified this trigger while only one in 1000 cosmic ray events in general did so.

The lowest scintillation counter had to be penetrated by the pions produced by the antiproton's annihilation in the lead plates of the second spark chamber. This last scintillator could then be removed from the trigger in order to observe the proton flux.

After an event triggered the electronics, the event's passage through the two spark chambers was more thoroughly examined. The top spark chamber, containing

direction and eliminated multi-particle events. The bottom spark chamber, containing aluminum plates for the top four plates and lead plates for the subsequent plates, was the stage upon which each antiproton candidate must annihilate. These spark chambers were photographed by two cameras and the film was subsequently scanned for antiproton events.

This experiment was launced from The Pas, Canada (53 degrees north latitude), on June 18, 1980. This location was slightly farther north than the LEAP launch site (also 53.0° north latitude). Data was recorded for 18.4 hours of float time.

During the flight, 64 events produced a trigger and exhibited at least three-pronged interactions within the bottom spark chamber. However, all but 14 were eliminated as background due to events such as high-energy particle interactions with the gondola's side whose secondary products satisfied the trigger criteria, or a helium nucleus (later eliminated through the pulse height analysis of the scintillators), possible residual fragmentation contamination, etc. A correction factor of 1.2 was used to compensate for antiproton interaction and annihilation within the atmosphere above the balloon gondola (about 11 g/cm^2) and the material in the experimental stack. Thus, the antiproton flux, corrected to the top of the atmosphere, was calculated to be 1.7 ($\pm$ 0.5) x 10^{-4} m^{-2} sr^{-1} s^{-1} MeV^{-1}. Using a proton flux of 0.8 m^{-2} sr^{-1} s^{-1} MeV^{-1} from IMP-8 data, the Buffington group estimated the antiproton/proton ratio to be 2.2 ($\pm$ 0.6) x 10^{-4}, shown in Fig. 1.

This surprisingly high result (how surprising is discussed later) was controversial in several respects. One of the major objections is that many of the events had energies well below the geomagnetic cutoff rigidity of the launch site, although Buffington et al. felt that the quoted cutoff rigidities they used were

although Buffington et al. felt that the quoted cutoff rigidities they used were inaccurate.

Thus, the experimental situation prior to 1987 is shown on Fig. 1. Relatively few measurements of the primary antiproton flux at the top of the atmosphere had been undertaken in this low-energy range. Interest in this lower energy range had been small since it was assumed that any antiprotons observed would simply be secondary production of proton-proton collisions of cosmic-ray particles with the interstellar medium. However, the measurement of Buffington et al. was not consistent with that assumption and thus provoked an interest that in turn motivated us to begin the LEAP collaboration.

To see just how surprising Buffington et al.'s measurement was, I will now briefly summarize the conventional theoretical calculations of this antiproton flux that contrasts so sharply with Buffington group's result.

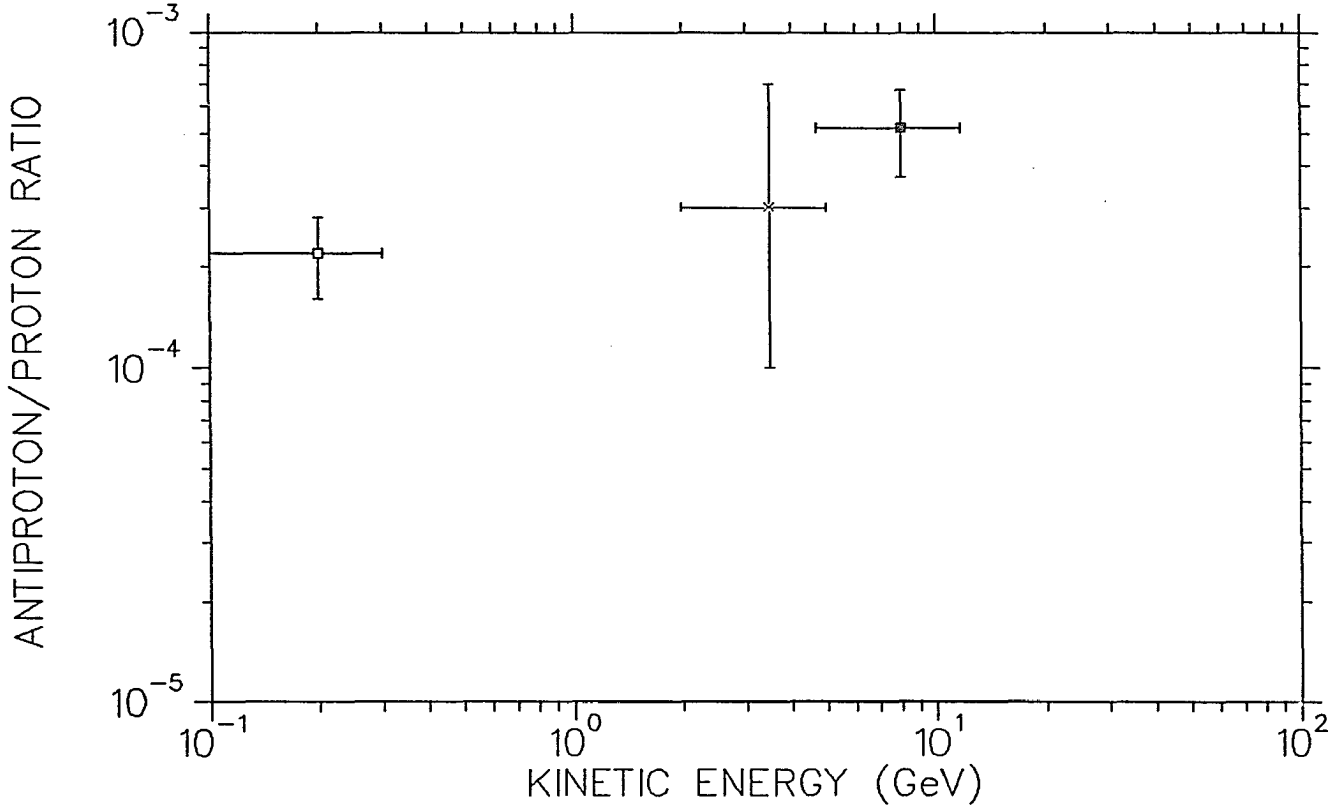

Fig. 1. Experimental measurements of the antiproton/proton ratio prior to 1987. The data are from Golden et al. (1979): filled square; Bogomolov et al. (1978): cross; Buffington et al. (1981): open square.

CHAPTER 3

SECONDARY PRODUCTION AND PROPAGATION OF COSMIC RAY ANTIPROTONS

3.1. In the Interstellar Medium

The conventional wisdom prior to 1981 was that the flux of low-energy antiprotons below several GeV should be very low. However, the antiproton flux was always believed to be finite since antiprotons would be present as products of the high energy collisions of cosmic ray particles with the hydrogen and helium nuclei present in the interstellar medium. In this section, I will outline the basic theoretical predictions of this conventional picture and show how the antiproton measurements discussed previously, especially the Buffington group's experimental results, challenge this picture.

Cosmic ray particles travel throughout the galaxy and exhibit a power-law spectrum that may extend to 10^{20} eV and perhaps beyond. These particles appear to be mainly protons with a 10% admixture of helium nuclei and an even smaller addition of most other nuclei found naturally in our solar system. Indeed, the abundances of each element in the cosmic-ray population seem to match fairly well these same abundances of elements found in the solar system and sun, with a few important exceptions. One such exception is the surprisingly high abundance of lithium, beryllium, and boron which naturally occur in low quantities in our solar system. Lithium, beryllium, and boron are normally depleted due to stellar fusion reactions. The usual explanation for the cosmic-ray enhancement (e.g. Juliusson, Meyer, and Müller, 1972; Smith et al., 1973; Juliusson, 1974; Caldwell, 1977; Simon

et al.,1980; Engelman et al., 1983) suggests that the relatively large population of lithium, beryllium, and boron occurs because they are the spallation products of carbon, nitrogen, and oxygen which do occur with some abundance in the cosmic rays. Thus, as cosmic ray particles travel through the interstellar medium, the lighter elements of lithium, beryllium, and boron are created in high energy collisions in the interstellar medium. Their abundance indicates that, on average, cosmic rays travel through 5 gm/cm^2 of material, although this pathlength may vary somewhat with energy. These elements give us some clues to the conditions present in the interstellar medium in which these high-energy collisions occur, producing among other particles - antiprotons.

The cosmic-ray proton spectrum is shown in Fig. 2. Usually, authors (e.g. Stephens, 1981) characterize this spectrum with a power law as follows:

$$\frac{dN_p}{dE_p} = N_0 E_p^{-\gamma} \tag{3.1}$$

with dN_p/dE_p as the differential proton spectrum, N_0 as a normalization factor, E_p as the proton kinetic energy. The factor γ is between 2.50 and 2.75. Most researchers believe that γ may be 2.65 to 2.75 at energies below 10^{15} eV and steepen to a γ of 3.0 to 3.5 for higher energies (Hillas, 1983). The shape of the spectrum at lower energies, below a few GeV, is much modified by the solar wind in our solar system (discussed in the next section). It is a reasonable approximation to assume that the shape of the spectra for higher Z nuclei are similar in shape to the proton spectrum. Thus, the differential spectrum for all cosmic rays can be approximated as

$$\frac{dN}{dE_p} = \delta\ N_0 E_p^{-\gamma} \quad . \tag{3.2}$$

δ is a numerical factor that will include these higher Z nuclei. δ is usually between 1.10 and 1.30. As one example, Stephens (1981) uses

$$\frac{dN}{dE_p} = (7.25 \times 10^3)\ E_p^{-2.50} \text{ for } 10 \text{ GeV} \leq E_p \leq 60 \text{ GeV} \quad ,$$

$$\frac{dN}{dE_p} = (2.0 \times 10^4)\ E_p^{-2.75} \text{ for } E_p > 60 \text{ GeV} \quad . \tag{3.3}$$

As the protons and other nuclei travel through the interstellar medium (ISM), antiprotons are produced in high-energy collisions of these cosmic-ray nuclei with the nuclei of the ISM. The majority of these reactions are p - p collisions, although nuclei of higher Z (and A) can also be involved. However, for simplicity, I will refer to these reactions as p - p collisions. The products of these collisions include nucleon - antinucleon pairs. Among these products are the secondary antiprotons and antineutrons (which decay in about 15 minutes to antiprotons). Thus, a small population of antiprotons are produced in this fashion in the ISM.

The production spectrum of these antiprotons are calculated using the invariant antiproton production cross section

$$\left[E_T\ \frac{d^3\sigma}{dP^3}\right]_{\bar{p}} \quad .$$

Here, E_T is total energy and P is momentum. Usually, authors (Tan and Ng, 1983; Gaisser, 1982; Gaisser and Maurer, 1973; Stephens, 1981) will use a parameterization of a corresponding function that compares well with the accelerator

data of the antiproton production cross section in the p + p → $\bar{p}$ + [ ] reaction. For example, Tan and Ng employed the parametrization

$$\left[E_T \frac{d^3\sigma}{dP^3}\right]_{\bar{p}} = f(X_R) \exp\left[-\left[AP_{t,\bar{p}} + BP^2_{t,\bar{p}}\right]\right] \tag{3.4}$$

where $f(X_R)$ is a function of X_R (the ratio of the antiproton total energy in the center-of-mass-system (CMS) and the maximum antiproton energy possible in the collision). $P_{t,\bar{p}}$ is the antiproton transverse momentum and A and B are functions of X_R. Then, the differential antiproton production cross section is calculated as

$$\frac{d\sigma_{\bar{p}}(E_{\bar{p}}, E_p)}{dE_p} = 2\pi \int_{\theta_{\bar{p}\,min}}^{\theta_{\bar{p}\,max}} P_{t,\bar{p}} \left[E_T \frac{d^3\sigma}{dp^3}\right]_{\bar{p}} d\theta_{\bar{p}} \quad . \tag{3.5}$$

Here, $\theta_{\bar{p}}$ is the antiproton angle in the lab system. This production spectrum integrated over all cosmic-ray energies is shown in Fig. 3. Of course, this is simply one of many such calculations, but the idea in all of these is the same: calculate a production spectrum from a curve that matches accelerator data for p + p collisions and use various scaling techniques to extend this function to the high energies attainable in cosmic rays.

Once these antiprotons are produced, several processes act upon this original spectrum to modify it. First, these antiprotons could escape from the galaxy. In the conventional leaky box model of cosmic ray propagation, protons and other cosmic ray particles are somewhat trapped in the galaxy by the galactic magnetic field. The particles spiral about the magnetic field lines and are thus trapped if

they possess a relatively low energy where their gyration radius is much smaller than the galactic radius. Escape can occur if random scattering allows the particle to leave the galactic magnetic field. The amount of time a particle is trapped is characterized by an escape time τ_{esc}. The presence of daughter products in the cosmic ray spectrum, produced by the decay of radioactive nuclei, indicates that this confinement time is on the order of several million years. Another way of looking at this model is to picture these cosmic rays as traveling back and forth in a box. Each time these nuclei bounce off a wall, there is some fixed probability that the particle will pass through the walls and escape. Each particle will then travel a distance ℓ with a mean free path of λ_{esc}. As antiprotons are produced by high-energy cosmic ray particles, a quasi-steady state will eventually be reached within this leaky box.

There are of course, additional processes occurring which modify the antiproton production spectrum. As the antiprotons travel through the interstellar medium, some will annihilate with the nuclei of the interstellar medium; this reaction is characterized by the path length λ_{ann}. The antiprotons may also undergo inelastic, non-annihilation collisions in which they survive, but at a lower energy; this process is characterized by the length $\lambda_{inelastic}$. They also will suffer ionization energy loss, though at the higher energies involved and in the rarified material of interstellar space, this will be a relatively small effect.

Taking these reactions into account and after traveling through x amount of material in the ISM, the antiproton flux as a function of time at an energy E can be calculated (as adapted from Gaisser and Levy, 1974; Gaisser, 1982) as

$$\frac{dN_{\bar{p}}(E)}{dt} = \frac{-N_{\bar{p}}(E)}{\tau_{\bar{p},esc}} - \frac{N_{\bar{p}}(E)}{\lambda_{\tau,Reaction}}$$

$$+ \int_{E_0=E}^{\infty} \frac{1}{\tau_{p,inelastic}} \cdot \frac{1}{\sigma_{inelastic}} \cdot \frac{d\sigma_{\bar{p}}(E,E_0)}{dE} N_p(E_0)dE_0$$

$$+ \int_{E_0=E}^{\infty} \frac{1}{\tau_{\bar{p},inelastic}} \frac{dN_{\bar{p}}(E,E_0)}{dE} N_{\bar{p}}(E_0)dE_0 - V\left[\frac{dE}{dx}\right]\left[\frac{\partial N_{\bar{p}}}{\partial E}\right] . \qquad (3.6)$$

The first term is the loss of antiprotons through galactic escape. $\tau_{\bar{p},esc}$ is the antiproton escape mean lifetime. The second term is the loss of antiprotons through annihilation and collisional energy-loss to a lower energy E' < E. Here, $1/\tau_{\bar{p},Reaction} = 1/\tau_{\bar{p},ann} + 1/\tau_{\bar{p},inelastic}$. The third term is the production of antiprotons through p - p collisions. Here, $d\sigma_{\bar{p}}(E,E_0)/dE$ is the antiproton production cross section for producing an antiproton of energy E by a cosmic ray proton of energy E_0. The source spectrum of protons is represented by $N_p(E_0)$. The fourth term is the flux of antiprotons originally of energy E which collide with protons in the ISM inelastically, but survive at the lower energy E_0. The term $dN_{\bar{p}}(E,E_0)/dE$ is the probability that an antiproton possessing energy E will possess energy E_0 after the collison. Finally, the last term is the ionization energy loss that antiprotons suffer as they travel through the ISM. In the steady-state solution, $dN_{\bar{p}}(E)/dt = 0$.

Another way of looking at this process is in terms of the steady-state flux of antiprotons in the galaxy. Following (Tan and Ng, 1981; 1983), the quasi-steady state flux of antiprotons obeys the following equation:

$$\left[\frac{1}{\lambda_{esc}} + \frac{1}{\lambda_{\bar{p},Reaction}}\right] N_{\bar{p}} + \frac{d}{dE_{\bar{p}}}(IN_{\bar{p}}) = Q_{\bar{p}} \quad . \tag{3.7}$$

Here, $\frac{d(IN_{\bar{p}})}{dE_{\bar{p}}}$ is the ionization energy loss term; I is the ionization loss rate. $Q_{\bar{p}}$ is the total antiproton production term, including the collisionally-produced antiprotons

$$q_{\bar{p}}^{(1)} = 4\pi\rho_{ISM} \int_{E_{\bar{p}}}^{\infty} N_p(E_p) \frac{d\sigma_{\bar{p}}(E_{\bar{p}}, E_p)}{dE_p} dE_p \tag{3.8}$$

where $N_p(E_p)$ is the proton flux and $d\sigma_{\bar{p}}(E_{\bar{p}}, E_p)/dE_p$ is from equation (3.5). Also, $Q_{\bar{p}}$ takes into account those antiprotons lost through inelastic, non-annihilation collisions:

$$q_{\bar{p}}^{(2)} = \int_{E_{\bar{p}}}^{\infty} \frac{1}{\lambda_{\bar{p},inelastic}} \cdot \frac{dN_{\bar{p}}(E_{\bar{p}}, E'_{\bar{p}})}{dE_{\bar{p}}} N_{\bar{p}}(E'_{\bar{p}}) dE'_p \quad . \tag{3.9}$$

Thus, $Q_{\bar{p}} = q_{\bar{p}}^{(1)} + q_{\bar{p}}^{(2)}$. Note that equation (3.6) and equation (3.7) are equivalent.

Solving equation (3.7),

$$N_{\bar{p}}(E_{\bar{p}}) = \frac{1}{I(E_{\bar{p}})} \int_{E_{\bar{p}}}^{\infty} Q_{\bar{p}}(E'_{\bar{p}}) dE'_{\bar{p}}$$

$$\times \exp\left[-\int_{E_{\bar{p}}}^{E'_{\bar{p}}} \frac{dE''_{\bar{p}}}{I(E''_{\bar{p}})} \left[\frac{1}{\lambda_{esc}} + \frac{1}{\lambda_{\bar{p},inelastic}}\right]\right] \tag{3.10}$$

Thus, with either equation (3.6) or (3.7), it is possible to use parameterized accelerator data of the appropriate cross sections, with some judicious scaling to extend these data to the highest cosmic ray energies, to calculate the expected secondary antiproton spectrum. However, there is one complication at the lower energies ($\lesssim$ 2 GeV). At these energies, the adiabatic deceleration associated with the solar wind is appreciable for each cosmic-ray antiproton (and of course proton) which enters the solar system.

3.2. Solar Modulation

As cosmic-ray particles enter the sun's sphere of influence, they feel the effect of the solar wind - an outflowing of energetic particles from the sun's surface. These particles carry the sun's magnetic field with them, because the high conductivity of most astrophysical plasmas cause these plasmas to behave as fluids where the magnetic field lines are "frozen" into the fluid and are carried with the general flow. In typical astrophysical situations, the conductivity is on the order of 10^{15} s^{-1}. Although individual collisions of cosmic-ray particles are fairly rare, each cosmic-ray particle feels the scattering effect of the magnetic field irregularities carried outwards by the solar wind.

One form of the the general transport equation for cosmic-ray particles as they enter the solar cavity is (Jokipii, 1985)

$$\frac{\partial n}{\partial t} = \nabla \cdot [K \nabla n] - \nabla \cdot [nV] + (1/3) \nabla \cdot V \frac{\partial}{\partial p} (\alpha E n) \quad . \tag{3.11}$$

Here, n is the particle distribution function $n(P,r,t)$ and the flux $N = P^2 n$, where P is the particle momentum. The first term on the left, $\nabla \cdot [K \nabla n]$ represents the

inward diffusion of particles into the solar system. The diffusion coefficient K is affected by the scattering effect of the magnetic irregularities present in the solar magnetic field and the general shape of the sun's magnetic field as it is carried out by the solar wind. Thus, in reality, K is a tensor that shows the effect that the magnetic field's direction and magnitude has on diffusion in each direction. The second term adds in the effect of convection - the scattering centers are moving outward with the wind at a velocity V. Finally, the last term takes into account the general expansion of the solar wind. P is momentum, E is kinetic energy of the cosmic ray particle, and $\alpha = (E+2mc^2)/(E+mc^2)$ is approximately equal to 2 for low energies, 1 for high energies.

One additional note on K is that, at different points in the sun's 22-year magnetic field cycle, the various components of the tensor K will have different magnitudes. In addition, K will differ depending on the charge of the entering particle as each particle follows its own path through the solar system. If this effect is real, the antiproton flux would have been enhanced during the summer of 1987 by perhaps 18% (Perko, 1987). To date, it has been difficult to measure such an effect since the uncertainties in the measured cosmic-ray flux have been greater than the proposed effect.

Now, in general, equation (3.11) is very difficult to solve analytically in its present form. In 1987, Perko calculated the modulated antiproton flux using several simplifying approximations. He assumed a steady-state solution ($\partial n/\partial t=0$) in a spherically-symmetric model for the high energy case. In the steady state then, a balance is struck between the inward diffusion of cosmic rays and the outward pressure exerted by the solar wind. K is then a purely radial diffusion coefficient. Thus,

$$\frac{\partial n}{\partial r} + \frac{VP}{3K}\frac{\partial n}{\partial P} \cong 0 \quad . \tag{3.12}$$

The omni-directional cosmic ray distribution function is again **n**. The differential intensity $N=p^2n$. For the radial diffusion coefficient, Perko used

$$K = A\beta P_c \qquad \text{for } P < P_c$$

and

$$K = A\beta P \qquad \text{for } P > P_c \quad , \tag{3.13}$$

where A and P_c are constants for the diffusion coefficient. P is the particle momentum. These constants are determined at each point in the solar cycle from the measured proton spectrum.

Solving for the total energy E_T of an incoming cosmic-ray particle, he obtained the solution

$$E_T = P_c \, \ell n \, \frac{P_r+E_r}{P_c+E_c} + E_c + \frac{(R-r)V}{3A} \qquad \text{for } P_r < P_c$$

and

$$E_T = E_r + \frac{(R-r)V}{3A} \qquad \text{for } P_r < P_c \quad . \tag{3.14}$$

The constants P_c, E_c, and radius R are obtained at some reference point in the solar system. P_r, E_r, and r are the particle variables. Thus, here he obtained an analytical solution for the energy loss each particle suffers as it enters the solar system. To obtain the modulated spectrum, one needs only to substitute expression (3.14) for the energy into an interstellar particle spectrum.

It is evident, for energies below several GeV, an accurate accounting of the

sun's influence on the interstellar spectrum must be taken into account when comparing the sort of measurement attempted by LEAP to the theoretically expected interstellar spectrum.

3.3. In the Earth's Atmosphere

Once the interstellar spectrum of antiprotons modulated by the solar wind in the solar system enters the earth's atmosphere, the spectrum is further modified by collisions with the nitrogen, oxygen, and other molecules in the atmosphere. The antiprotons suffer the same ionization energy-loss, the same annihilating and non-annihilating inelastic collisions as in the interstellar medium. In addition, the same secondary antiproton production mechanism that operated in the ISM operates in the earth's atmosphere. Even though most of the antiproton measurements discussed in Chapter 2 were performed very high in the atmosphere, there was still some 5 to 11 gm/cm^2 of atmosphere directly above the experimental balloon gondolas and it is necessary to give some thought to the atmosphere's effect on the interpretation of these results.

In 1986, T. Bowen and I (Bowen and Moats, 1986) calculated the secondary antiproton spectrum produced from inelastic collisions by high-energy cosmic-ray protons with air nuclei. With special attention to the energy-loss processes, we calculated the antiproton spectrum as a function of depth, x, in the atmosphere.

In the calculations, we used a one-dimensional diffusion equation similar to equation (3.6) of the interstellar medium, necessarily with no galactic escape term, to calculate the vertical intensities. This is a reasonable approximation at depth x if the interaction secondaries have laboratory angles

$$\theta_{LAB} << \left[\frac{\lambda_{attenuation}}{x}\right]^{1/2} \quad .$$

At sea level, this requirement would translate to $\theta_{LAB} << 20^{o}$.

Two adjustable parameters were included to allow for inelasticity and charge exchange in nucleon-nucleus collisions. To obtain values for these parameters, we first calculated the proton spectrum as a function of atmospheric depth. Since experimental data for the proton differential intensities is abundant, we were able to adjust the parameters by comparing our computed curves with the published data. Then we could use these adjusted values of the parameters in our antiproton calculations.

For the differential proton intensities, the atmosphere was divided into "slabs" of equal thickness Δx; steps of 1 g/cm^2 were used. Starting at the top of the atmosphere, the proton and neutron intensities were calculated for each slab using the calculated values of the adjacent slab above as a starting point.

For our calculations, the primary spectrum of protons at the top of the atmosphere was assumed to have the form

$$N_p = 2.0\ (E_p + 2.15)^{-2.75}\ cm^{-2}s^{-1}sr^{-1}\ GeV^{-1} \quad . \tag{3.15}$$

Cosmic-ray nuclei with higher Z (possessing a similar spectral shape) were added with a geomagnetic cutoff rigidity corresponding to Z/A = 1/2; it was assumed that the constituent nucleons acted independently in the atmosphere. The vertical geomagnetic cutoff rigidity is that rigidity (basically momentum per unit charge) below which the earth's magnetic field would exclude those particles from reaching the earth's surface. Above the cutoff, the number of primary protons was

increased by 22% and the number of neutrons contained in the primary nuclei of the heavier cosmic-ray nuclei was 22% of equation (3.15). All protons and nuclei whose momenta were less than the vertical cutoff rigidity were excluded.

At the i + 1 step or slab, the proton intensity $N_p(E)$ and neutron intensity $N_n(E)$ for each energy interval ΔE was calculated using the following equations:

$$\text{(a)} \quad N(i+1) = N(i) + \frac{dN(E)}{dx}\,\Delta x \quad ,$$

$$\text{(b)} \quad \frac{dN_p(E)}{dx} = \frac{-N_p(E)}{\lambda_{inel}^{air}} - \left[\frac{dE}{dx}\right]\frac{\Delta N_p}{\Delta E} + \int_{E_0=E}^{\infty} \frac{1}{\lambda_{inel}^{air}} \frac{dN(E,E_0)}{dE}\,[(1-\alpha)N_p(E_0) + \alpha N_n(E_0)]dE_0$$

$$\text{(c)} \quad \frac{dN_n(E)}{dx} = \frac{-N_n(E)}{\lambda_{inel}^{air}} + \int_{E_0=E}^{\infty} \frac{1}{\lambda_{inel}^{air}} \frac{dN(E,E_0)}{dE}\,[(1-\alpha)N_n(E_0) + \alpha N_p(E_0)]dE_0 \quad , \qquad (3.16)$$

where all the values of n on the right-hand side of equation (3.16) are the values from the slab i above.

λ_{inel}^{air} is the inelastic mean free path for proton-air nuclei collisions, found by fitting a curve to data compiled by DiGiacomo, De Vries, and Peng (1980) of p - ^{12}C reaction cross sections, which were then scaled up to p - air reaction cross sections by a factor $(14.4/12.0)^{2/3} = 1.13$. Above 0.8 GeV. λ_{inel}^{air} was assumed constant and was scaled from p - ^{12}C data at 20 GeV (Bellettini et al., 1966).

The first term on the right-hand side of equation (3.16b) is the loss of protons

from that energy interval due to inelastic collisions. The second term is the loss of protons from an energy E to some lower energy E' due to ionization energy loss. The last term adds in the protons gained from inelastic collisions of higher-energy protons E' > E with air nuclei. As in previous equations, the term $dN(E,E_0)/dE$ is defined as the probability that a proton of initial energy E_0 will possess energy E after collision. A simple uniform distribution of nucleon energies after an inelastic collision was used. This distribution is shown in Fig. 4. The parameter ϵ, where $\epsilon/2$ is the average elasticity, was adjusted between 0 and 1 until the data was fitted to the experimental data; the final ϵ was found to be 0.9. Here, α is the probability of charge exchange in an inelastic collision. $\alpha = 0.333$ best fit the experimental data.

The equation for the neutron distribution $N_n(E)$ was analogous except for the omission of the ionization energy loss term for the neutrons.

These parameters α and ϵ were adjusted until the calculated proton spectra matched the experimental data for several altitudes quite well, as shown in Fig. 5. These same parameters α and ϵ were then used in the antiproton calculations. Using the same numerical method, the atmospheric secondary antiproton spectrum was calculated using the following equations:

(a) $$N(i+1) = N(i) + \frac{dN(E)}{dx}\,\Delta x \quad ,$$

(b) $$\frac{dN_{\bar{p}}(E)}{dx} = \frac{-N_{\bar{p}}(E)}{\lambda^{air}_{Reaction}} + \int_{E_0=E}^{\infty} \frac{1}{\lambda^{air}_{inelastic}} \cdot \frac{1}{\sigma^{air}_{inelastic}} \cdot \frac{d\sigma^{air}_{\bar{p}}(E,E_0)}{dE}\, N_{nucleon}(E_0) \cdot dE_0$$

$$+ \int_{E_0=E}^{\infty} \frac{1}{\lambda_{inel}^{air}} \cdot \frac{dN(E,E_0)}{dE} [(1-\alpha)N_{\bar{p}}(E_0) + \alpha N_{\bar{n}}(E_0)]dE_0 - \left[\frac{dE}{dx}\right] \frac{\Delta N_{\bar{p}}}{\Delta E} \quad ,$$

$$\text{(c)} \quad \frac{dN_{\bar{n}}(E)}{dx} = \frac{-N_{\bar{n}}(E)}{\lambda_{Reaction}^{air}} + \int_{E_0=E}^{\infty} \frac{1}{\lambda_{inelastic}^{air}} \cdot \frac{1}{\sigma_{inelastic}^{air}} \cdot \frac{d\sigma_{\bar{n}}^{air}(E,E_0)}{dE} N_{nucleon}(E_0)$$

$$dE_0$$

$$+ \int_{E_0=E}^{\infty} \frac{1}{\lambda_{inel}^{air}} \cdot \frac{dN(E,E_0)}{dE} [(1-\alpha)N_{\bar{n}}(E_0) + \alpha N_{\bar{p}}(E_0)]dE_0 \quad . \qquad (3.17)$$

The second term on the right-hand side of equation (3.17b) is the production spectrum for antiprotons in proton-air collisions; here we used the parameterization of Tan and Ng (1983). We assumed that the primary spectrum again includes Z greater than 1 nuclei, that the production of antineutrons is equal to antiproton production, and that both production spectra were attenuated with increasing atmospheric depth with a 122 g/cm^2 attenuation length $\lambda_{attenuation}$. The forms of the ionization loss (dE/dx) and the distribution function $dN(E,E_0)/dE$ were of the same form as used in the proton calculations.

$\lambda_{Reaction}^{air}$ is the antiproton mean free path in air for annihilation and inelastic scattering in antinucleon-nucleon interactions:

$$\frac{1}{\lambda_{Reaction}^{air}} = \frac{1}{\lambda_{ann}^{air}} + \frac{1}{\lambda_{inelastic}^{air}} \quad . \qquad (3.18)$$

We derived $\lambda_{Reaction}^{air}$ by scaling a power-law fit to antiproton - ^{12}C reaction cross sections (Bruge, 1984). $\lambda_{inelastic}^{air}$, the antiproton mean free path for inelastic, non-annihilation collisions, was fitted to the available accelerator data in three different

forms (see Fig. 6). However, the most realistic method used was curve a. To derive this estimate, we assumed that the cross section for p - p inelastic collisions was the same as for $\bar{p}$ - p inelastic, non-annihilation collisions, necessary since there is very little accelerator data available for fitting a curve to (Flaminio, 1984). We then assumed that

$$\bar{\lambda}^{air}_{inelastic} / \bar{\lambda}^{air}_{annihilation} = \sigma^{(\bar{p}\ p)}_{annihilation} / \sigma^{(\bar{p}\ p)}_{inelastic} \quad . \tag{3.19}$$

Below 0.5 GeV, $\bar{\lambda}^{air}_{inelastic}$ depends entirely on quasi-elastic antiproton-nucleon scattering; for our estimate for $\sigma_{inelastic}(\bar{p}\text{-air})$, the quasielastic scattering was taken to be 1/10 as probable as for the p - nucleon case (shown as curve c in Fig. 6), based upon Monte Carlo calculations using ISABEL INC for $\bar{p}$ - ^{12}C inelastic scattering at 180 MeV and 400 MeV (Clover, McGaughey, and Yariv, 1985; Clover et al., 1982). Fig. 6 shows our estimate for $\bar{\lambda}^{air}_{inelastic}$.

A short note on curves b and c, for completeness, is necessary to understand Fig. 6. Curve c assumes that $\bar{\lambda}^{air}_{inelastic}$ was equal to $\lambda^{air}_{inelastic}$, probably underestimating the antiproton-air inelastic mean free path, since the scattering process in $\bar{p}$ - p collisions must compete with annihilation and the $\bar{p}$ - p quasielastic scattering cross section is much less than for the pp case at large values of four-momentum transfer. Curve b uses an estimate by Szabelski and Wolfendale (1986).

The final results for low-energy antiproton fluxes are very sensitive to the uncertainty of $\bar{\lambda}^{air}_{inelastic}$ below 0.5 GeV.

Our calculations of the atmospheric secondary antiproton flux was calculated at each 1 gm/cm^2 step in atmospheric depth. At a mountain altitude of 747 g/cm^2, shown in Fig. 7, we compared our calculated antiproton flux estimate with a recent

antiproton measurement by the Arizona group (Sembroski et al.1986). Curves a and c are both consistent with the small amount of data available. This is encouraging, since at these low altitudes, virtually any observed antiprotons must be secondary, not primary, in nature. The atmospheric secondary antiproton flux at 5 and 11 g/cm^2 are also shown in Fig. 7. As can be seen, the atmospherically produced secondary flux is several orders of magnitude below that of measurements discussed in Chapter 2. Thus, we cannot discount these previous measurements as an atmospheric phenomenon, but as a real measurement of ISM antiprotons.

3.4. Expected Spectrum in the Energy Range 100 MeV to Several GeV

As stated previously, the expected secondary antiproton spectrum from a purely atmospheric source is shown in Fig. 7. At high altitudes of 5 to 11 gm/cm^2 typical of previous balloon measurements, this spectrum is quite low.

Various authors (Tan and Ng, 1983; Gaisser and Levy, 1974; Gaisser, 1982; Szabelski, Wdowczyk, and Wolfendale, 1980; Stephens, 1981) have also calculated the expected antiproton flux from secondary production in p - p collisions in the interstellar medium. Using various forms of the equations found in the previous sections, the secondary antiproton spectrum can be calculated with appropriate models and approximations. One of the most recent (Webber, 1987) is shown in Fig. 8. The effect of solar modulation on Webber's result is shown as the dashed spectra labeled as Perko. As can be seen, there is still some uncertainty in the theoretical predictions; most of this uncertainty appears as differences in the cross sections used. Most of the accelerator data must be extrapolated to very high energies in order to be useful in the interstellar medium calculations and the best way to do this is not always clear. In addition, uncertainties in the exact

interstellar cosmic-ray spectrum also plays a part. However, in all the calculations shown here, it is obvious that the secondary antiproton flux decreases rapidly at decreasing particle kinetic energies for kinetic energies much below a few GeV.

The reason for this agreement is the role that relativistic kinematics plays in the collision process. The antiprotons are produced as one pair of a nucleon-antinucleon pair, and thus can only be produced in highly relativistic collisions above the threshold for pair production. Thus, even when the secondary antiproton may have little kinetic energy in the center-of-mass frame, the secondary antiproton will still possess appreciable kinetic energy in the laboratory frame. Any secondary antiprotons observed below this kinematic limit must have undergone some deceleration (e.g. inelastic collisions). Thus, the secondary antiproton spectrum is not rich in low-energy antiprotons.

Also in this figure is shown the results of the Golden, Bogomolov, and Buffington groups. While Bogomolov's and Golden's data is arguably in some agreement with the predictions of the conventional leaky box model, Buffington's data point seems to be anomalously high. No decrease in the antiproton spectrum below the kinematic limit is apparent. If correct, this high flux of low-energy antiprotons cannot be explained easily by the conventional picture outlined in this chapter.

Several possibilities are evident. The data of Buffington et al. might not be correct; corroboration for this surprising result is needed: hence, the LEAP experiment. Second, our understanding of high-energy p - p reactions may not be correct. This possibility is not dealt with here. Or, thirdly, there may be, in the universe, a source of primary antiprotons which would produce this population of low-energy antiprotons.

After this surprising result, many theorists scrambled to model just such a source. Since the Buffington group's measurement stood alone for quite a few years, many models were proposed in that time. In this next section, I will outline a few of these theories to give an idea of the richness and variety of possible antiproton sources that were proposed because of this one lone result.

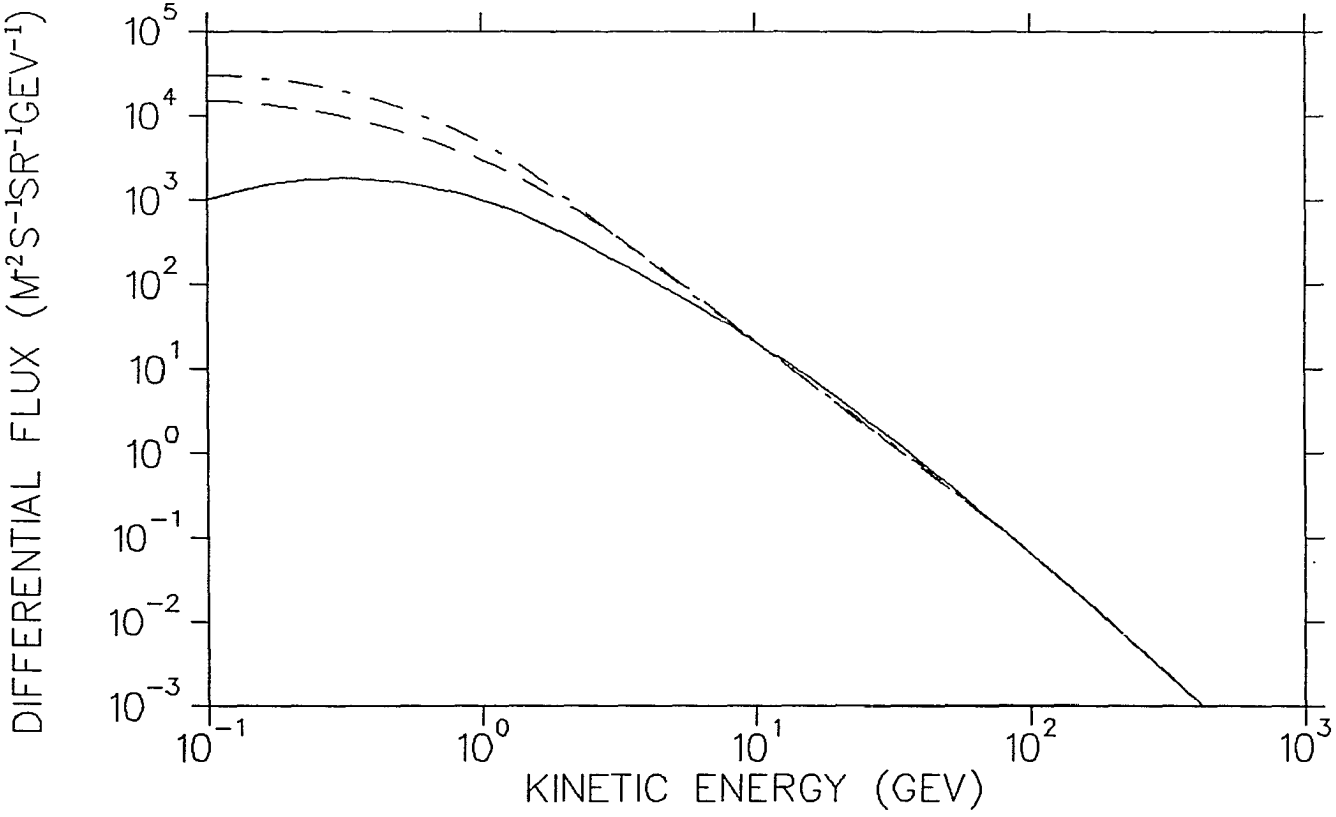

Fig. 2. The cosmic-ray proton spectrum observed during minimum solar modulation is shown with the solid curve. The other curves are the demodulated interstellar proton spectrum according to various models. This figure from Stephens (1981).

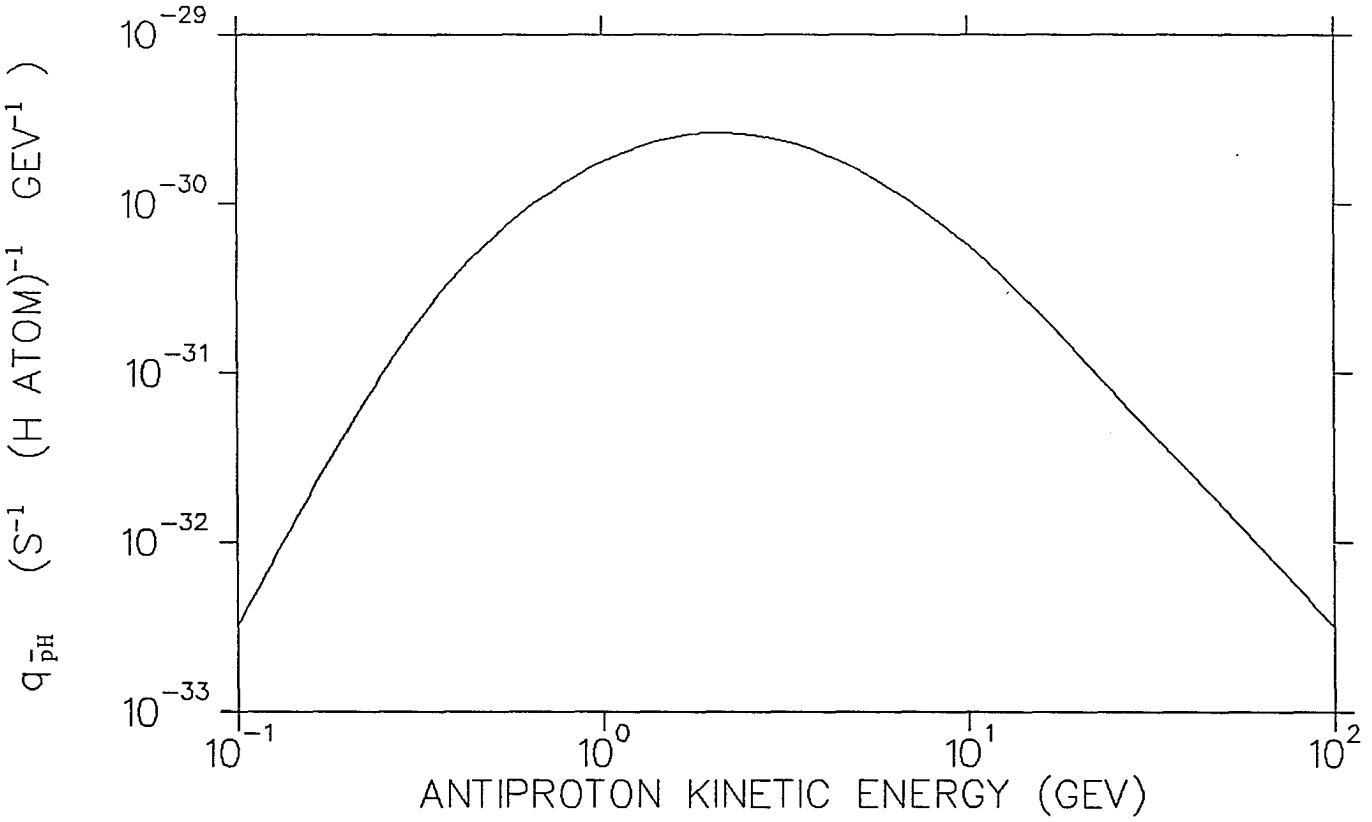

Fig. 3. The antiproton production rate, $q(\bar{p}H)$, as a function of the antiproton kinetic energy $T(\bar{p})$. From a calculation by Tan and Ng (1983).

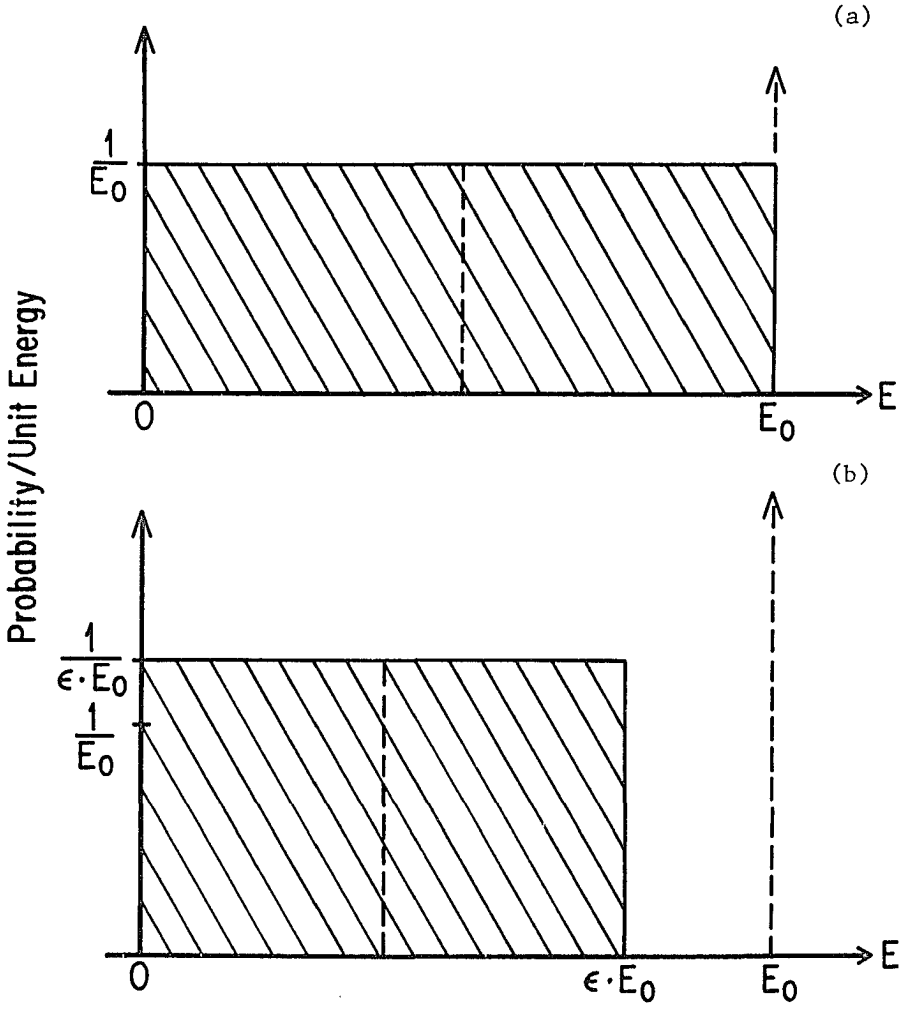

Fig. 4. (a) A simple uniform distribution of nuclear energies after an inelastic collision, with average elasticity of 1/2.
(b) The uniform distribution as modified by Bowen and Moats (1986) with average elasticity of epsilon/2.

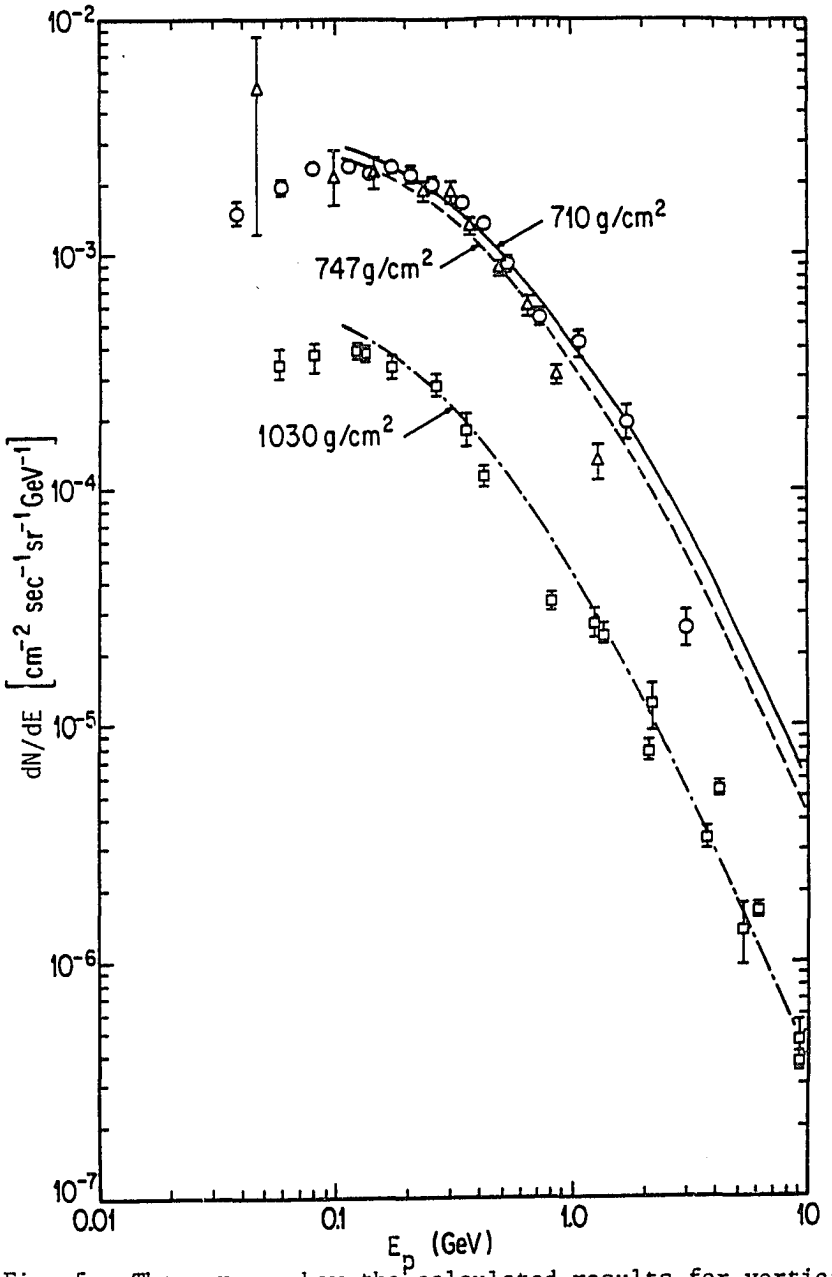

Fig. 5. The curves show the calculated results for vertical proton intensities at 710, 747, and 1030 g/cm^2 depth. The data are a compilation by Barber (1980). From Bowen and Moats (1986).

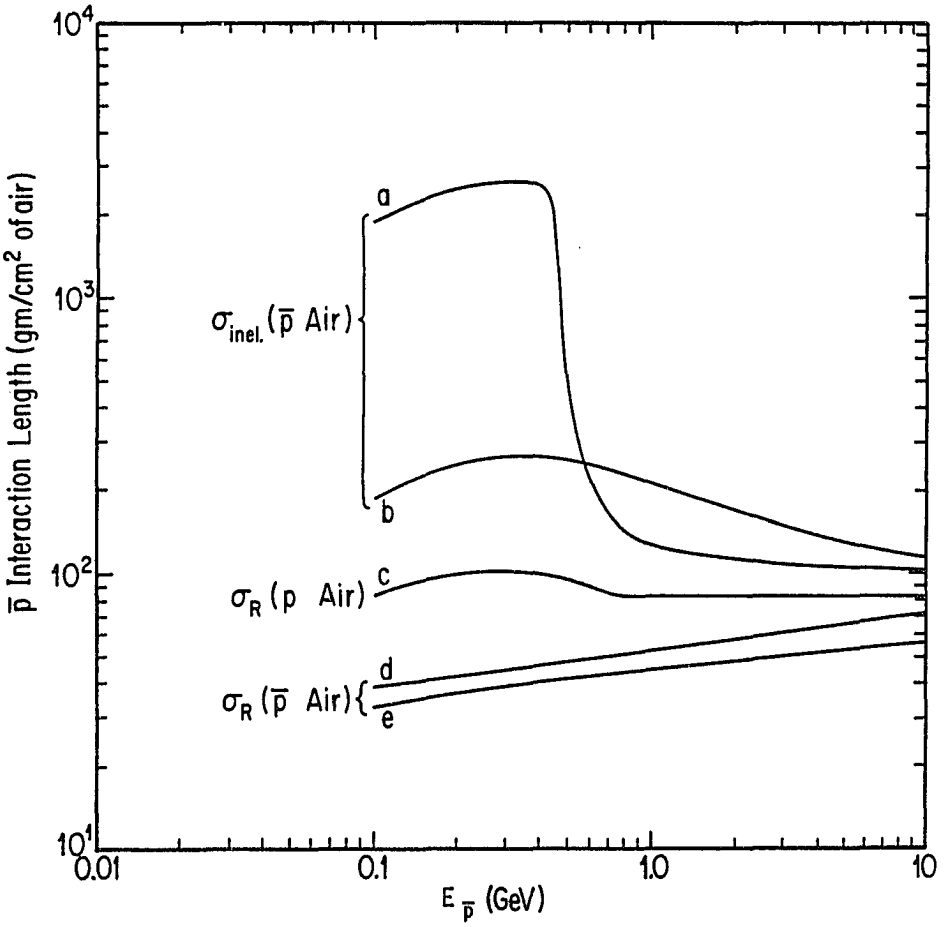

Fig. 6. Antiproton - air interaction lengths (mean free paths) employed in the calculations of atmospheric secondary antiprotons. Labeled curves are discussed in text. From Bowen and Moats (1986).

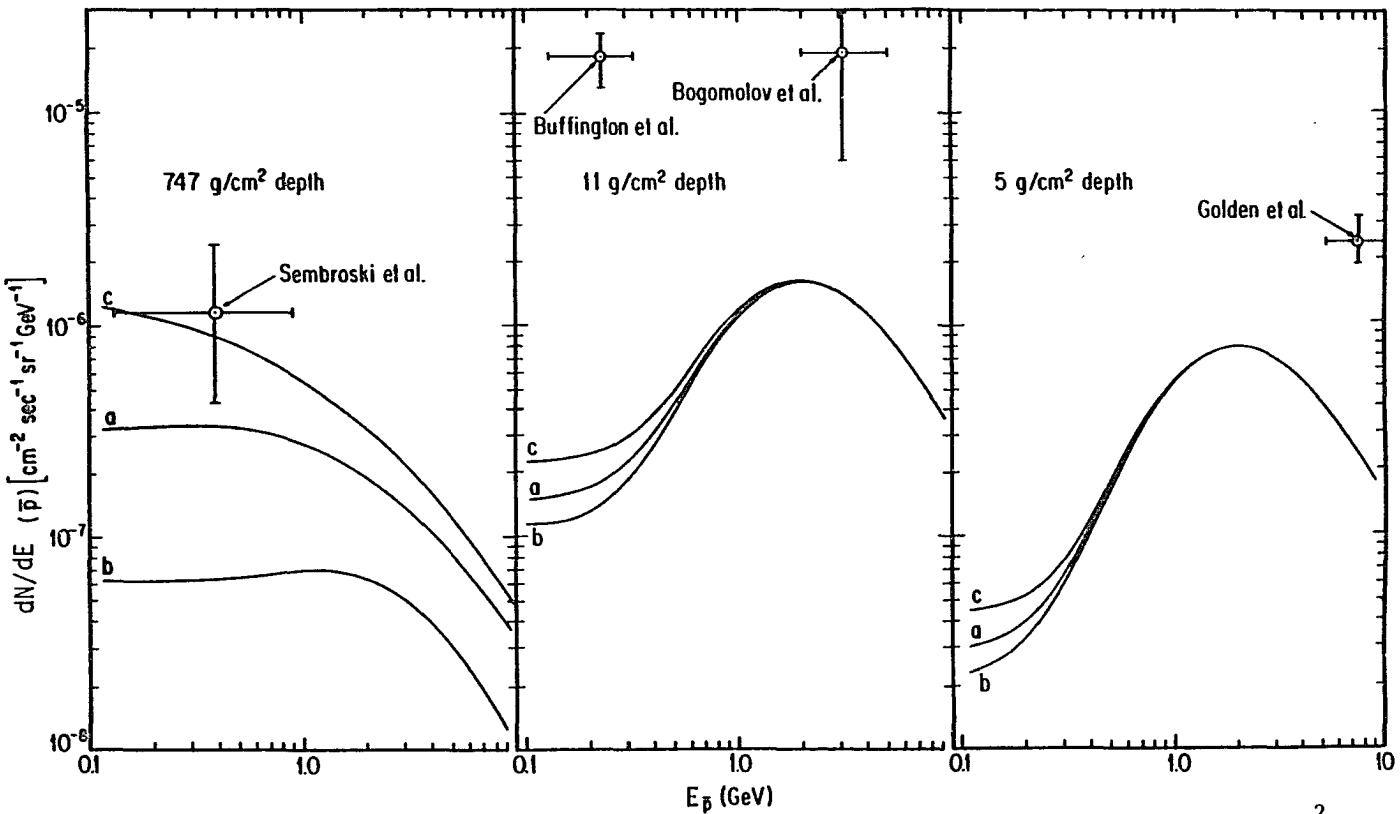

Fig. 7. The calculated atmospheric secondary antiproton intensities at 5, 11, and 747 g/cm^2. The curves a, b, and c are the same designation as for figure (6). The datum at 747 g/cm^2 is from Sembroski et al. (1986). This figure from Bowen and Moats (1986).

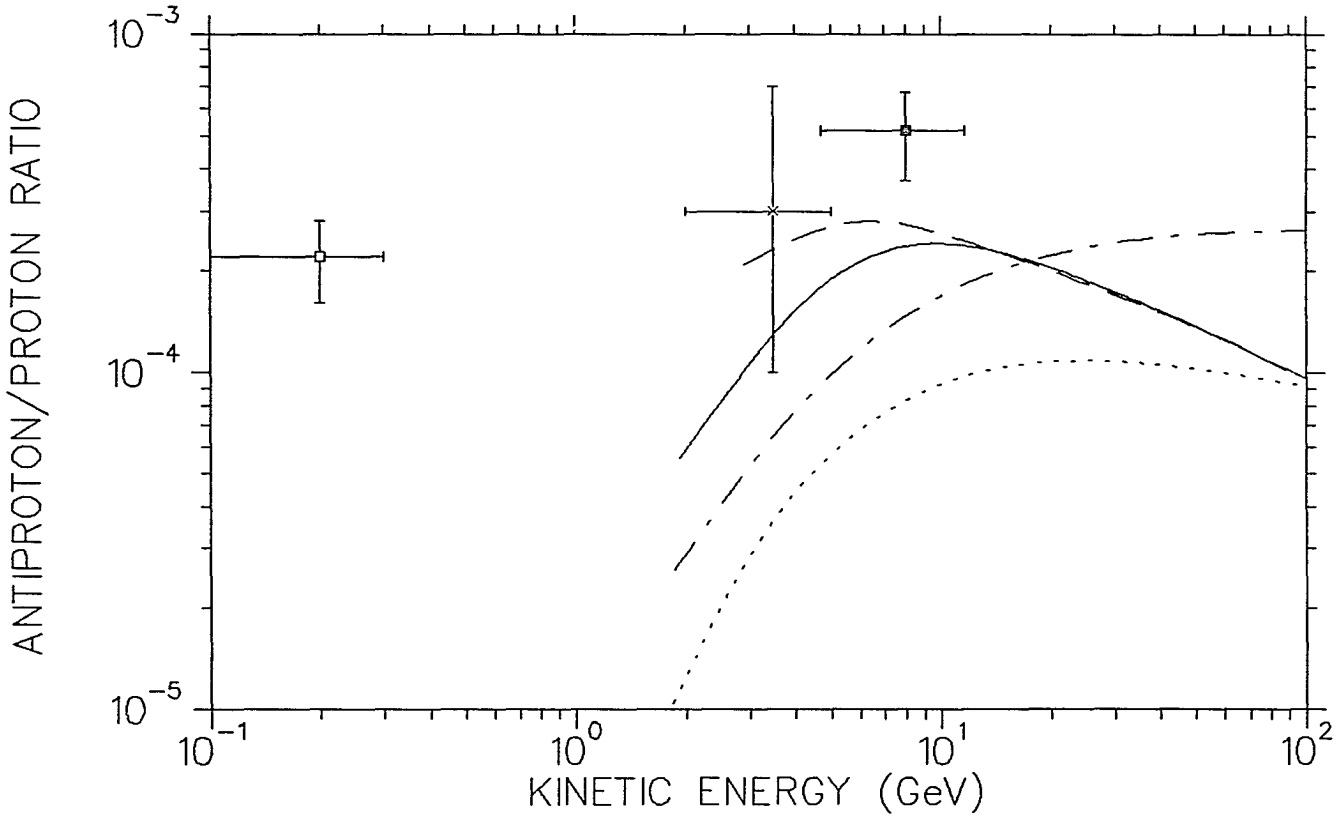

Fig. 8. Secondary antiproton/proton ratio as a function of kinetic energy. The theoretical curves are from: Webber (1987), solid line; effect of modulation from Perko (1987), dashed line; Stephens (1981), dot-dashed line; Protheroe (1981), dotted line. The experimental measurements are from figure 1.

CHAPTER 4

POSSIBLE SOURCES OF PRIMARY ANTIPROTONS

4.1. Production from Annihilation of Primordial Supersymmetric Particles

One of the most popular theories suggests that a substantial flux of low-energy antiprotons is a consequence of dark matter in galactic halos (Stecker, 1987; Rudaz and Stecker, 1988; Silk and Srednicki, 1984; Hagelin and Kane, 1986; Stecker, Rudaz, and Walsh, 1985). From the flat rotation curves of visible galactic matter in other spiral galaxies, it is reasonable to assume that a large proportion of the universe's matter is nonluminous, not directly observable to us. Since present estimates show that the visible universe has a matter density much lower than the closure density (density needed to eventually slow and stop the inflationary universe), it may be that this dark matter makes up the bulk of all matter.

This dark halo matter would have to be neutral, weakly interacting, massive particles. One class of candidates are the supersymmetric particles, the superpartners of ordinary constituent particles, postulated in extensions of the standard electroweak model of Glashow, Weinberg, and Salam (Glashow, 1961; Weinberg, 1967; Salam, 1968) where spontaneous symmetry breaking appears. These dark matter particles are fermions (spin 1/2), partners to ordinary matter bosons. For example, photinos, higgsinos, and zinos are the massive superpartners of the photon, higgs, and Z^0 particles. Additional dark matter candidates are the spin-0 sneutrinos, Dirac neutrinos, or Majorana neutrinos (Rudaz and Stecker, 1988). However, each of these either will not produce antiprotons in abundance or has some experimental evidence against their existence.

The lightest supersymmetric particle (some superposition of photino, higgsino, and zino states) will be stable, prevented from decaying because of conservation of R-parity. The lightest supersymmetric particle (LSP) will be the lightest state with odd R-parity. It is most probable that the lightest supersymmetric case is almost a pure photino state or a pure higgsino state. These photinos or higgsinos were created in the big bang, along with all the other supersymmetric particles. However, the heavier supersymmetric particles would have decayed, leaving only the lightest such particles as the missing matter in the galactic halos.

The only path of photino or higgsino "disappearance" throughout time would be annihilation with its own antiparticle. If the photino or higgsino mass m_x is only slightly greater than the quark mass, heavy hadrons containing a heavy quark are produced; the heavy quark will then decay with an antiproton as a by-product. If m_x is much greater than the quark mass, low momentum baryon-antibaryon pairs will be produced, producing antiprotons also. However, there are other branches in the annihilation reaction such as lepton $\bar{\tau}\ \tau$ production which do not result in antiproton production.

Assuming that either a photino or a higgsino makes up the missing matter in galactic halos and studying the quark jets in the analogous process

$$e^+ \ e^- \ \rightarrow \ \bar{p} \ + \ [\text{anything}],$$

various authors (e.g. Silk and Srednicki, 1984; Hagelin and Kane, 1984; Stecker, Rudaz, and Walsh, 1985) have calculated an antiproton spectrum due to these hypothetical particles. After S. Rudaz and F. W. Stecker, the production rate of antiprotons is

$$Q_{\bar{p}}(E_T) = n_x^2 \langle \sigma_x v \rangle_A \, f_{\bar{p}}(E_T) \quad , \tag{4.1}$$

where $f_{\bar{p}}(E_T) = dN_{\bar{p}}/dE_T$, normalized to the number of antiprotons produced per supersymetric particle-antiparticle annihilation, $\langle \sigma_x v \rangle_A$ is the annihilation cross section, and n_x is the number of supersymmetric particles in the halo. E_T is the antiproton total energy. With the decay being overwhelmingly domimated by τ lepton and $\bar{c}c$ and $\bar{b}b$ quarks in the final states,

$$\langle \sigma_x v \rangle_A = \frac{G_F^2}{4\pi} (m_\tau^2 + 3\, m_c^2 + 3m_b^2) \quad , \tag{4.2}$$

assuming $m_x > 15$ GeV and β_f or $\beta_{\bar{f}} \approx 1$. ($\beta_f$ is the supersymmetric fermion velocity.) The masses m_τ, m_c, m_b are the lepton and quark masses and the factor of 3 for color effects. Taking into account the quark masses, we get

$$\langle \sigma_x v \rangle_A = \frac{31}{4\pi} G_F^2 m_\tau^2 = 1.26 \times 10^{-26} \text{ cm}^3\text{s}^{-1} \quad . \tag{4.3}$$

The factor $f_{\bar{p}}(E_T) = dN_{\bar{p}}/dE = 2/\sigma_A \cdot d/dE\,(\sigma_{xx \to \bar{p}+X})$ (the factor of 2 from the production of antineutrons which decay into antiprotons) can be fitted by a function

$$\frac{1}{\sigma_A} \frac{d}{dx} (\sigma_{xx \to \bar{p}X}) = \frac{1}{\sigma_{e^+e^- \to h}} \frac{d}{dx} (\sigma_{e^+e^- \to \bar{p}X}) \qquad (X = \text{anything}) \tag{4.4}$$

from e^+e^- reactions. Here, $x = 2E/\sqrt{s}$ is the scaled antiproton energy. The CSM energy is $\sqrt{s}$. Then

$$f_{\bar{p}}(E_T) = 2.4\beta_{\bar{p}} (m_x)^{-1} [8.5\ e^{-11(E_T/m_x)} + 0.25\ e^{-2(E_T/m_x)}] \quad . \tag{4.5}$$

From equation (4.1) then, the interstellar flux is

$$N_{\bar{p}}(E_T) = (4\pi)^{-1} Q_{\bar{p}}(E_T) \beta_{\bar{p}} c\tau_{esc} = 2.5 \times 10^{-5} \beta_{\bar{p}}^2 K [8.5\ e^{-11(E_T/m_x)} + 0.25\ e^{-2(E_T/m_x)}]\ cm^{-2}s^{-1}sr^{-1}GeV^{-1} \tag{4.6}$$

with $K = (\rho_x/0.75)^2 (m_x/15)^{-3} [\tau_{esc}/2 \times 10^{15}]cm^{-6} (GeV)^3s$. Here, ρ_x is the lightest supersymmetric particle (LSP) mass density and τ_{esc} is the mean antiproton lifetime in the halo. Using different estimates for ρ_x, m_x, and τ_{esc} present in the various galactic and particle-physics models, the antiproton flux from LSP's can then be easily calculated. For one example, see Fig. 9.

For these calculations, after the decrease in the average energy of the antiprotons due to solar modulation effects are taken into account, a high flux of low-energy antiprotons in the energy range examined by the Buffington group would be expected. In addition, all of these spectra exhibit a cutoff at an energy that is at the kinematic limit of these annihilation reactions. Since no data is available at these higher energies, the data of Buffington et al. could then be construed as some indication that these low-energy antiprotons from photino or higgsino annihilations were being observed. However, this was only one of many theories, albeit the most popular one, attempting to explain Buffington's result. In the following sections, I will briefly describe some of the other theories.

I would like to note here that an absence of low-energy antiprotons would not discredit this picture of supersymmetric dark matter residing in the halo. With the

right choice of particle masses for the dark matter, squark and slepton masses, and vacuum expectation values for the two higgs scalars, etc., a very low flux of low-energy antiprotons could also be expected.

4.2. Closed Galaxy Model

Other theories suggest that antiprotons are still secondary in nature with no need to suggest a primary source of antimatter. It is the 'leaky box' model of cosmic ray trapping that needs to be addressed. This would, for example, explain the absence of anti-alphas.

In the conventional 'leaky box' model, all cosmic ray particles traverse about 5 grams/cm^2; there may be an $E^{-\delta}$ energy dependence on this path length (Ormes and Protheroe, 1983), but in general all nuclei are treated equally.

In the closed galaxy model of Peters and Westergaard (1977), there are two major components in the cosmic-ray population - an old component inhabiting the galactic halo region and a young component inhabiting the galaxy's spiral arms. The young component, making up some fraction $f < 1$ of the cosmic ray spectrum, has an escape length $\lambda_{e,y}$ that is still very similar to that of the conventional model. The fraction f is between 0.74 and 0.97. The old component has escaped to the halo and now has an escape length $\lambda_{e,o} >>> \lambda_{e,y}$. Thus, these nuclei have existed in the halo much longer, undergoing many more collisions and traveling through much more material than the young component. All of these nuclei have been broken down into protons (the neutrons having long since decayed to protons) and the number of antiprotons overall has been enhanced due to this greater amount of grammage traversed. Also, if this path length $\lambda_{e,o}$ is much greater than the nuclear reaction pathlength, a significant number of antiprotons will have shifted their

energies to the lower end of the spectrum, changing the shape of the antiproton spectrum. A judicious juggling of paramaters, especially looking carefully at the non-annihilation inelastic collision role in cosmic-ray propagation, it is possible to explain this enhanced production of low-energy antiprotons (Stephens, 1981; Protheroe, 1981; Kiraly et al., 1981). However, since conditions in the halo are not known very well and no experimental evidence of these two very different populations exist as yet, this model is far from being accepted. A review and comparison of several authors' calculations (Stephens, Protheroe, Tan and Ng) can be seen in Tan and Ng's 1983 paper.

4.3. Baryon-Antibaryon Symmetric Universe Model

Another possible source for low-energy antiprotons is a baryon-antibaryon symmetric universe (Stecker, 1981; Szabelski, Wdowczyk, Wolfendale, 1981; Gaisser and Levy, 1974; Stecker and Wolfendale, 1984). A nice review of this theory is included in a paper by Stecker (1988).

In this model, various regions or domains of the galaxy would have had a slight matter or antimatter excess in the early universe. In conventional models, the entire early universe had a matter excess. As the universe cooled, most of the matter particles annihilated with the antimatter also present. But, the universe had some matter "left over." This matter excess occurred because of baryon number violation, breaking of thermodynamic equilibrium, and violation of C and CP symmetry. The direction of the CP violation would determine whether matter or antimatter would be in excess. In the baryon-antibaryon domain theory, the CP violation arises from spontaneous symmetry breaking as the universe cooled below some temperature T_{cp} at time t_{cp} after the big bang. Thus, regions separated by

distances larger than ct_{cp} may have different directions of the CP violation leading to the matter and antimatter excess domains with an overall neutral sign of the CP violation. Such a domain model could be accomodated within present measurements of background gamma ray flux.

Thus, the cosmic-ray spectrum may hold a small component of extragalactic particles that arrive from these different domains. Because of the scattering effects of the tangled magnetic fields, this extragalactic component could consist equally of protons and antiprotons. Thus, while the greater part of the observed cosmic-ray protons will be galactic in nature, most of the antiprotons would be extragalctic in nature.

Most authors assume a cosmic-ray source spectral index of 2.0 ($\gamma = 2.0$) with an escape pathlength that scales as $E^{-\delta}$ with $\delta \cong 0.7$. The extragalactic component would then have a spectral index of 2.0 and be much flatter than the $\gamma = 2.7$ index of the galactic component. Thus, the expected ratio of extragalactic antiprotons to mostly galactic protons should increase with energy as E^{δ} (Stecker and Wolfendale, 1984). At low energies, the antiproton/proton ratio could be 10^{-2} to 10^{-5} (depending upon the author) which would increase at higher energies and become unity at about 10^5 GeV. These authors cite a flattening in the cosmic-ray spectrum at this point as some indication of the validity of this picture. However, the adiabatic deceleration of this extragalactic component as it enters the galactic wind is another complication which has not been detailed fully at this time. This galactic wind could prevent the lower-energy particles from entering the galaxy.

One other problem with this picture is the absence so far of anti-helium sightings. Although it is possible that the anti-alphas are broken down during emission from their anti-galaxies, a finite anti-alpha/alpha ratio of about 10^{-5} is

expected, but has not been seen yet.

4.4. Relativistic Plasma Model

Another model indicates a secondary nature to the observed antiprotons which would then explain the lack of anti-alpha observations. The antiprotons are the decay products of antineutrons produced in p - p collisions in astrophysical relativistic plasmas (Dermer and Ramaty, 1986). The reaction

$$p + p \rightarrow p + p + n + \bar{n} + [\ ]$$

would occur with both target and projectile in motion, kinematically allowing much lower energy antineutrons to be produced. Since these plasmas are most likely associated with accretion disks around neutron stars or black holes, the likely intense magnetic field would not allow the direct escape of the secondary antiprotons produced. These sources may be associated with gamma-ray and x-ray point sources.

To be viable as antiproton sources, the produced antineutrons must not decay before escape (thus the collapsed star mass must be less than 10^7 solar masses), must not interact strongly before escaping (the amount of material traversed must be less than 50 g/cm^2), and must traverse the object's magnetic field without a drastic energy change (easily satisfied in most accretion disk models).

One calculation of the antiproton flux from both secondary production in the ISM and in thick relativistic plasmas is shown in Fig. 10. Here all the particles have momenta greater than the cutoff momentum P_{co} = 500 MeV/c. (If P_{co} approaches zero, the p - p collisions where the target particle is nearly at rest

predominates and the picture reduces to the ISM case.) This model is normalized to the experimental data since the number of such sources is not known. For the experimental antiproton spectrum above 2 GeV, this model is satifactory, but predicts a flux greater than that measured by the Buffington group at lower energies.

4.5. Other Models

Of course, one can go on and on with various models proposed during the long period when only the Buffington group's lone experimental point was available to theorists. Some of these were variations of previously mentioned models - such as point gamma-ray sources surrounded by thick matter clouds (Cowsik and Wilson, 1975; Cowsik and Gaisser, 1981) or adiabatic deceleration of secondary antiprotons in an expanding source (Eichler, 1982) or expanding propagation region (Streitmatter et al., 1982). One such source that has been suggested is an exploding galactic center producing proton - antiproton pairs, or even a whole series of intermittent galactic center explosions (Khazan and Ptuskin, 1977). Several authors (Hawking, 1974; Page and Hawking, 1976; Carr, 1976; Carter, et al., 1976; Kiraly, et al., 1981) have suggested that evaporating primordial black holes, radiating as black bodies, may radiate 12% of their energy in nucleon - antinucleon pairs and thus may be a source of primary antiprotons.

Each of these models have their separate strengths and weaknesses with differing predictions of the antiproton spectrum. However, with the scarcity of hard data on the fine details of the antiproton spectrum or even corroboration of the very surprising antiproton result at the low-energy end of the spectrum below the kinematic limit for the usual secondary production theory, all of these models

could be made to fit the available data. The need for an experiment such as LEAP was apparent and, in 1987, LEAP added its data to this field with the hope of narrowing the range of theoretical possibilities for the antiproton flux in the galaxy.

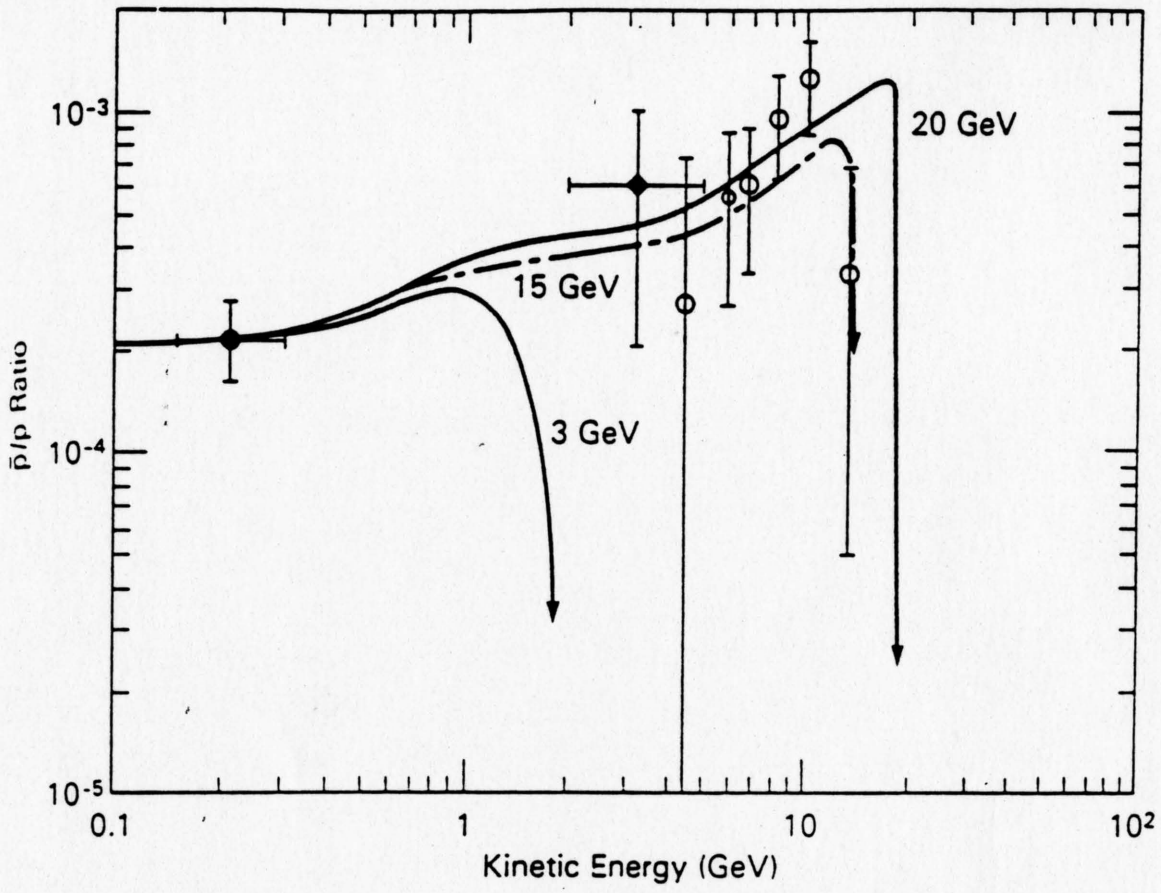

Fig. 9. Primary cosmic-ray antiproton/proton ratio as a function of kinetic energy from dark matter annihilation for various values of the supersymmetric particle mass. From Rudaz and Stecker (1988).

Experimental data from Buffington et al. (1981), filled circle; Bogomolov et al. (1979), filled diamond; Golden et al. (1984), open circle.

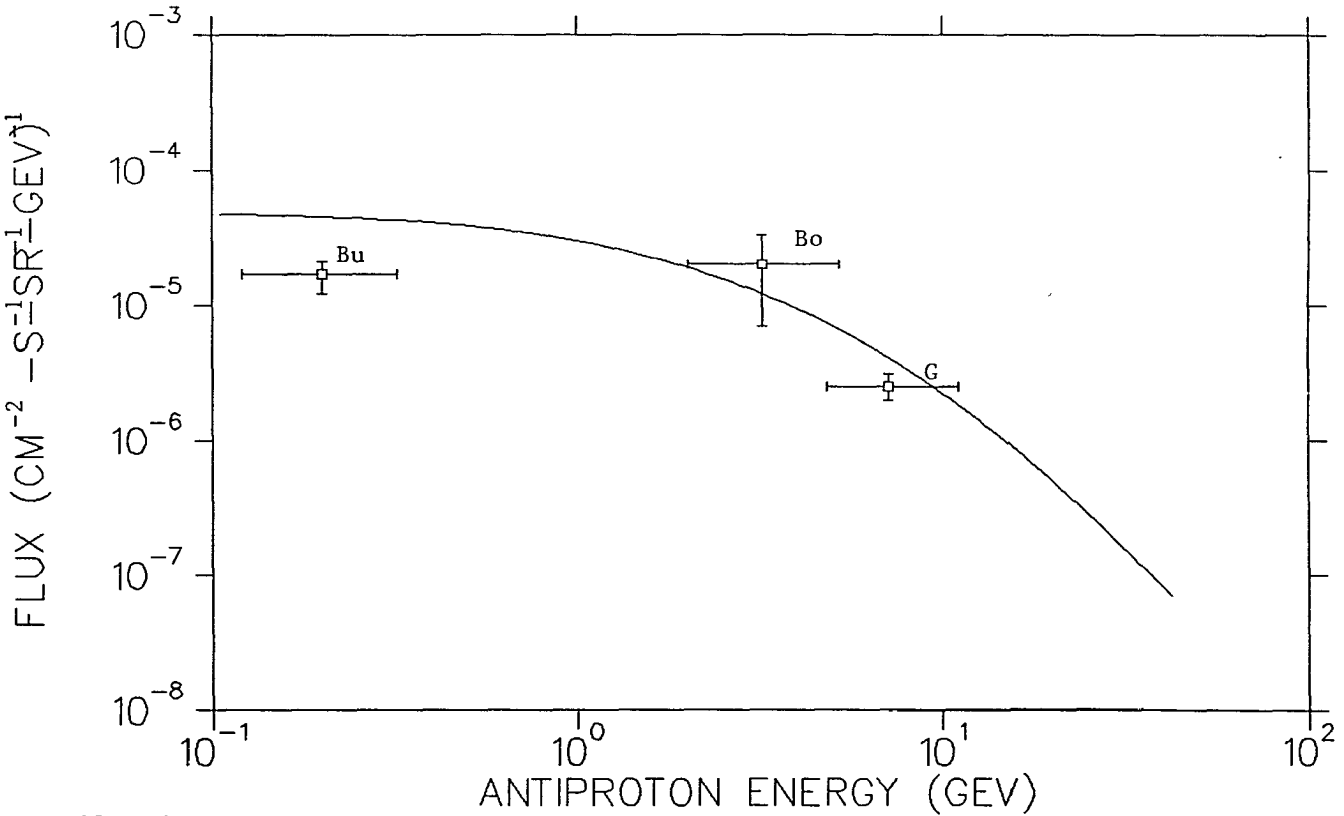

Fig. 10. The antiproton flux from the decay of antineutrons produced in a non-thermal relativistic plasma with P_{co} = 500 MeV/c (cut-off momentum). This flux is fit to the antiproton data in excess of the leaky-box contribution. The data Bu, Bo, and G are from Buffington, Bogomolov, and Golden, respectively. From Dermer and Ramaty (1986).

CHAPTER 5

LEAP EXPERIMENTAL DESIGN

On August 21, 1987, the LEAP (low-energy antiproton) experiment was launched from Prince Albert, Canada. LEAP, a high-altitude balloon antiproton search is a collaboration of groups at NASA/Goddard Space Flight Center, New Mexico State University, and the University of Arizona. The principal components of LEAP are the NMSU magnet spectrometer, GSFC time-of-flight counters, and a UA Cherenkov counter. A schematic of the experimental stack is shown in Fig. 11. The magnet spectrometer measures the charge sign and rigidity of particles by tracing their trajectories using eight planes of x - y multiwire proportional counters (MWPC's) in a magnetic field produced by a superconducting magnet coil. The time - of - flight (TOF) system consists of four planes (two above the magnet, two below the magnet) of plastic scintillator slabs which were viewed by photomultiplier tubes at one end of each slab. The TOF system measured the velocity of the incoming particles and was sufficiently accurate for particle-separation purposes below 500 MeV.

The Cherenkov counter, described in more detail later, was designed and built by T. Bowen and me and extended the energy range of LEAP to 1.2 GeV. Protons and antiprotons with less than 1.2 GeV kinetic energy radiated less than 1/2 of the maximum Cherenkov light intensity; in the same rigidity range lighter particles, such as pions, muons, and kaons, radiate nearly the maximum intensity. Thus, the Cherenkov counter could effectively separate the heavier protons from the relatively light background particles.

Directly below the Cherenkov counter was a plastic scintillator counter (S2) which recorded the exit of particles from the bottom of the Cherenkov counter.

At the top of the LEAP stack, a scintillator detector (S1) was used to determine the particles' charge and, in combination with S2, was an additional rough check on the time - of - flight and travel direction.

Thus, the LEAP experiment was designed to detect antiprotons in the 120 MeV to 1.2 GeV kinetic energy range. In the next few sections, I will discuss each component of LEAP in greater detail, with special attention to the Cherenkov counter and the scintillator S2 which were largely our responsibility at the University of Arizona.

5.1. NMSU Magnet Spectrometer

The magnet spectrometer, described in detail elsewhere (Golden, 1985), consists of a superconducting magnet coil and eight planes of multiwire proportional counters. The magnet was essentially a large coil of copper-clad niobium-titanium wire (outer diameter of 60.96 centimeters with a rectangular cross section measuring 7.62 cm x 12.9 cm) in a dewar of liquid helium. For NI = 1.3×10^6 amp - turns, a magnetic field of over 34 kilogauss was generated at the center of the coil arrangement.

The particles' trajectories through this magnetic field was traced with the MWPC's. Thus, at eight values of z (in our coordinate system), x and y were measured with a 50 micron resolution. Then, using a complex least-squares routine, the particle's curvature and thus rigidity

$$R = Pc/Ze \tag{5.1}$$

was calculated. The geometric factor of this spectrometer telescope was energy dependent - approximately 200 cm^2-sr.

5.2. Time - of - Flight System

The time - of - flight detector was designed at Goddard Space Flight Center and is also described in detail elsewhere (Streitmatter et al., 1989). The TOF was essentially twenty scintillating counters arranged in four planes. Each counter was a one centimeter thick plastic (Bicron 404) scintillating paddle, viewed at one end by a Hamamatsu R2490-01 photomultiplying tube (PMT). Two planes (T1 and T2) are above the MWPC's; two planes (T3 and T4) are below. The centerlines of the top and bottom planes are six nanoseconds apart at light speed, and time - of - flight is determined to within 200 - 270 picoseconds, depending on the paddles used. This resolution was achieved by doing an extensive time-walk analysis of the PMT pulses received and recorded during the flight. A resolution of 200 picoseconds was obtained in the 120 MeV to 360 MeV kinetic energy range, translating to an uncertainty of +/- 0.05 for beta. The lower kinetic energy limit was set by the ionization energy loss of each particle due to the thickness of atmosphere above the LEAP gondola and the thickness of the experimental stack itself.

Above 500 MeV (beta of 0.75), the time - of - flight measurement was not sufficiently accurate to separate protons from pions and muons, but could be used to determine the basic travel direction (up or down) of the particles passing through the experimental stack. This proved invaluable in screening out the albedo protons which could be mistaken for antiprotons otherwise.

5.3. Cherenkov Counter

In essence, the Cherenkov counter consists of a 44.45 cm x 44.45 cm x 12.7 cm box filled with FC72, a liquid fluorocarbon which emits Cherenkov radiation whenever charged particles pass through with a velocity exceeding the speed of light in this medium.

There are several excellent treatments of Cherenkov radiation theory, such as by Jackson (1975) and Jelley (1958). Basically, Cherenkov radiation occurs whenever a charged particle travels through a medium at a velocity greater than the velocity of light in that medium. The radiation occurs along a cone with the particle as the vertex; the situation is mathematically analogous to the sonic boom that occurs along the shock front of any object traveling at a speed greater than the speed of sound in that medium, although the Cherenkov case differs in that the radiation is dipole radiation emanating from distorted atoms in the Cherenkov medium. Since the refractive index n(ref) is the ratio between the speed of light in vacuum and the speed of light in the medium, each material has a threshold velocity below which no Cherenkov radiation occurs. At threshold,

$$\beta_{min} = \frac{1}{n(ref)} \quad . \tag{5.2}$$

The photons are mainly in the visible and ultraviolet. At higher frequencies, such as in the x-ray range, n(ref) is less than one and the threshold can never be reached. In many Cherenkov detectors, the characteristic angle

$$\cos\theta = \frac{1}{\beta n(ref)} \tag{5.3}$$

that the radiation travels is the measured quantity. However, our counter was designed to utilize the total integrated light intensity. As discussed later, light collection efficiency was very important and maximum efficiency could be achieved by sacrificing any information on the Cherenkov radiation angle.

Both the intensity of the light and the number of photons emitted is proportional to

$$I \propto 1 - \frac{1}{\beta^2 n^2(\text{ref})} \tag{5.4}$$

where the index of refraction is assumed to be a constant. Since the maximum beta is 1.0, the intensity ratio

$$I/(I_{max}) = \left[1 - \frac{1}{\beta^2 n^2(\text{ref})}\right] / \left[1 - \frac{1}{n^2(\text{ref})}\right] \tag{5.5}$$

is a function only of β and n(ref). In Fig. 12, I have plotted the ratio I/I_{max} as a function of the particle kinetic energy for several values of n(ref). To separate the antiprotons from the pions, we need the antiprotons in the energy range we are interested in to radiate less than 50% of the maximum and the pions to radiate more than 50% of the maximum. At 50% of the maximum intensity, the antiproton (and proton) curves have the greatest slope and is the most useful range for gathering information on beta. As can be seen from Fig. 12, an index of refraction in the range of 1.10 to 1.27 is necessary for the separation of antiprotons from muons, etc., in an energy range which overlaps the sensitive energy range of the TOF system and allows us to extend the LEAP energy range significantly above that of the TOF system.

Another consideration was the coefficient of absorption of these materials. The energy radiated as Cherenkov light per unit distance along the particle's trajectory (Jelley, 1958) is

$$\left[\frac{dE}{d\ell}\right]_{rad} = \frac{(Ze)^2}{c^2} \int_{n^2 > \frac{1}{\beta^2}} \omega \left[1 - \frac{1}{\beta^2 n^2(ref)}\right] d\omega \quad . \tag{5.6}$$

If we assume a singly-charged particle in a medium of constant n(ref), the number of Cherenkov photons emitted per unit length between wavelengths λ_1 and λ_2 is

$$N = 2\pi\, \alpha\ell \left[\frac{1}{\lambda_2} - \frac{1}{\lambda_1}\right] \left[1 - \frac{1}{\beta^2 n^2(ref)}\right] \tag{5.7}$$

where $\alpha = e^2/\hbar c = 1/137$. In the visible region, for $\ell = 12.7$ cm, $\beta = 1.0$, and n(ref) = 1.25, approximately 1430 photons are emitted in the 400 nm to 550 nm wavelength range. For PMT's having a quantum efficiency of 10%, that corresponds to 143 photoelectrons on average. This is assuming that all of the photons are channeled into the PMT's with 100% efficiency, which is of course never realized. Thus, yield and efficiency are at a premium and we need a very low coefficient of absorption in the visible and, hopefully, the ultraviolet so that a wide bandwidth can be used.

The majority of solid and liquid Cherenkov detector media possess an index of refraction greater than 1.33 (n(ref)=1.33 for water-see Fig. 45). All the most likely candidates were liquids and included liquid N_2, water, and the fluid fluorocarbons from 3M tradenamed FC72, FC75, FC84, and FC104.

Since these 3M products had very rarely been used for this purpose, the needed information on the refractive index n(λ) and the coefficient of absorption was limited. For a related fluorocarbon FC88, the light attenuation in 1 centimeter as a function of wavelength was available and showed a band of high absorption in the near ultraviolet which was disturbing. From 3M, an "average" index of refraction (no wavelength specified) for the candidate liquids at 25° C was quoted (3M, 1985); these are shown in Table 1. With an index of 1.276, FC75 was deemed marginal. 3M did have additional information on FC75 - the variation of n(ref) at 546.1 nm as a function of temperature and the refractive index at 20° C as a function of wavelength, which made FC75 unacceptable since n(ref) increased beyond 1.276 at 20° C. However, this type of information on the more promising FC fluids was not available. Thus, I made the necessary measurements of n(λ) over the visible and of the absorption coefficient in the visible and ultraviolet for FC72, FC75, FC84, and FC104.

The results of these optical measurements are presented in Appendix A. We decided that of the candidates, FC72 was the most appropriate medium because of its 1.25 index of refraction, its low coefficient of absorption in the visible and ultraviolet, and the slow variation in n(λ) as a function of wavelength and temperature. In addition, of all the 3M FC fluids, FC72 was the least expensive and, at a density of 1.68 gm/cm^3, the lightest. Also, with FC72 a fluid at room temperature, it was much easier to handle than any cryogenic liquids that were considered.

In the final design, the liquid FC72 was held in a 45 cm x 45 cm x 12.7 cm plexiglas box. This box was viewed by 16 Hamamatsu R2490-01 PMT's held in place by an aluminum box that surrounded the plexiglas box (see Fig. 13).

The plexiglas box was constructed of 1/4" thick UVA (ultraviolet absorbing) plexiglas. As shown in Fig. 13, the box had two projections, a filling nipple and a venting nipple, allowing the filling and venting of FC72 into and out of the plexiglas box. The inside surface was coated with a waveshifter mixture (p-Terphenyl, Bis-MSB, and PPO) referred to as "blue waveshifter" by Viehmann and Frost (1979). The waveshifter allowed us to detect the ultraviolet part of the Cherenkov spectrum, increasing the number of detected photons. Since the coating was on the inner surface of the box, UVT (ultraviolet transmitting) plexiglas was not necessary. In fact, we specifically avoided UVT plexiglas since, in the past, UVT plexiglas has been found to emit scintillation light.

Immediately surrounding this clear box was an aluminum box, providing the light-tightness necessary for the low light production in the counter and providing a system for holding the PMT's in place. The bottom and sides, excluding the PMT holders (projections on the four sides), was cut from a single piece of 1/16" aluminum and folded into position. The seams and PMT holders were welded together. The top is a separate removable piece, complete with projections which allow clearance for the plexiglas fill and vent nipples and which allow the necessary tubing to be attached to the plexiglas nipples and fed through to the outside. The top piece was attached to the rest of the box with black optical tape. The inside surface of the aluminum box was painted with Eastman Kodak $BaSO_4$ paint. This highly reflective paint (Shai and Schutt, 1971; Grum and Luckey, 1968) allowed us to collect a large fraction of the Cherenkov light generated by each particle. Sixteen 2" diameter Hamamatsu tubes viewed this box, each PMT face bordered by a 1/4" non-reflective area (the layers of 1/4" thick foam used to stabilize the tubes in position). The resulting efficiency factor of the white box

was roughly 38%.

The Hamamatsu R2490-01 PMT's are able to operate without magnetic shielding in the 500 - 1000 gauss magnetic spectrometer fringe field present at the counter's position, provided that the PMT's axis is parallel to the magnetic field line direction to within 5°. If heavy iron shields had been necessary, they would have distorted the spectrometer field, requiring intensive mapping of the field, as well as adding significantly to the total weight of the experiment. To accomodate the Hamamatsu tube, each projection of the aluminum box had to be attached at a specific angle.

I developed a computer model of the LEAP magnetic field to determine the direction of the magnetic field lines. The numerical solution is discussed in Appendix B. To test the resulting tube angles, a coil of approximately the same dimensions as the superconducting magnet on LEAP generated a low magnitude test field. A mock-up of the aluminum box with its tube projections was constructed and placed in the same relative position to the magnet as on the flight. A Bell 640 incremental magnetometer measured the direction of the field at each tube holder and determined that each PMT axis was parallel to the magnetic field lines.

The filling system designed to fill the counter with FC72 while in place in the LEAP system is shown in Fig. 14. A careful design was necessary to satisfy the following requirements. The filling system must, first of all, be able to completely fill the counter, without bubbles, and drain the counter completely while in place in the LEAP gondola without the advantage of being able to visually check the liquid level. The system must be able to accomodate any pressure changes in the gondola (equalizing the pressure between the FC72 and the gondola atmosphere) and any volume changes in the FC72 liquid (due to temperature changes). The

filling system must preserve the liqht-tightness of the Cherenkov counter. Finally, the system must not spill or leak fluid, even when the gondola tips over on landing, to avoid contamination of the other LEAP detectors and loss of the FC72 (the counter contained about $1000 worth of FC72).

Clear tygon tubing, 1/4" inner diameter, was attached to both the inlet and vent nipples of the plexiglas box, was fed through the aluminum box, and was then attached to copper tubing formed into four helical turns. The tygon tubing between the aluminum box and the copper helices was covered with two layers of black shrink-wrap electronic spaghetti tubing. The shrink-wrap and the copper tubing spirals prevented light from entering the counter through the inlet and outlet tubing, completing the light-tightness of the system. Both the fill and vent lines were attached to an outside reservoir directly exposed to atmospheric pressure with a capacity of two liters. This reservoir allows the FC72 to thermally expand and contract during the flight without pressurizing and damaging the plexiglas box. To discourage evaporation of the fluid, the reservoir lid was fitted to a long 1/8" inner diameter tube that circled the inner wall of the gondola for two full turns. This provided a long diffusion length of approximately 10 m and would prevent leakage if the gondola did not land upright after the flight.

The lines and valves shown in Fig. 14 allowed us to fill the counter without air bubbles in the counter itself and in any of the filling system lines. Since the counter was tilted slightly so that the vent outlet was at the counter's highest point, air bubbles in the counter were forced out that line. At the end of a filling cycle, the FC72 fluid level was visible through the translucent walls of the fluid reservoir, insuring that the counter was completely filled.

5.4. Scintillators S1 and S2

The scintillator placed directly under the Cherenkov counter was designed to detect the exit of particles from the bottom of the Cherenkov counter. Thus, particles that ranged out in the FC72 medium could be identified and eliminated. The scintillator S2 was a .635 cm thick piece of plastic scintillator (44.45 cm x 44.45 cm). A layer of aluminum foil covers the plastic; a layer of black optical tape covers the aluminum foil. Looking upwards at the plastic through a thin layer of silastic and optical coupling gel was a Hamamatsu R2490-01 PMT, held in place by two aluminum sleeves and additional taping (Fig. 15). The tube was centered on the scintillator slab since this was coincidentally where the magnetic field lines were perpendicular to the plane of S2 and, thus, parallel to the tube axis.

S1 was basically a 52 x 50 x 1.27 cm thick scintillator viewed at two opposite ends by PMT's, connected to the plastic by light pipes. The whole assumbly was then wrapped in aluminum foil and black tape to insure light-tightness.

5.5. Electronics

The LEAP stack used both NIM and CAMAC electronics. A logic diagram for the LEAP experiment as a whole is shown in the reference (Golden, 1987).

In Fig. 16, I show the Cherenkov wiring block diagram. Two Spellman 3kV high voltage supplies provided high voltage to the sixteen PMT's in the Cherenkov counter and to the additional PMT in the scintillation detector S2. Tubes 1 - 8 were powered by one supply, tubes 9-17 with the other. Thus, the failure of one unit would not disable the counter completely. Each power supply fed 2700 volts to distribution boxes, constructed at the University of Arizona. Each distribution

box was essentially a group of voltage dividers constructed with 5 Mega-ohm potentiometers. A voltage measurement point for each tube was also included for use with an electrostatic voltmeter. The times-10 amplifiers were also constructed in-house with Avantek GPD-110 high frequency amplifiers. The pulse amplifier circuit is shown in Fig. 17.

The voltage applied to each PMT was balanced using a light source I constructed so that the pulse due to the light source of each tube was equal. The light source used the conversion electrons (662 KeV) (Particle Properties Data Booklet, 1986) from a point Cs^{137} source embedded in a .254 cm radius sphere of plastic scintillator to provide a fixed pulse of light. At this thickness, the conversion electrons would deposit essentially all of their ionization energy loss in the scintillator, but the smearing of the energy peak at 662 KeV due to Compton recoil electrons was minimized. The resulting peaked pulses from the Hamamatsus were measured with a LeCroy model 3001 multi-channel analyzer in the charge-integrating mode. Each PMT was set at a point which corresponded to a gain of approximately 10^6.

Pulses from the Cherenkov PMT's were amplified separately for each PMT using the Avantek GPD-110 high frequency amplifiers. Then, these signals entered the LeCroy 2249 ADC's. The signal from S2 was also analyzed by one of these ADC's and, in addition, a signal splitter allowed us to use a TDC to allow rough TOF from the S1 - S2 signals.

An event will trigger the LEAP stack whenever there is at least one "hit" in each of the four TOF planes. These triggers are generated by an LRS 4564 logic unit whose signals are fed to an LRS 356 programmable coincidence unit. The readout was also programmed such that a signal from S1 was necessary to begin the

process of event recording.

Once an event triggers the logic units, the master trigger signal is fed through fanouts to the rest of the gondola, including a "readout - in - progress" flip-flop in the NMSU payload I/O module, informing the computer of the event and preventing the digitization of any other incoming event while the current event is being read into the computer. The computer resets the flip-flop when the read-out cycle is complete.

Each event is recorded in two frames containing 50 12 - bit words each. The first frame is the header frame; the second is the trailer frame. Both frames contain words which identify the event by number. The science frame for each event then contains the pulse-height analysis from the ADC's, the readout of the TDC's, and the MWPC signals.

In addition, four "engineering frames" are sent at regular intervals which records the gondola temperature in various sections of the gondola, voltage levels, pressure levels, etc.

An on-board PDP11/23 and a Microvax II on the ground allowed for some real-time processing of the incoming events.

5.6. Gondola Design

During June of 1987, the Arizona Cherenkov detector was integrated into the entire LEAP payload in Las Cruces, New Mexico, as was the TOF system, S1, and S2. The Cherenkov counter, S2, the supporting hexcell layers (aluminum honeycomb material), and other supports were placed at the bottom of the stack. An illustration of the LEAP experimental stack positioned within the gondola is shown in Fig. 18.

The gondola was roughly cylindrical with a height of 4 meters and a diameter of 2 meters. The gondola was built in 3 sections, with bolted flange joints sealed by O-rings, and pressurized to an absolute pressure slightly greater than one atmosphere. The gondola was insulated and painted white in order to stabilize the internal temperature of the gondola to 25° C +/- 10° C. Including the ballast and batteries needed for power, the entire experiment weighed in at 5400 pounds. Note that the Cherenkov counter and S2 contributed only 140 pounds to that total.

5.7. The Flight of August, 1987

From July 10 until the launch date in August, payload integration and testing continued at the launch site in an aircraft hangar at Prince Albert, Saskatchewan, Canada. With the trigger operational and the on-line software installed, the β=1 muon peak was used to do the final adjustment on the PMT gains. Other miscellaneous tests, such as a test of operation under cold (4° C) conditions, were performed.

LEAP was launched from Prince Albert, Canada, (long. 254.0, lat. 53.0) on August 21, 1987. A high-altitude helium-filled balloon manufactured by the Raven company carried the gondola to the upper atmosphere. The data run was conducted at 119,000 feet (with a residual atmospheric thickness of 4.7 g/cm^2). At Prince Albert, the calculated vertical geomagnetic cutoff rigidity was 0.66 GV (Shea and Smart, 1983) which increased as the balloon drifted to the southwest, where it landed near Medicine Hat, Alberta (long. 149.4, lat. 50.5 - a calculated cutoff of 1.09 GV) after nearly 20 hours of flight.

However, evidence of this energy cutoff was not seen during most of the

flight. Towards the end of the flight as the balloon drifted southward, only slight evidence of a cutoff appeared. This leads us to believe the calculated values to be incorrect. This did not impact the Cherenkov counter data analysis to any great extent. 0.66 GV corresponds to about 200 MeV and 1.09 GV corresponds to roughly 500 MeV as lower kinetic energy cutoffs.

In the next chapter, I will discuss the analysis of this collected data. The flight data was also used to calibrate and locate in space the position of the detectors. Thus, a preliminary antiproton/proton upper limit was culled from this flight and, in Chapter 6, I will discuss this.

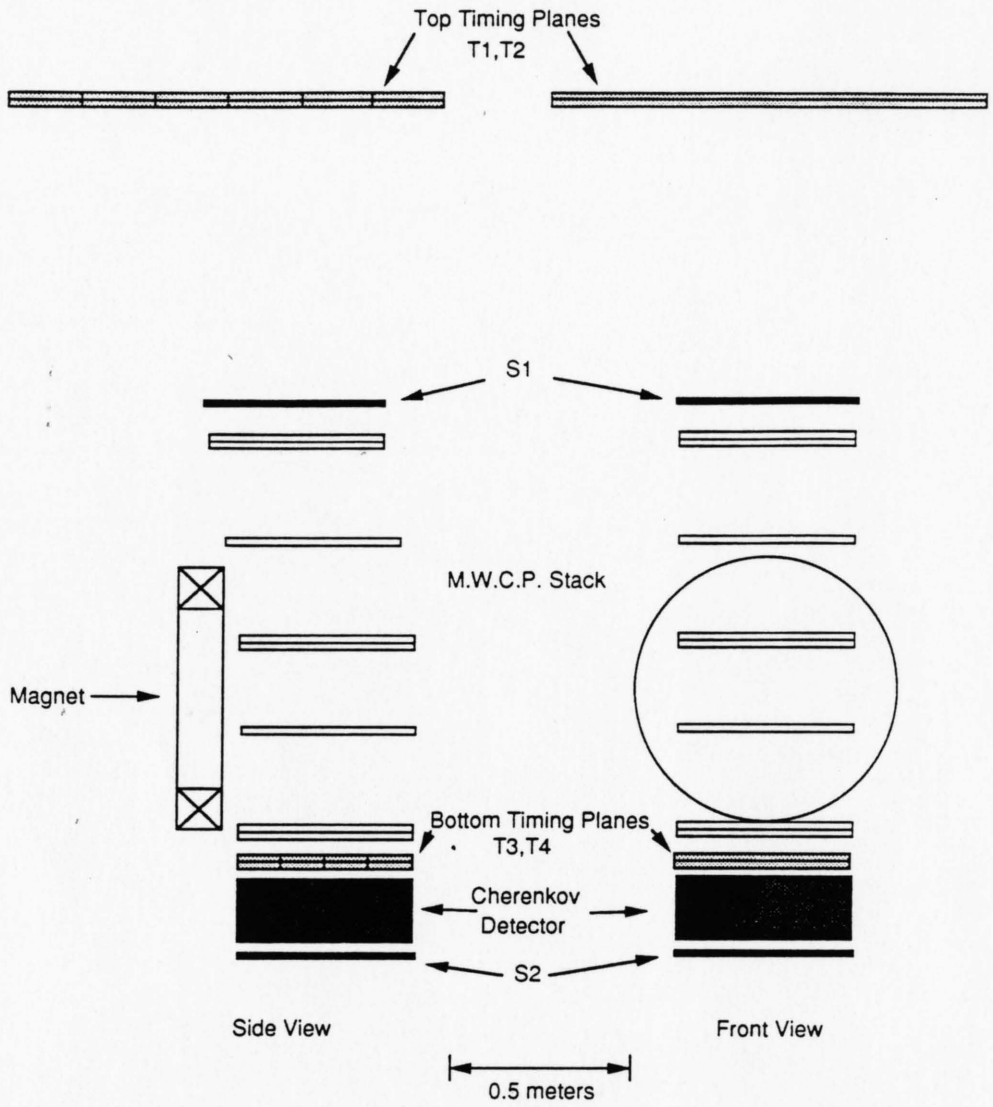

Fig. 11. The LEAP experiment, consisting of T1, T2, T3, T4 (the time-of-flight detector); S1, S2 (scintillation detectors); MWPC stack and magnet (the NMSU magnet spectrometer); and the Cherenkov detector.

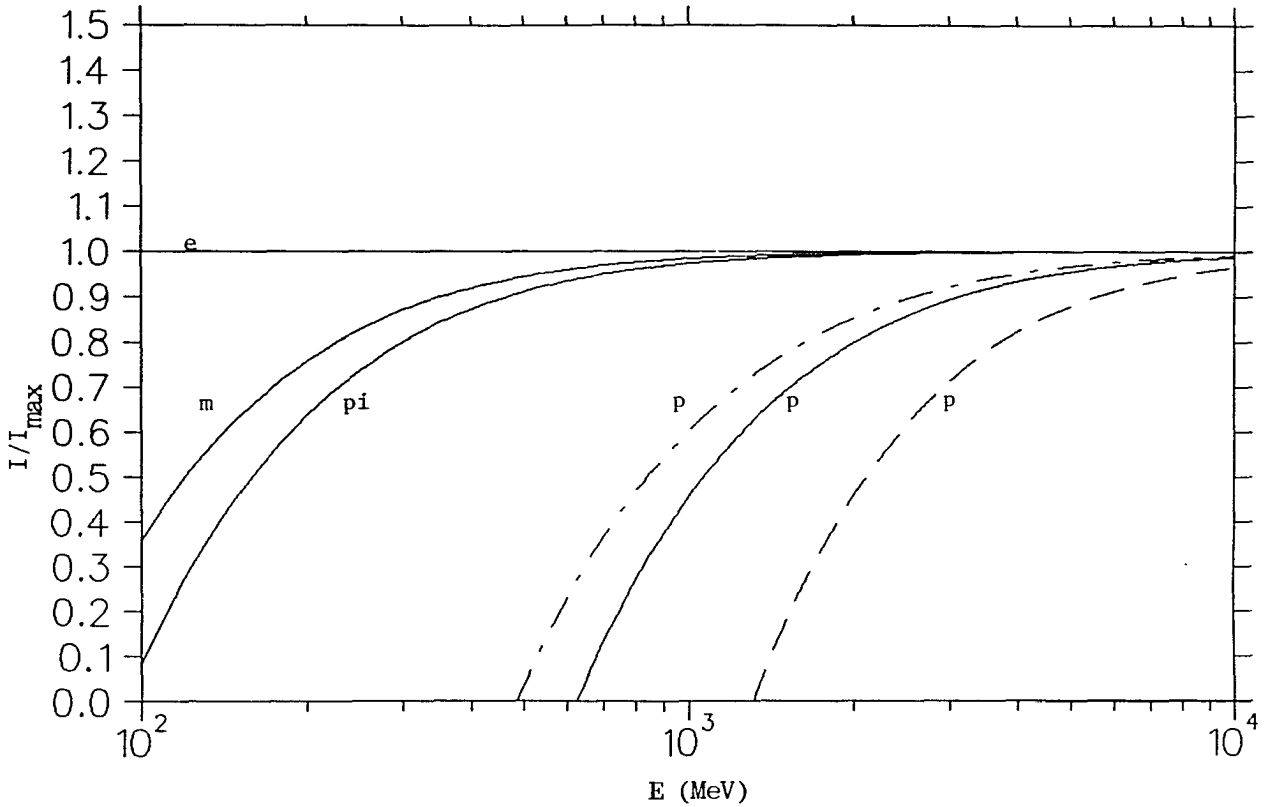

Fig. 12. The Cherenkov light I/I_{max}, where I_{max} is the maximum Cherenkov light for a Z=1 particle, as a function of kinetic energy E. The solid curves are for n(ref)=1.25. The dashed curve is for n(ref)=1.1. The dot-dashed curve is for n(ref)=1.33. Particles shown are: e, electrons; p, protons and antiprotons; m, muons; pi, pions.

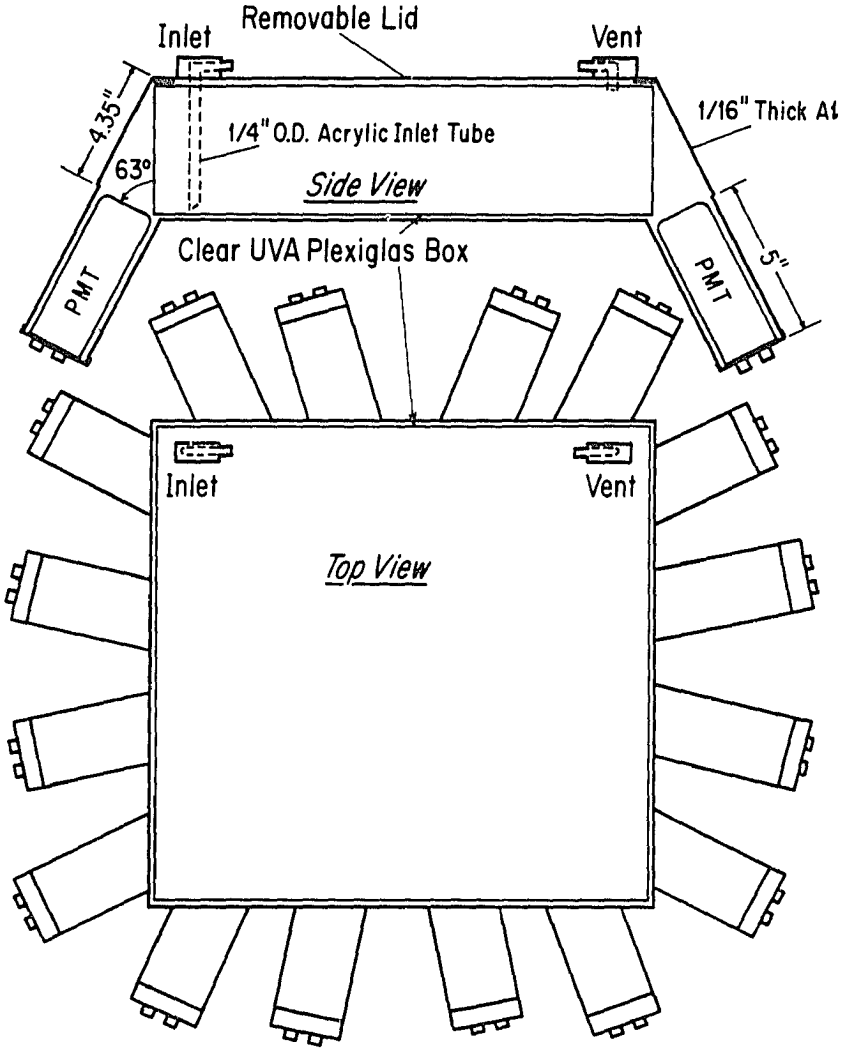

Fig. 13. Side and plan views of the Cherenkov detector, showing the aluminum box surrounding a clear UVA plexiglas box, which is coated on the inside with wavelength shifter dyes, and which contains the FC72. The 16 Hamamatsu R2490-01 PMT's view the FC72 along the four sides (four PMT's to a side).

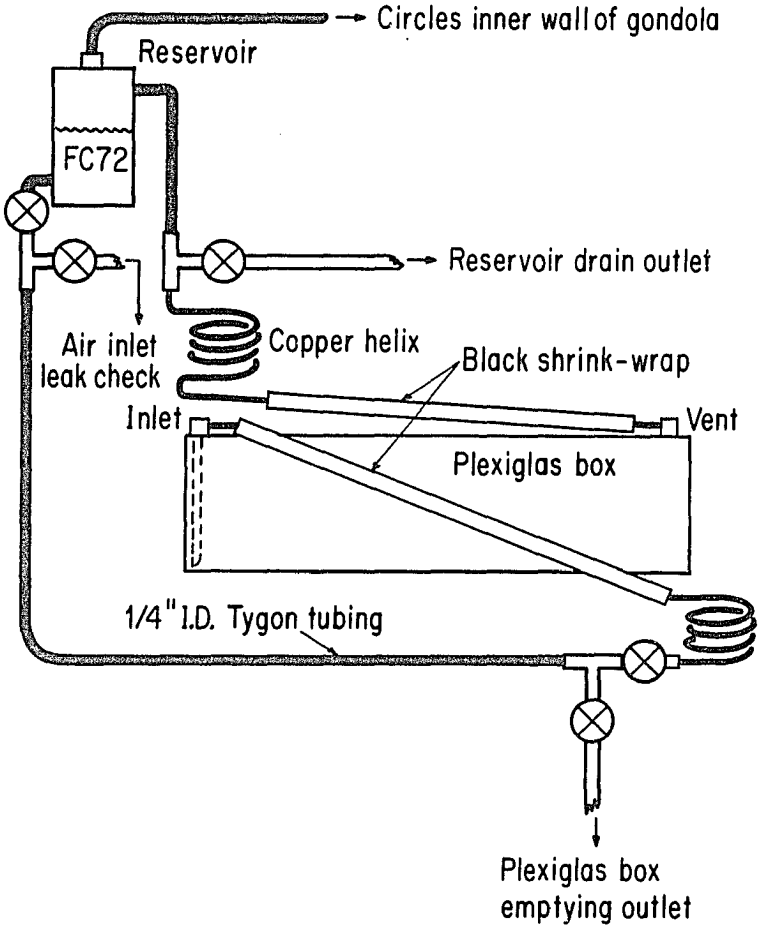

Fig. 14. The FC72 filling system, with 2 liter capacity reservoir. The plexiglas box shown rests within the aluminum box.

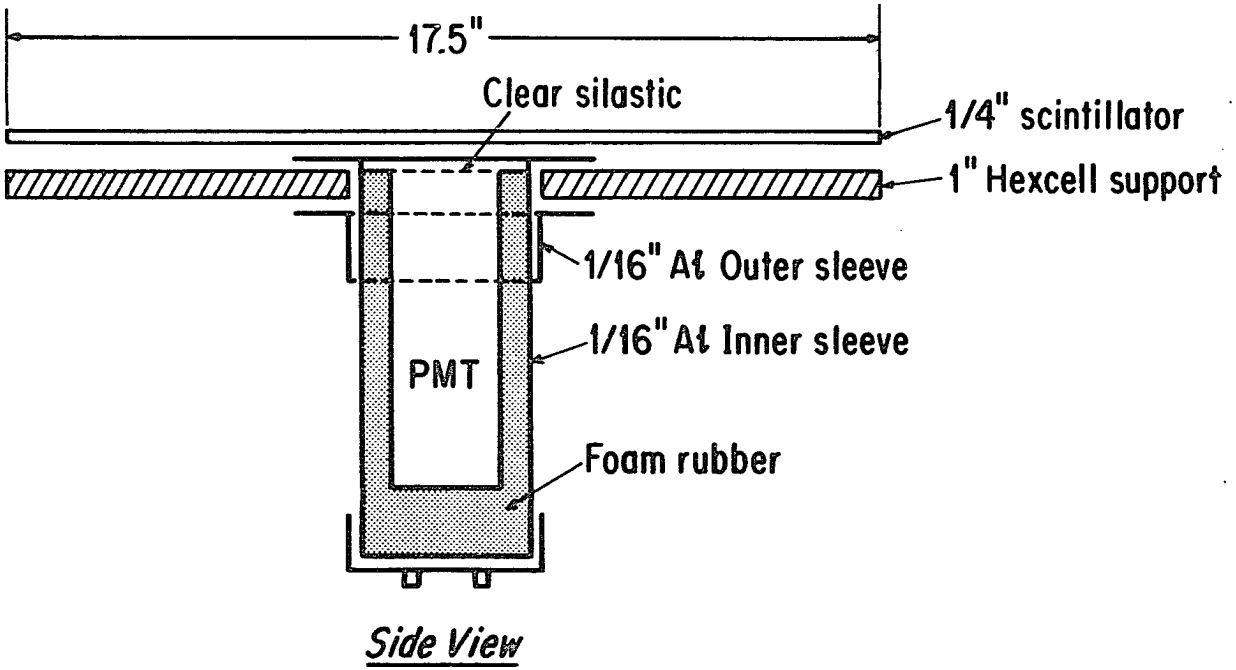

Fig. 15. Scintillation detector S2. Aluminum sleeves hold the PMT in place.

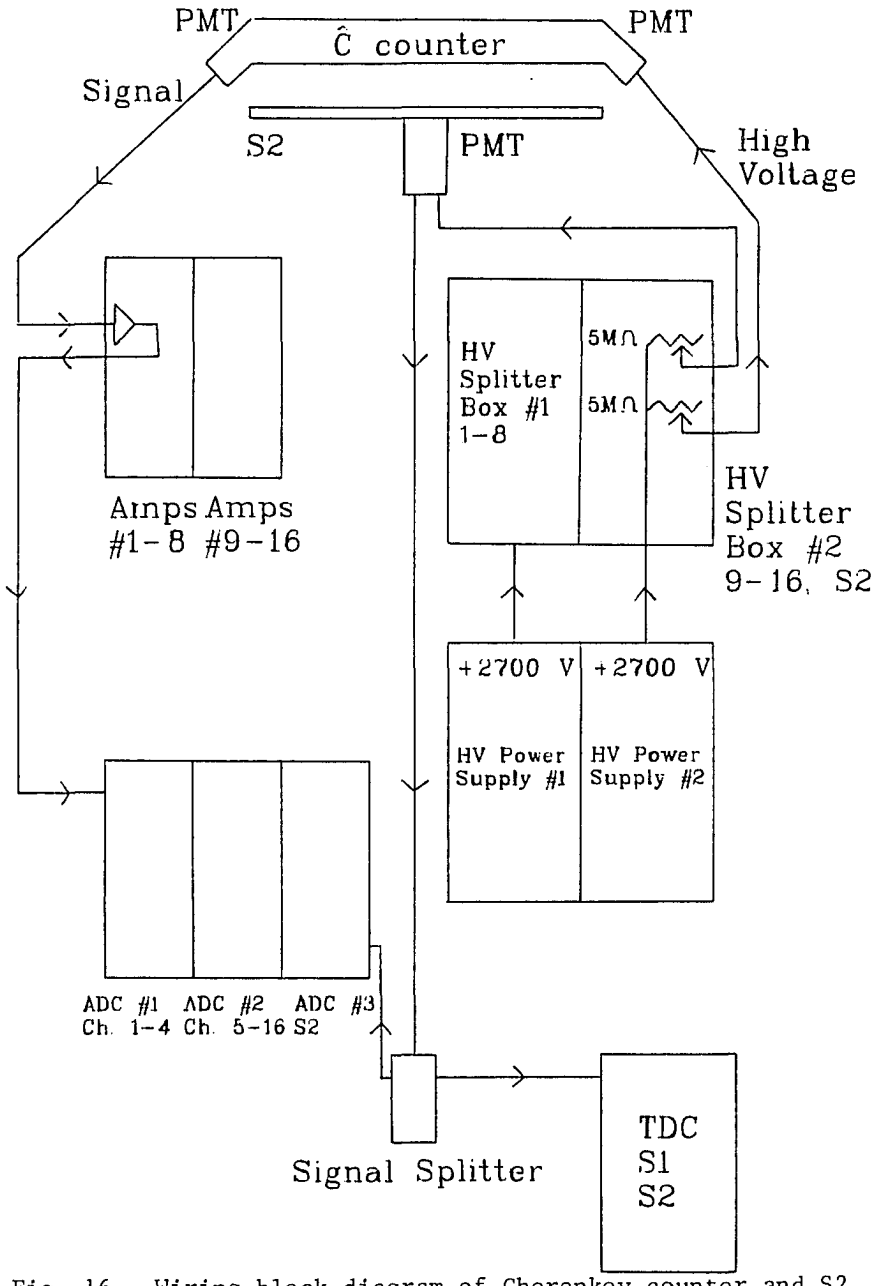

Fig. 16. Wiring block diagram of Cherenkov counter and S2 scintillation detector on LEAP.

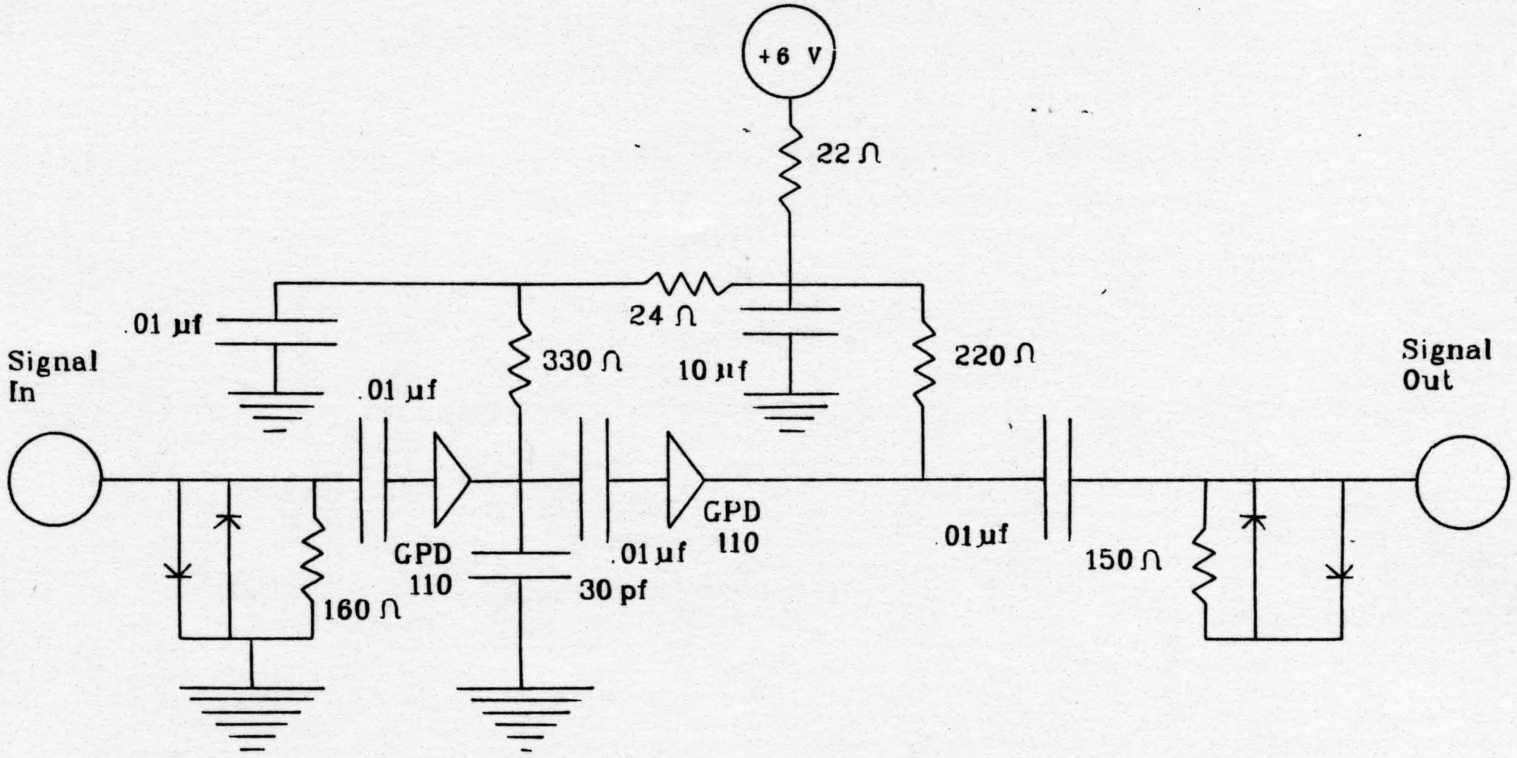

Fig. 17. Pulse amplifier circuit for x10 gain, utilyzing Avantek GPD-110 high frequency amplifiers. Each NIM module contained eight identical amplifiers.

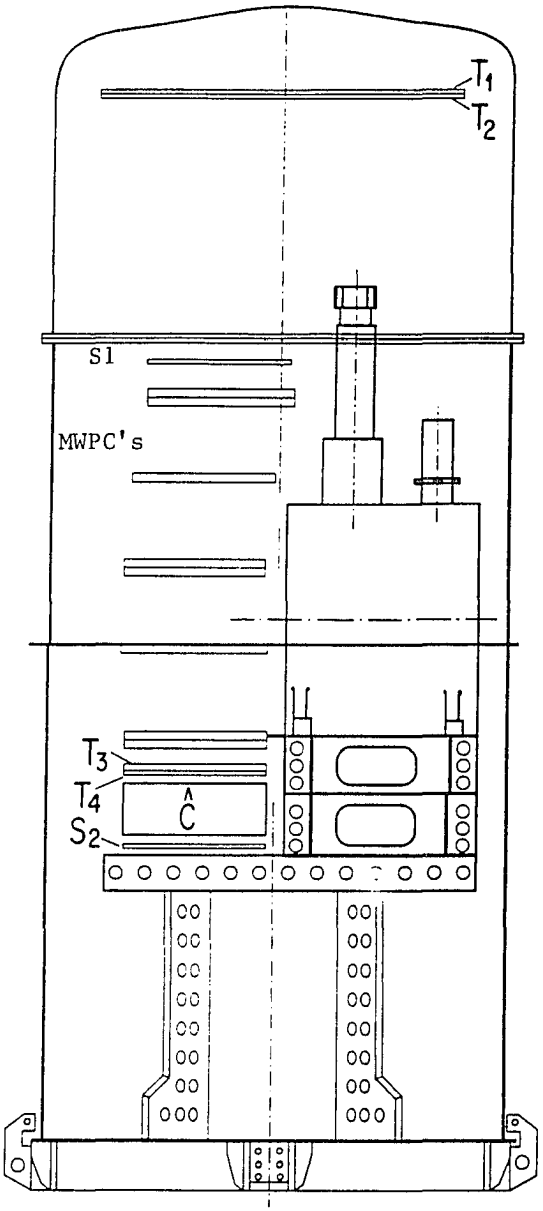

Fig. 18. The LEAP experimental stack situated within the gondola.

TABLE 1. The FC Cherenkov Medium Candidates

FC Fluid	n(ref) at 25° C	Typ. Boiling Point (° C)	Density (g/cm^3) at 25° C
FC72	1.251	56	1.68
FC75	1.276	102	1.76
FC84	1.261	80	1.73
FC104	1.271	101	1.76

From (3M, 1975)

CHAPTER 6

DATA ANALYSIS

The data analysis for the 500 MeV to 1.2 GeV kinetic energy range for which the Cherenkov counter data was essential was performed at the University of Arizona and thus I will concentrate on that segment of the analysis. A brief summary of the analysis performed by Goddard Space Flight Center using TOF system data is presented at the end of this chapter.

6.1. The Software System

As stated in the previous chapter, the flight data for each event was contained in a "science frame" of 100 12-bit words. These words make up the first 100 elements of the data array DAT(500). Each additional element was some analytic combination of previously computed or recorded elements of the array, subject to various flags computed from previous array elements which could veto or allow the calculation to proceed. A list of the DAT array is shown in Table 2.

The data for each event was read and the calculations performed by a software system, written in Fortran, that was developed by Dr. Robert Golden of New Mexico State University. To this overall system, the groups at Goddard Space Flight Center and at the University of Arizona could add additional subroutines that calculated other array elements of the DAT array for each event. Specifically, the first 91 words, DAT(1) - DAT(91), were the "raw" data recorded from the flight. DAT(95) - DAT(191) were the calculated MWPC values. DAT(300) - DAT(399) were computed by a Goddard Space Flight subroutine TDCCOM that determined

TOF values. Words (400) through (500) were calculated by our subroutine called CHERCOM and included the Cherenkov data. I will now discuss in more detail these array elements.

Each event had associated with it a unique identifying number contained in DAT(4) and DAT(5) - epas-hi and epas-lo.

DAT(6) - DAT(91) contained the flight data - the pulse height analysis (PHA) of the PMT's contained in the TOF system, the Cherenkov counter, S1, S2; the MWPC data; and the time-to-digital converter (TDC) output for the TOF system, S1, and S2.

DAT(95) - DAT(191) are the results of Dr. R. Golden's analysis of the MWPC data. This area includes measured values of x and y in his coordinate system and the fitted trajectory values of x and y. The particle trajectory was fitted using a least squares fitting routine of the raw MWPC data with greater than 100 elements. He also made available the fitted deflection (or inverse rigidity), the direction cosines, and the chi-squared values of the trajectory fit in the x and y directions. Finally, word 191 was a flag that indicated whether the trajectory fit was successful. At present, only the x values from planes 2, 4, 5, 6, and 7 and the y values in planes 2,5, and 6 are useable.

DAT(300) - DAT(343) are the various combinations of the TOF system data necessary to perform the TOF analysis, including the time-walk analysis that is contained in TDCCOM. Basically, the time-walk analysis removes the pulse-height amplitude dependence of the TDC "start" point at which timing is started or stopped for each PMT pulse arriving from the TOF paddles. DAT(344) - DAT(399) are the calculated values of the TOF beta, mass, and some intermediate values for the TOF system.

DAT(400) - DAT(500) was our responsibility and was calculated in the subroutine CHERCOM, written here at the University of Arizona.

Starting at the top, DAT(400) was simply the pathlength particles traveled in the Cherenkov counter - the thickness of the counter divided by the absolute value of the fitted direction cosine with the z axis.

DAT(401) - DAT(416) are the PHA of the 16 PMT's in the Cherenkov counter with the following corrections. The pedestal value (the "zero point" of the pulse height as seen by the LRS 2249 ADC's) was subtracted from each pulse-height to insure all PMT pulse heights reported the same numerical value for a null-pulse. The pedestal value for each PMT was monitored during the flight. Although the pedestals of the pulse-height data did vary with the experiment temperature during the flight, this variation (+/- 3% of the peak pulse-height) was much less than the variation due to the photon statistics (discussed later) and I treated the pedestals as constants during the flight. Also, gain factors for each PMT were calculated from data recorded just prior to the launch and used as a normalization factor, insuring that all 16 Cherenkov PMT's were reporting events on the same measurement scale. As we discussed in Chapter 5, a rough normalization had been done using a small light source prior to final integration into the LEAP experimental stack. With LEAP integrated and data recording from the entire stack taking place, we were able to do a more accurate calculation, weighting each tube so that the apparent average number of photoelectrons from the ground-level muon peak for each PMT was equal. Finally, using the path-length of each particle's trajectory through the Cherenkov counter (DAT(400)), I removed the cosine dependence of the Cherenkov output by dividing these pulse heights by the pathlength. Thus, DAT(401) - DAT(416) are the "corrected" PMT pulse heights.

DAT(417) is the "corrected" S2 pulse height. DAT(440) is the normalized S1 PHA.

DAT(418) is the sum of the 16 Cherenkov PMT "corrected" pulse heights, designated the gang output.

DAT(419) - DAT(424) are various combinations of Cherenkov PMT pulse heights. These combinations were used to monitor the Cherenkov system behavior during the flight.

DAT(425) - DAT(429), DAT(441), and DAT(442) are the x and y values in Golden's coordinate system of each particle's path through the Cherenkov counter, S1, and S2. For this purpose, I calculated the intersection point of the particle's trajectory as determined by the MWPC fitted trajectory and the plane of each counter in the midpoint of the counter thickness.

DAT(430) - DAT(499) are various quantities calculated to aid in the counter calibration and data cuts and will be discussed in the appropriate sections which follow.

For the data analysis, a record of all the negative rigidity events and 1 out of every 33 positive rigidity events was employed.

A subset of 50,000 events was used to calibrate the counter and to determine the best limits to employ on the data to isolate the protons and antiprotons. Each event in this subset had word(191) showing a successful trajectory fit.

6.2. Counter Calibration and Location

The 50,000 event subset of flight events was first used to map the position of the Cherenkov, S1, and S2 counter in three-dimensional space within the experimental setup. I simply plotted the events where the counter response was

well above the pedestal value and each event possessed a high rigidity (the absolute value of the rigidity greater than 2 GV). This insured a straight trajectory in the magnetic field in the vicinity of the counters. The x and y position where each event intersected the counter was plotted and an image of the Cherenkov, S1, and S2 counters was generated. All of the detectors had a "tail" of events that extended beyond the physical edge of each detector, producing a fuzziness in the image. The number of events in the tail decreased as the distance from the counter edge increased. The average Cherenkov output also decreased in this fashion. The tail extended for 3 to 4 centimeters beyond all the counters' boundaries.

I at first felt that our value of z (the distance the counters were above or below the origin of our coordinate system) was incorrect. Since we were using a straight-line trajectory, as computed from the MWPC data in MWPC planes either above or below the region of the greatest magnetic field, an overestimation in z would produce an image too large for the known dimensions of the detectors. For the z value, R. Golden had physically measured the experimental stack. I then tried different values of z in the trajectory calculation for the Cherenkov x and y coordinates, but the fuzziness scaled with the value of z. One possible explanation for this may be that the event tail is due to showers produced below the MWPC planes in which some knock-on electrons are produced. Thus, some particles could travel through the Cherenkov medium, producing light and PMT response, while the main body of the shower did not pass through the Cherenkov medium. However, this would only appear at the 1% level. A more likely explanation are relatively poor MWPC trajectory fits.

To determine the counters' boundaries, I determined the point on each boundary where the average number of perceived events began to diminish. I then

set these points as working boundaries. However, the apparent counter dimensions did not correspond precisely to the known dimensions of the counters, over or underestimating the dimensions by +/- 1 centimeter. If I then distribute this difference equally on all sides of the counter and add or subtract these small differences to the working boundaries, my final boundaries then correspond to the correct counter size. I thus had the boundary locations and the corresponding centers of the counters located in the LEAP coordinate system.

I then turned to the problem of counter calibration. A problem with all three counters was that the amplitude of each event was a strong function of the location of the event's passage through the counter.

To determine the nature of the dependence, I looked at the pulse heights of events as a function of r or x and y. The variable r is the distance from the center of the counter to the particle's intersection with the midplane of the counter. I used only events of high rigidity (as seen by the MWPC's) that passed within the counters' boundaries determined previously. For the purposes of calibration, I used the positive rigidity events where

$$0.1 < \frac{1}{R} < 0.5 \ (GV)^{-1}$$

and the negative rigidity events where

$$-2.0 < \frac{1}{R} < -0.1 \ (GV)^{-1} \quad .$$

The very high rigidity events would radiate the maximum Cherenkov intensity in the Cherenkov counter, and be minimum-ionizing particles in S1 and S2. Thus, the

pulse-height output of these high-rigidity particles should define a peak in the PMT outputs. Restricting the calibration events to particles passing within the counter boundaries weeded out the edge events where a particle may not have passed through the entire counter thickness; this served to sharpen the lower end of each peak.

At small values of r, too few events were recorded to be able to discern a well-defined peak due to the smaller detection area. However, it was found that for the well-defined peaks at larger values of r, a fixed percentile of events had pulse-heights below the peak average. So for each counter, I determined the percentage of events with pulse heights lower than the peak. I then used this fixed quantile to estimate the peak position in radii bins where too few events appeared to define any peak.

Using the 50,000 event subset, it was found that this peak position was a function of the distance r from the center of the detector to the particle's intersection with the midplane of the detector in both the Cherenkov counter and S2. In S1 there was a strong x, y dependence, z being normal to the plane of the detector.

I then fitted a function to the pulse-height versus r, or x and y, as seen by this subset of events. This function could be used as a normalization factor, removing this location dependence and allowing us to ignore the particle's intersection trajectory in later analysis.

For the Cherenkov counter, this functional dependence was

$$1.675 - 0.000278\ r^2 \quad ,$$

where r is the distance from the center of the Cherenkov counter. The radial dependence of the peak positions before correction is shown in Fig. 19. The fixed quantile for each peak position was 35%. In the Cherenkov counter case, I used the summation of the outputs of all 16 PMT's - the gang output.

The "corrected" pulse height where the output of each event is not a function of position is

$$I_{c,corrected} = \frac{I_{c,uncorrected}}{(1.675 - 0.000278\ r^2)} \quad . \tag{6.1}$$

The average of the corrected peaks was 1028 channels with a 3.4% standard deviation. The corrected pulse-height peak as a function of r is shown in Fig. 20.

For the scintillating counter S2, a pedestal value of 8 channels was subtracted. Particles passing through the center of S2 (and thus down through the PMT face directly) had anomolously high PMT pulse heights, indicating saturation. Thus, prior to any correction, this saturation peak was removed and placed at a very high channel value. Thus, we still used these events but did not bother to correct the outputs since they were already at saturation. For the rest of the events, the peak was found to correspond to the 32% quantile level.

For S2, the correction function is

$$I_{S2,corrected} = \frac{I_{S2,uncorrected}}{[(10.616)\arcsin(2.875/r) + \Sigma I_i]} \tag{6.2}$$

where the summation is the correction due to the reflected images of the source event. Each reflected image was added with a reflection coefficient factor f = 0.10. The arcsine of (k/r) is simply proportional to the line-image of the event's passage

as seen by the PMT. The counter response before calibration is shown in Fig. 21. The normalized peak positions of S2 as a function of r had an average of 81.8 (channels) and a standard deviation of 6%. The variation of $I_{S2,corrected}$ with r is shown in Fig. 22.

The analysis for S1 was performed by Dr. T. Bowen. He found the correction factor to be

$$S1CORR = (0.987 - 0.000392\ (y-13.8)^2)\ (0.782\ e^{-0.0281(x+2)}$$

$$+\ 0.846\ e^{-0.0281(50-x)} + 0.670\ e^{0.308(50-x)} \qquad (6.3)$$

Then

$$I_{S1,corrected} = \frac{I_{S1,uncorrected}}{S1CORR} \quad , \qquad (6.4)$$

where x and y are the coordinates within the counter. With this correction factor, the peak averaged 109 channels with a 2.9% standard deviation. The peaks were located at the 38% quantile. The peak positions before correction are shown in Figs. 23 and 24. In Fig. 23, there appears to be a large assymetry in the peak position averages. This indicates that the adhesive bond between the plastic scintillator of S1 and the light pipe of one of S1's PMT's was damaged. The corrected peak positions are shown in Figs. 25 and 26.

The differing counter correction functions are due to the differing PMT arrangements and reflection characteristics of each counter.

6.3. Cherenkov Counter Photon Statistics

To determine the average number of photoelectrons expected from a fast particle radiating the maximum Cherenkov light, I looked at the uncorrected PHA from the sixteen Cherenkov PMT's (DAT(476)-DAT(491)) with only a pedestal subtraction. There are no corrections for pathlength or gain.

I then looked at the population of negative rigidity events which passed the following cuts:

rigidity fit status good

chi-squared x and y cuts

Absolute value of S2 PHA greater than 40

S1 PHA between channels 64 and 200

TOF beta greater than zero

$$-2 \quad < \quad \frac{1}{R} \quad < \quad 0 \ (GV)^{-1}$$

and I looked at only events passing through a small central region possessing 1/9 of the area of the whole Cherenkov counter. These cuts are discussed in section 6.4.

It was possible to fit a Pearson's function of the form

$$f(x)\,dx = Ax^{n-1}\,e^{-\alpha x}\,dx \tag{6.5}$$

where

$$\alpha = \mu/\sigma^2 \ , \ n = \alpha\mu \ (1 < n < 2) \ ,$$

and

$$A = \frac{\alpha^n}{\Gamma(n)} \ .$$

Here, μ and σ are the mean and standard deviation of the PMT pulse height distribution. An example of a PMT output (the histogram) overlayed with the Pearson's function is shown in Fig. 27.

I then recorded the total number of events (n_{total} = 518) and the number of events in each tube that were at the pedestal (n_{zeros}) (thus, giving a zero photoelectron reading). In Poisson statistics, the probability of such a zero reading is

$$P(0) = e^{-\mu} \quad . \tag{6.6}$$

Thus,

$$\mu = \bar{n}_{p.e.} = \ell n \left[\frac{n_{total}}{n_{zeros}} \right] \quad . \tag{6.7}$$

Employing equation (6.7), I was able to calculate the average number of photoelectrons for each of the sixteen PMT's; when these 16 numbers were added together,

$$\langle n_{p.e.}\ (total) \rangle = \sum_{i=1}^{16} \ell n \left[\frac{n_{tot,i}}{n_{zeros,i}} \right] \quad , \tag{6.8}$$

they totaled 52.4 photoelectrons for a beta=1 particle.

However, there were a few events (14) that seemed to have an anomolously low total Cherenkov output. They did not seem to be a part of the general peak. When I excluded those few events, the average total number of photoelectrons calculated from equation (6.8) jumped to 72.2.

When looking at these negative rigidity events, the Cherenkov peak (Fig. 28)

has a tail at the high intensity end. This is not evident in the analogous population of positive rigidity events (Fig. 29) where

$$0 < \frac{1}{R} < 2 \text{ (GV)}^{-1} \quad .$$

Also, it is evident from looking at these two populations, that the peak channel is somewhat lower in the positive rigidity events than for the negative rigidity events.

It is evident that for the negative rigidity events (negative pions, muons, and electrons, with a very few antiprotons) that the high tail is composed of showering electrons. The radiation length in FC72 is approximately 36.1 g/cm^2: the exact molecular formula of the FC fluids is a trade secret. The Cherenkov counter thickness is 21.34 g/cm^2. Thus, more than half of the entering electrons will shower. The positive rigidity population has no such showering activity and is composed mostly of slower protons which explains the lower peak average.

6.4. Data Cuts

Using the 50,000 event subset, various quantities used to separate the protons and antiprotons from other particles were examined and limits set with which we could cut out unwanted events. Calculated variables in the DAT array, using limits found from the small subset of flight data, were used to isolate the "best" proton and antiproton events from the entire body of flight data. These cuts are quite strict, perhaps overly strict, but since these cuts were applied equally to the positive and negative events, the antiproton/proton ratio would be unaffected. This overstrictness caused us to lose many good events and this must be corrected in the future.

A total of ten cuts were made to the data. I will summarize each of these.

The first cut was that a good rigidity fit, as flagged by DAT(191), was achieved from the measured trajectory in the multiwire proportional counters in the magnet spectrometer.

Cut number 2 was that the chi-squared fit of the particle's trajectory through the MWPC's in the x and y axes is good, eliminating scattering events. For the x direction, chi-squared must be less than 6. For the y axis, chi-squared must be less than 1.5. The chi-squared distributions of the 50,000 event subset are shown in Figs. 30 and 31. The differing scale of chi-squared distributions in x and y are due to the different number of working MWPC planes.

The third cut requires that the pulse-height from the scintillating counter S2 indicates a particle exiting the bottom of the Cherenkov counter, eliminating particles that may range out in the FC72 fluid or miss the Cherenkov counter. Looking at the output from S2 in Fig. 32, we arbitrarily set a limit that particles with pulse heights less than channel 40 were not within the main Z=1 "peak", broad as it is. Thus, the pulse height must be greater than channel 40. This will also include any particles that saturated the PMT output as it passed down through the center of S2 and the PMT face below. This arbitrary limit was used on both positive and negative events, leaving the antiproton/proton ratio intact.

We then looked at the output of scintillating counter S1. There, a well-defined Z=1 peak is more apparent, as can be seen in Fig. 33. To insure that a single, Z=1 particle (no multiple particles, no showers, no alphas) enters the experimental stack, we required the S1 output to be within this central peak. We thus required S1 PHA to be within channel 64 and 200. No obvious alpha peak was seen, using S1 alone.

The fifth cut was that the Cherenkov counter output must be consistent with a heavy particle. That is, the Cherenkov intensity should be less than approximately half the maximum intensity. To set the exact upper limit, I looked at the Cherenkov output for negative rigidities. For reasons explained in the next section, I looked at the square root of the gang Cherenkov signal for negative rigidities

$$-2 < \frac{1}{R} < 0 \ (GV)^{-1} \quad .$$

In this range, I should be looking at only a very few antiproton events and mostly electron, muon and pion events that radiate maximum Cherenkov intensity. This output is shown in Fig. 34. We set a limit requiring $\sqrt{I_c} < 24$. This condition eliminated the electron, muon, and pion peak.

The sixth cut requires the particle to pass through the body of the Cherenkov counter. Any particle normally producing the maximum intensity of Cherenkov light that traverses only part of the total counter thickness (exiting out one side of the counter) would produce a deceptively low light level. To test whether this limit was sufficient, I did several runs where I required chi-squared x be less than 6, chi-squared y be less than 1.5, S2 PHA be greater than 40, and 64 < S1 PHA <200 (the cuts already discussed). I also required the Cherenkov counter response be low and $1/|R| < 2 \ (GV)^{-1}$, so that I was looking predominantly at the more massive proton and antiproton candidates. I then varied the allowable x and y values for the particles' trajectories through the Cherenkov counter and looked at those surviving events with positive and negative rigidities. These events should correspond to proton and antiproton candidates with background. Then, as I

decreased the boundary limits, I checked the apparent antiproton/proton ratio. When the x, y limits are at the physical dimensions of the counter and additionally decreased so that only a small section of the counter area is used, the antiproton/proton ratio remains the same. That is, if we restrict the particles to some inner region of the counter, both proton and antiproton candidates falling outside this region are equally disqualified and the ratio remains the same. Thus, cut #6 requires the particle to pass within the physical boundaries of the Cherenkov counter. That is,

$$1.9 \text{ cm} < x < 45.7 \text{ cm}$$

and

$$1.7 \text{ cm} < y < 45.5 \text{ cm}.$$

For cuts #7 and #8, I used calculations performed by TDCCOM for the TOF system. Although the values of beta as calculated from the Goddard TOF system are not accurate enough to distinguish protons from pions at energies greater than 500 MeV, the overall sign of beta can be distinguished. Thus, it is possible to determine the direction of travel for particles traversing the experimental stack, eliminating albedo protons traveling upwards through the apparatus mimicking an antiproton. To insure a downward traveling particle, cut #7 required that beta, as determined by the TOF system, be greater than zero.

We also required that the velocity as calculated from the particles' rigidities (from the MWPC's) and from the time-of-flight must be consistent within specified limits, screening out suspicious events where the two methods did not agree. To do this, we calculated a quantity $\Delta\beta$.

$$\Delta\beta = \beta_{TOF} - |\beta_{Rig}| \tag{6.9}$$

where β_{TOF} is the time-of-flight beta, $|\beta_{Rig}|$ is the absolute value of beta as calculated by the MWPC value for rigidity, assuming a proton mass. The reason for the absolute value is that while the TOF beta is positive for both protons and antiprotons traveling downwards (negative for both protons and antiprotons traveling upwards), the rigidity beta is negative for protons traveling upwards or antiprotons traveling downwards (positive for protons traveling downwards or antiprotons traveling upwards). This cut insures that if the velocity as seen by the MWPC's and the TOF system are nearly equal, $\Delta\beta$ should be very small. The actual behavior of $\Delta\beta$ for the subset events is shown in Fig. 35. To insure this consistency, we require

$$-0.075 < \Delta\beta < 0.050 \quad .$$

The ninth cut was to limit the particles to rigidities in the Cherenkov counter's range. Initially, the cuts were quite broad, i.e.

$$-2(GV)^{-1} < \frac{1}{R} < 2\ (GV)^{-1} \quad .$$

This corresponded to the absolute value of the rigidity greater than 0.5 GV/c or proton kinetic energy greater than about 125 MeV. The rigidity was calculated from MWPC data. The particle's inverse rigidities are shown in Fig. 36. More on the rigidity is discussed in the next section.

The tenth cut was based on the particle's mass as calculated from the

Cherenkov counter output and the spectrometer rigidity. From equations (5.1) and (5.7),

$$\left| \frac{mc^2}{Z} \right| = \sqrt{\left[1 - \frac{I_c}{I_{c,max}}\right]} \left[\frac{n^2-1}{\eta^2}\right] , \qquad (6.10)$$

where mc^2 is the particle's mass, Z is the charge, I_c is the Cherenkov counter response, $I_{c,max}$ is the maximum Cherenkov counter response, n is the index of refraction, and η is the inverse rigidity. The Cherenkov mass response after cuts #1 through #9 have already been taken is shown in Fig. 37. Because of the uncertainty in the rigidity and the photon statistics, I again made the mass cut quite loose:

$0.4 \text{ GeV} < mc^2 < 1.25 \text{ GeV}.$

I later tried a much stricter mass cut. While that eliminated some antiproton candidates, it also eliminated proton events, leaving the antiproton/proton ratio unchanged.

6.5. Uncorrected Results

With these ten cuts, I ran the entire flight data through the software. Five antiproton candidates were found among 71,940 proton candidates. However, all of the antiproton candidates had high values of beta (time-of-flight beta greater than 0.779). To narrow this range of kinetic energies (125 MeV < E_p < 1 GeV), I made one additional cut - I required the TOF beta be greater than 0.75 which

corresponded to a lower kinetic energy range of 480 MeV. I chose to make the lower cut with the TOF beta rather than the beta as calculated from the rigidity simply because both quantities were relatively inaccurate and so either cut was only approximate. The TOF system is not calibrated for these energies and there seems some smearing of the rigidity determination, as discussed later in regards to the particle ellipses. With the square root of the Cherenkov output less than channel 24 (and a maximum Cherenkov light output at channel 1028), the upper limit is at a kinetic energy limit of 1168 MeV. Thus,

$$480 \text{ MeV} < E_p < 1168 \text{ MeV}$$

is the kinetic energy range at the Cherenkov counter level of the apparatus.

When this last TOF beta cut is applied, I have five antiproton candidate events in 43,098 proton candidates. These five candidates are shown in Table 3. However, both events #5 and #3 are suspiciously close to the Cherenkov counter edge. The other three events occur more than one centimeter away from any counter edge. Since the particle-path fit is accurate only to one centimeter (Golden, private communication), I will throw out these two events as being somewhat suspicious. This then leaves me with three possible antiproton events.

To throw out these antiproton events, I must then throw out the proton events that also pass through the counter less than one centimeter from an edge. Of the original 43,098 proton candidates, 41,514 events pass through the counter atleast one centimeter away from any counter edge.

It would require getting all systems calibrated to their utmost to positively identify these three events as antiprotons. This development is still some time

away. However, assuming these events to follow a Poisson distribution, it is possible to calculate an upper antiproton/proton ratio limit. Since the Poisson probability distribution for n events is

$$P(n) = \frac{\mu^n}{n!} e^{-\mu} \tag{6.11}$$

the probability of observing three or fewer antiproton events is

$$P(\leq 3) = \left[1 + \mu + \frac{\mu^2}{2} + \frac{\mu^3}{6}\right] e^{-\mu} \tag{6.12}$$

for a mean value μ of the ratio. The 90% confidence level is that value of the mean μ where the probability shown above is 0.10. That occurs at $\mu = 7$ events. A naive antiproton/proton ratio upper limits would then be 7/41514 or 1.69×10^{-4} in this kinetic energy range.

In the lower energy range, a separate data analysis was performed (Streitmatter et al., 1989). No negative curvature events were found in 92,200 proton events in an energy range

$$120 \text{ MeV} < E_p < 360 \text{ MeV},$$

corrected to the top of the atmosphere. This gives an 90% confidence upper limit (uncorrected) of

$$2/92{,}200 = 2.2 \times 10^{-5}.$$

For both results, several corrections must be made to arrive at a final antiproton/proton ratio. In the next few sections, I will discuss these adjustments to the data.

6.6. Corrections to the Particles' Kinetic Energy Measurement

An interesting way of looking at the Cherenkov counter response as a function of the spectrometer rigidity is in the form of particle ellipses. Now the rigidity R is

$$R = \frac{Pc}{Ze} = \frac{mc^2}{Ze}\,\gamma\beta$$

where (6.13)

$$\gamma = 1/\sqrt{1-\beta^2} \quad .$$

From equation (5.4), the Cherenkov response I_c can be written as

$$I_c = k\left[1 - \frac{1}{\beta^2 n^2(\mathrm{ref})}\right] \tag{6.14}$$

where k is a constant in this situation. Combining equations (6.13) and (6.14),

$$I_c = A\left[B - D\,\frac{m^2}{z^2}\,\eta^2\right]$$

where

$$\eta = \frac{1}{R} \quad , \quad A = \frac{k}{n^2} \quad , \quad B = n^2 - 1 \quad , \quad \text{and} \quad D = \frac{c^4}{e^4}$$

(A, B, and D constants in this case). Then,

$$\sqrt{I_c} = \sqrt{A\left[B - D\,\frac{m^2}{z^2}\,\eta^2\right]} \tag{6.16}$$

which can be rewritten as

$$(\sqrt{I_c})^2 + \left[AD\,\frac{m^2}{z^2}\right]\eta^2 = AB \tag{6.17}$$

which is an ellipse. For particles of differing masses and charges, the theoretical ellipses are shown in Fig. 38.

An example of the actual ellipses seen in our instrument during flight and after the cuts above are applied is shown in Fig. 39. It is evident that there is a source of random error that decreases the sharpness of the proton ellipse; a broadening is occurring. A part of this broadening is due to the photon statistics (discussed earlier). However, such an effect would only broaden the ellipses in the vertical. It is obvious there is some fuzziness occurring in the horizontal direction also. This leads me to the conclusion that the uncertainty in the rigidity from the spectrometer also plays a part in the ellipse broadening.

The moral to all this is that the kinetic energies reported, derived as they are from the spectrometer rigidity, cannot be treated as absolutes. More accurate spectrometer data will be available in the future from a more careful analysis of the MWPC's and spectrometer characteristics by Golden's group. In the meantime, these rigidities will only be used to find the general energy range of the detected particles.

As stated previously, the $\sqrt{I_c} < 24$ cut sets the upper energy limit in the Cherenkov counter as 1168 MeV. The TOF beta > 0.75 cut gives a rough lower energy limit of 480 MeV.

Now, as the particles travel through the atmosphere and the experimental apparatus, they suffer ionization energy loss. I calculated the amount of energy loss expected for protons by dividing the 5 g/cm^2 of atmosphere above the gondola and the various grammages of other materials in the experimental stack into 1000 thin slabs. For each slab, I calculated the energy loss (Particle Properties Data Booklet, 1986) and followed the particle through the experiment in that manner, keeping track of the particles' energies as they traveled through this material. I then found that a 500 MeV particle at the top of the atmosphere would have a 480 MeV energy within the TOF system. That set the lower energy limit as 500 MeV, corrected to the top of the atmosphere. Also, a 1200 MeV particle at the top of the atmosphere would possess 1168 MeV within the FC72 fluid, setting a 1200 MeV upper limit. Adding a zenith angle to the particle's trajectory of up to 15^0 did not affect the results by more than 1%.

Thus, the kinetic energy range for our data, corrected to the top of the atmosphere is

$$500 \text{ MeV} < E_p < 1200 \text{ MeV}.$$

6.7. Atmospheric Corrections to the Apparent Antiproton/Proton Ratio.

The eventual figure for the observed antiproton/proton ratio must be corrected for various sources of systematic error due to the environment in which LEAP operated. The measured antiproton/proton ratio result will be affected by several

possible sources of contamination or alteration by the atmosphere above the experiment (about 5 gm/cm^2) and the experimental apparatus itself.

One possible contamination is the flux of secondary antiprotons produced in proton-proton collisions of high energy cosmic-ray protons or nuclei colliding with nitrogen or oxygen nuclei in the atmosphere. These secondary antiprotons, though predominately produced higher in energy than the low-energy antiprotons we are observing, could enter our energy range through inelastic, non-annihilating collisions subsequent to their production. Using the computer simulation discussed in Chapter 3 (Bowen and Moats, 1986), we calculated the expected antiproton flux of these secondaries at LEAP due to the 5 gm/cm^2 of atmosphere above the gondola and the 4 gm/cm^2 of aluminum and plastic contained in the gondola above the MWPC's. Any such interaction at the MWPC level or below would cause that track to be rejected by the cuts already discussed. This is especially true of the chi-squared cuts on the trajectory, the rigidity cuts, and the $\Delta\beta$ cuts which insure a one-particle event with a well-defined smooth path in our low kinetic energy range.

To accomplish this, I ran the simulation to obtain the atmospheric differential secondary antiproton flux as a function of kinetic energy for a total of 9 gm/cm^2 of air. For this purpose, treating the 4 gm/cm^2 of gondola apparatus as air was sufficient. I calculated the antiproton/proton ratio so that any difference in the actual primary proton flux at the top of the atmosphere and the primary proton flux used in the simulation would make very little difference in the output as long as the basic shape of the spectra was similar (a reasonable assumption). Since I obtained a differential spectrum, it was necessary to numerically integrate the simulation result over the appropriate kinetic energy range.

For the Cherenkov energy range of 500 MeV to 1.2 GeV at the top of the

atmosphere, the secondary antiproton/proton ratio is 3.44 x 10^{-6}. For our measured number of protons (41514), the expected number of secondary antiprotons is 0.143. Thus, atmospheric secondary antiprotons do not cause a significant problem in our energy range.

Another set of corrections are due to differential antiproton/proton absorption and antiproton annihilation in the upper atmosphere and gondola. We used information from (Bowen and Moats, 1986) to calculate the pertinent pathlengths in the 500 MeV to 1.2 GeV range. Fig. 6 contains the information we used for this calculation. Using 90 gm/cm^2 as the interaction length of proton-air collisions and 50 gm/cm^2 as the interaction pathlength of antiproton-air collisions (including both annihilation and inelastic antiproton-air collision interactions), the correction factor for the antiproton/proton ratio is

$$C_{\bar{p}/p} = \frac{e^{-x/\lambda_{p\text{-air}}}}{e^{-x/\lambda_{\bar{p}\text{-air}}}} = 1.34 \qquad (6.18)$$

where λ is the interaction length and x is the amount of material traversed through the whole experiment down to the bottom scintillation counter S2 (33 gm/cm^2) which was treated as air as in the secondary atmospheric antiproton case previously. We included the entire 33 gm/cm^2, since any annihilation or absorption occurring before the particle enters S2 would disqualify that event from inclusion in our results.

It is necessary to evaluate the contribution to the uncertainty in the antiproton/proton ratio from this correction factor. From Fig. 6, I estimated the error in $\lambda_{p\text{-air}}$ to be +/- 5 gm/cm^2, giving a lower bound of 85 gm/cm^2. That introduced a fractional error of 0.0213.

For $\lambda_{\bar{p}\text{-air}}$, I estimated a lower bound of 42 gm/cm^2. Thus, the fractional error is 0.1181.

Adding errors in quadrature, the fractional error in $c_{\bar{p}/p}$ is

$$e\,(c_{\bar{p}/p}) = \sqrt{(e_{p\text{-air}})^2 + (e_{\bar{p}\text{-air}})^2} = 0.12 \qquad (6.19)$$

The total error is (1.34) (0.12) = 0.16. Thus, the correction factor is 1.34 +/- 0.16.

6.7. Final Result

Summarizing this section, then, the naive antiproton/proton ratio upper limit is 1.69×10^{-4} in the 480 MeV < T < 1200 MeV kinetic energy range. With a correction factor of 1.34 from antiproton annihilation and proton absorption in the atmosphere, the 90% confidence antiproton/proton ratio upper limit is

$$(1.69 \times 10^{-4})\quad 1.34 = 2.3 \times 10^{-4}$$

in a kinetic energy range of

$$500\ \text{MeV} < E_p < 1.2\ \text{GeV},$$

corrected to the top of the atmosphere.

With 72.2 photoelectrons, the standard deviation is 8.5. However, due to the multiplicative ratio R_{PMT} at each PMT dynode, a factor of

$$\left[\frac{R_{PMT}}{R_{PMT-1}}\right]^{1/2} \sim 1.3 \qquad (6.20)$$

must be taken into account, giving a standard deviation of 11 photoelectrons.

The levels of maximum light and 50% of that maximum are separated by 3.2 standard deviations. When combined with several of the other data cuts, specifically the $\Delta\beta$ cut (cut #8) and the Cherenkov mass cut (cut #10) which specifically separated protons from the lighter mass particles, I am confident that the low Cherenkov output is real.

The final result is shown in Fig. 40.

I will now briefly mention the TOF system results to date, analyzed by Dr. R. Streitmatter, Dr. J. Ormes, and S. Stochaj at Goddard Space Flight Center. These results are presented in more detail in (Streitmatter et al., 1989). As stated previously, they found no negative curvature antiproton events in 92,200 proton events in the energy range below 360 MeV (corrected to the top of the atmosphere), corresponding to a 90% confidence upper limit of 2.2×10^{-5}. After corrections for proton absorption and antiproton annihilation in the atmosphere and in the experimental stack, their corrected 90% confidence upper limit is

$$3.5 \times 10^{-5} \text{ for } 120 \text{ MeV} < T < 360 \text{ MeV}.$$

In the same fashion as I had done previously, I calculated the expected number of secondary antiprotons in their energy range to be negligibly small. This result is also shown in Fig. 40.

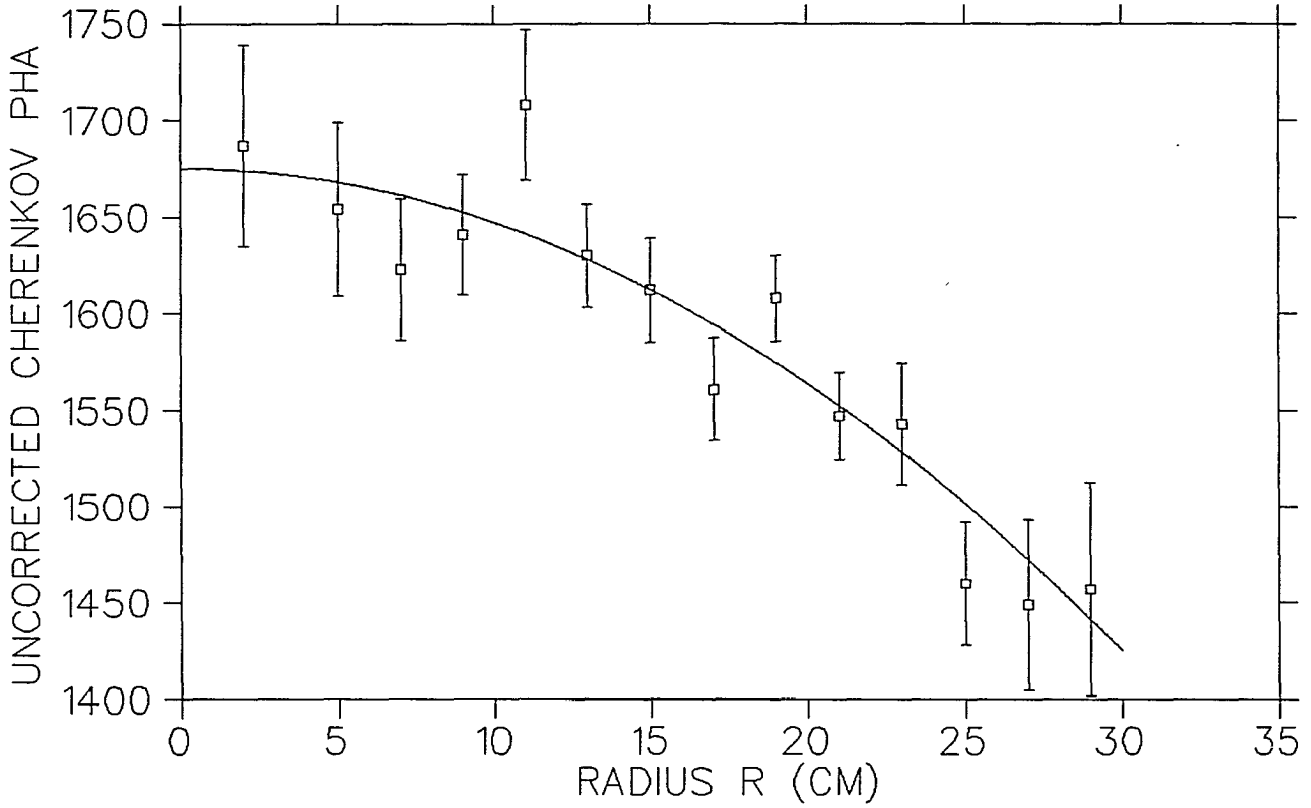

Fig. 19. The pulse height peak positions as a function of the radius R from the center of the Cherenkov counter (before calibration) for high rigidity events. The fitted correction function is shown as the solid curve.

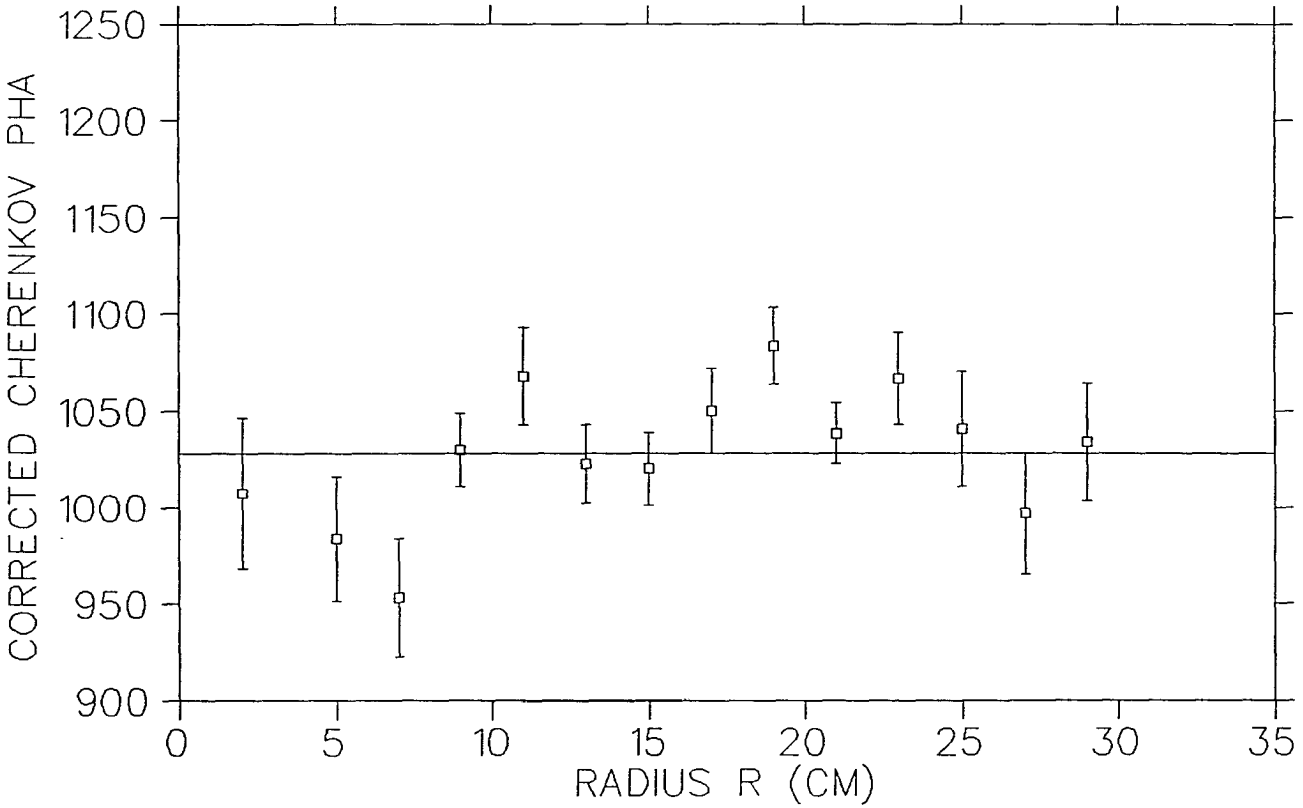

Fig. 20. The pulse height peak positions of the high rigidity events as a function of radius R from the center of the Cherenkov counter (after calibration). The average peak position is 1028 channels (shown by the solid line).

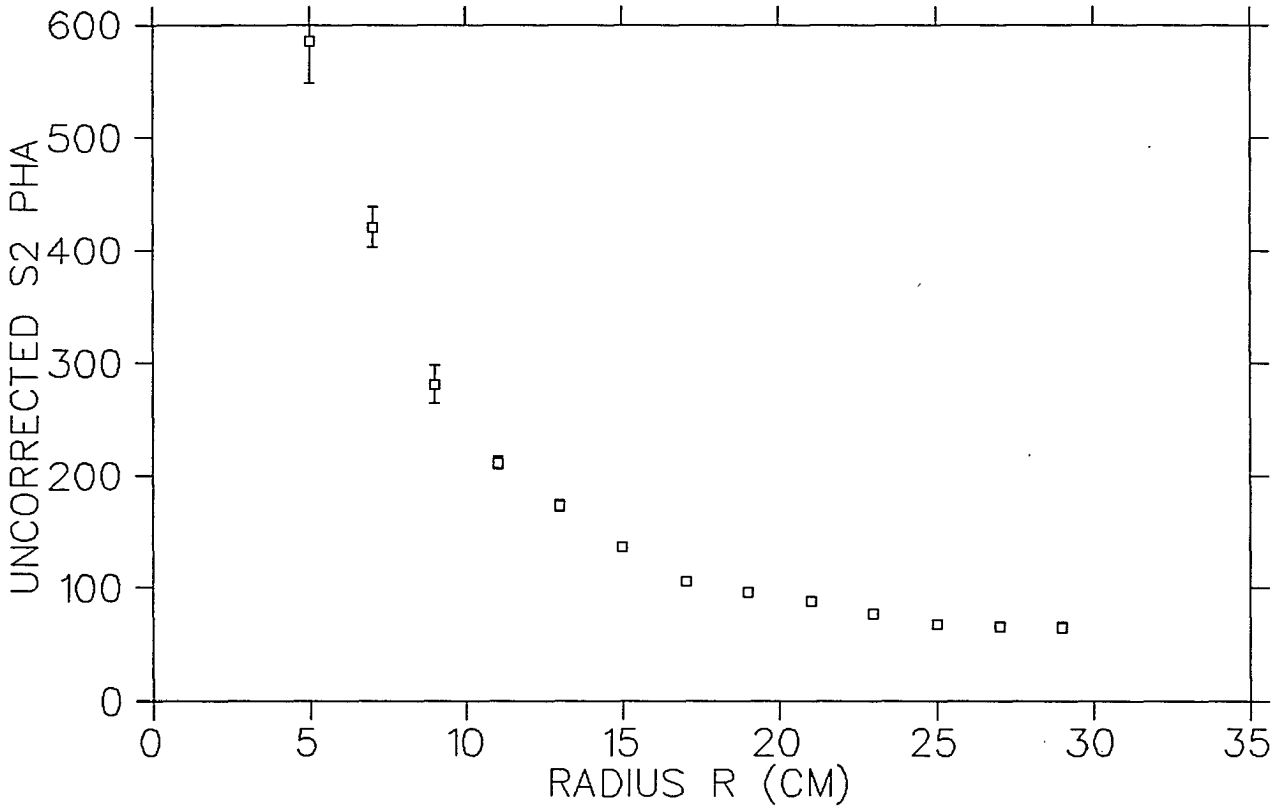

Fig. 21. The pulse height peak positions of the Z=1 peak as a function of the radial distance R from the center of the S2 counter (before correction).

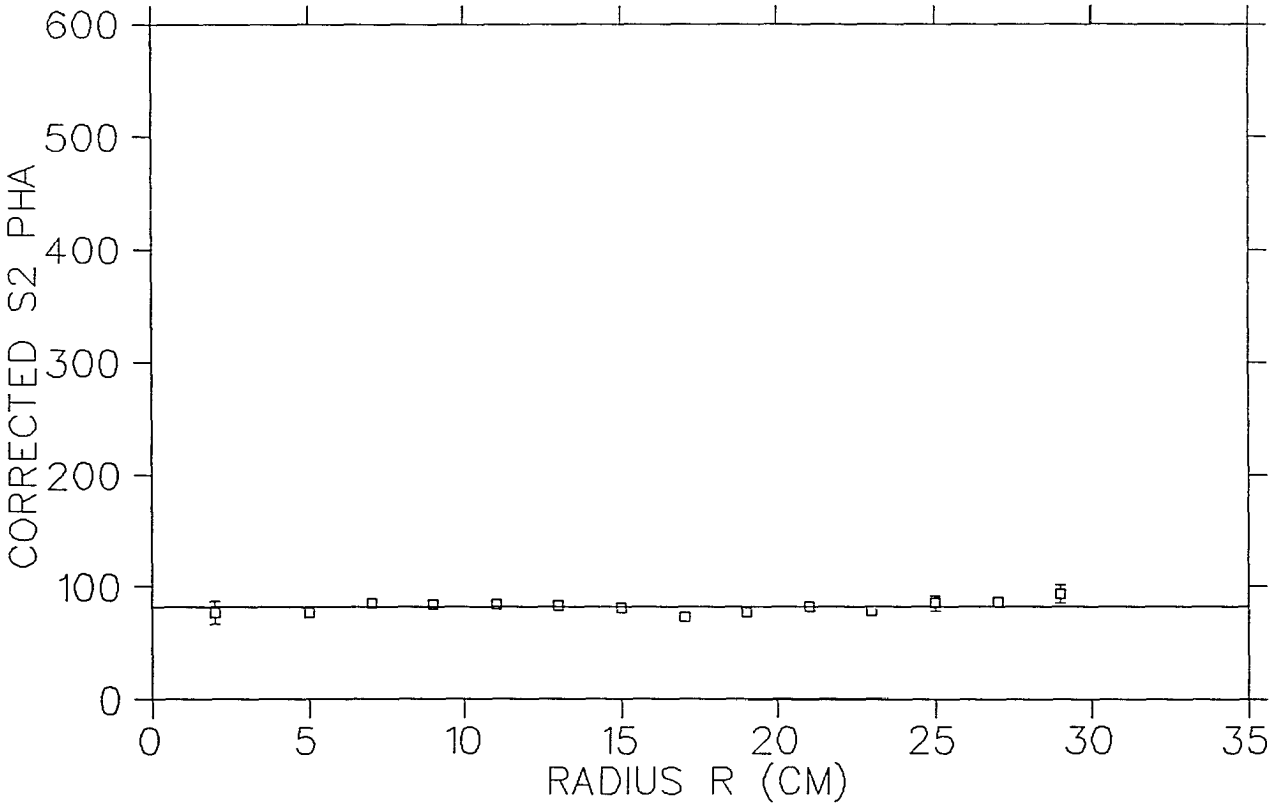

Fig. 22. The corrected pulse height peak positions of the Z=1 peak as a function of the radial distance R from the center of the S2 counter. The average peak position was at 81.8 channels (shown by the solid line).

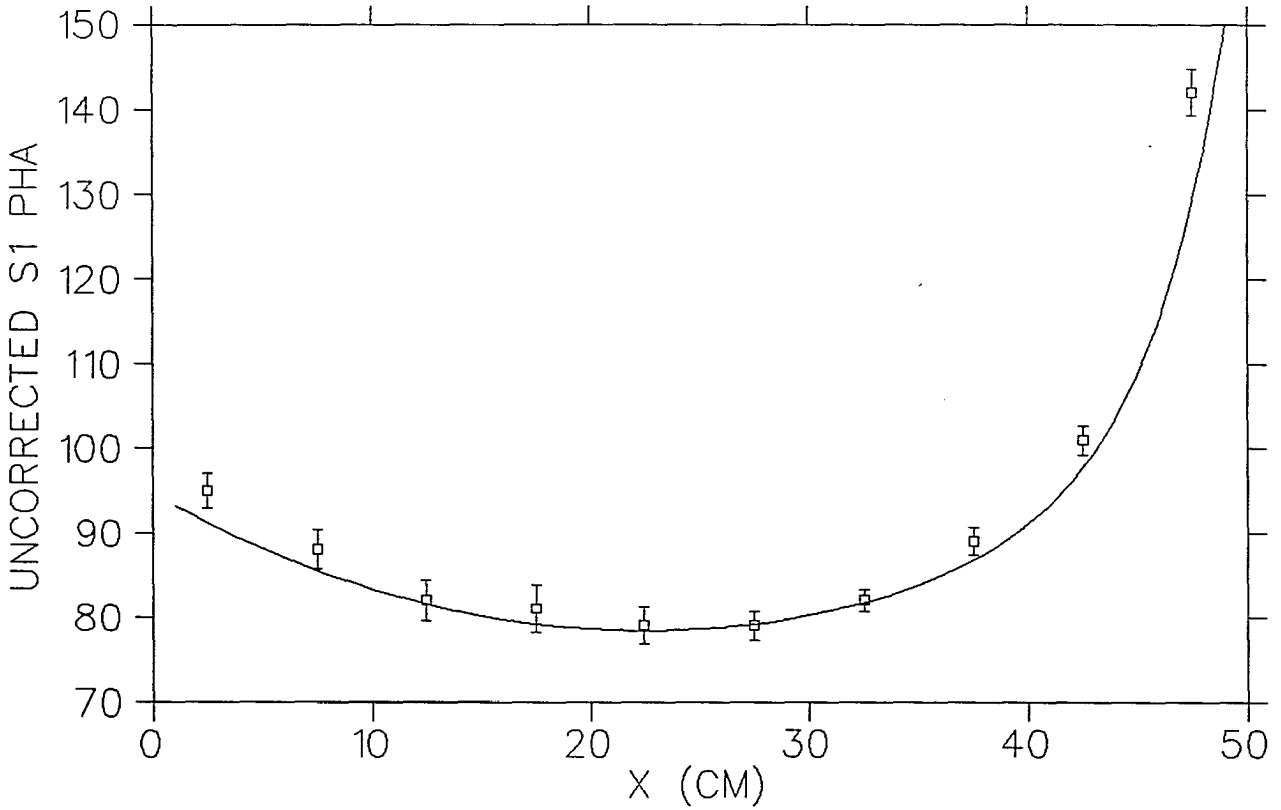

Fig. 23. The pulse height peak positions for the Z=1 peak as a function of x in the S1 counter (before calibration). The fitted correction function in the x direction is shown as the solid curve.

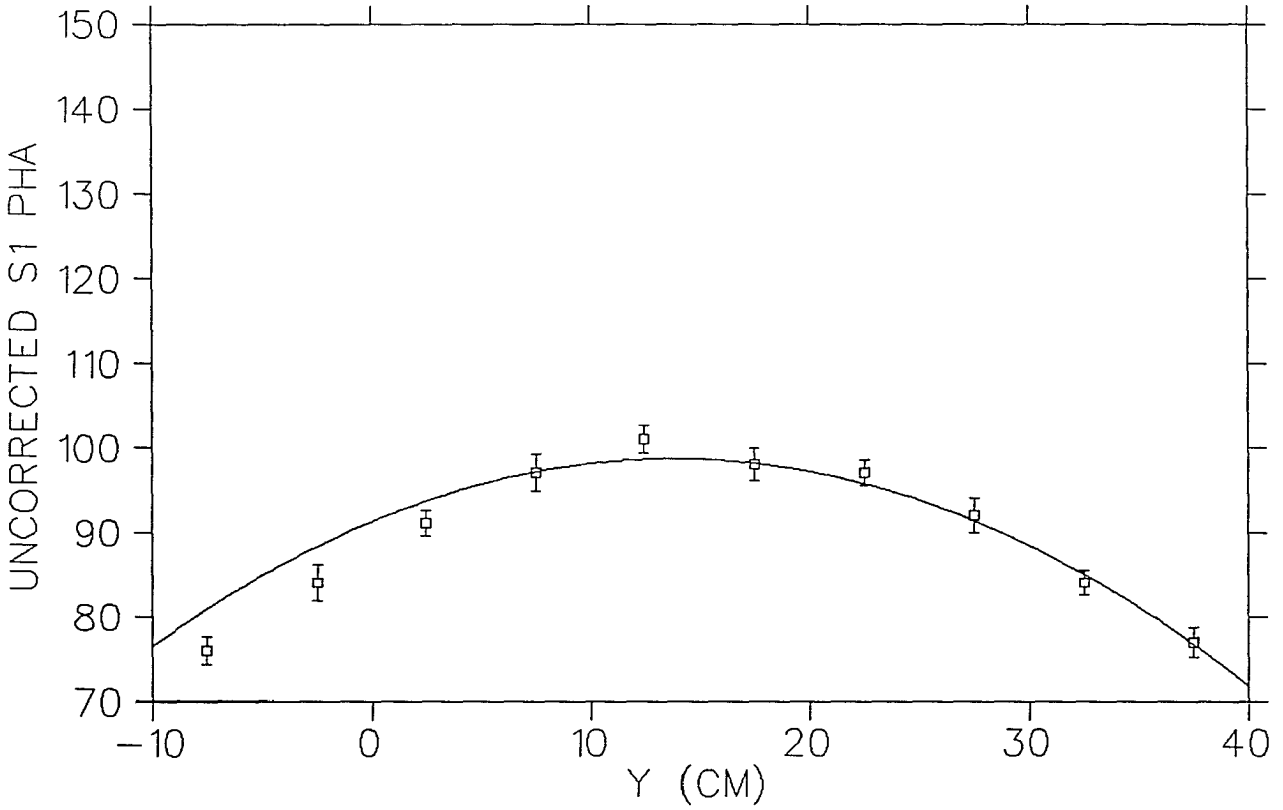

Fig. 24. The pulse height peak positions of the Z=1 peak as a function of y of the S1 counter (before calibration). The fitted correction function in the y direction is shown as the solid curve.

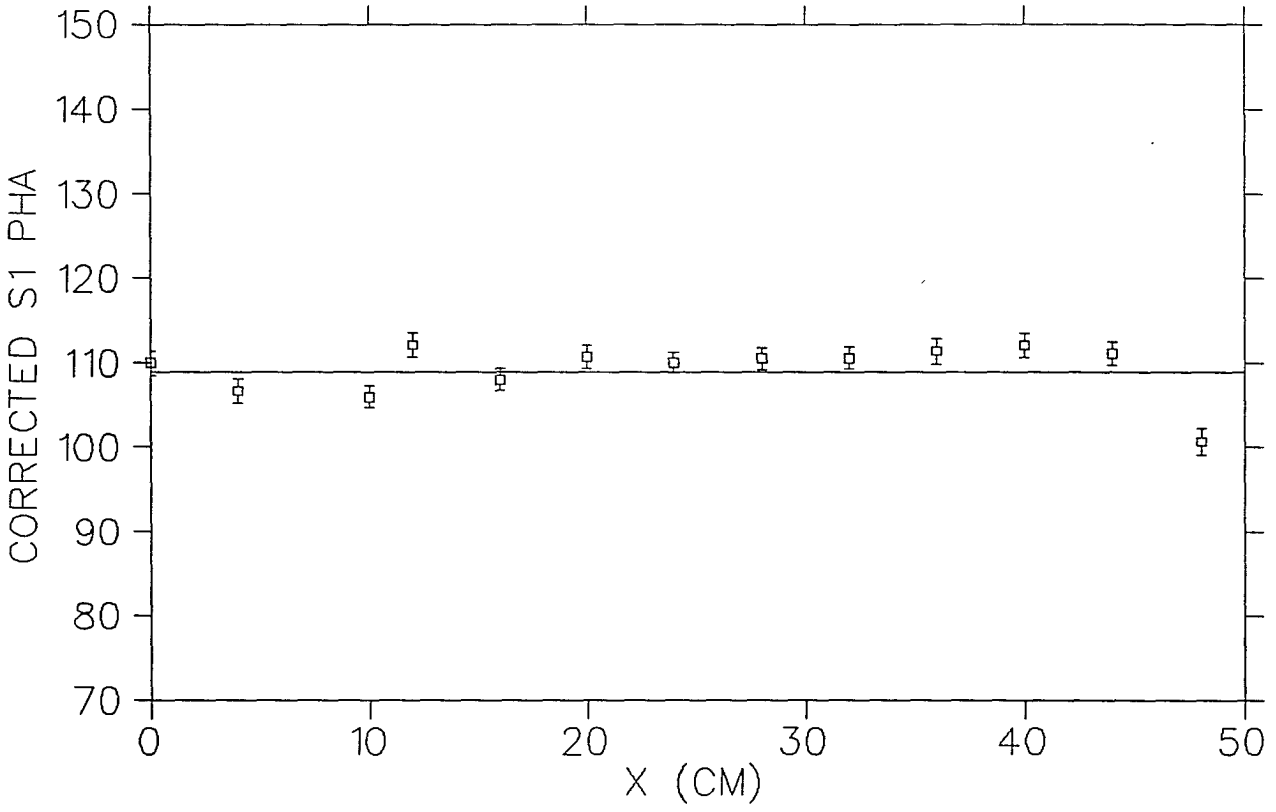

Fig. 25. The pulse height peak positions of the Z=1 peak as a function of x (after calibration) for S1. The peak position average of 109 channels is shown by the solid line.

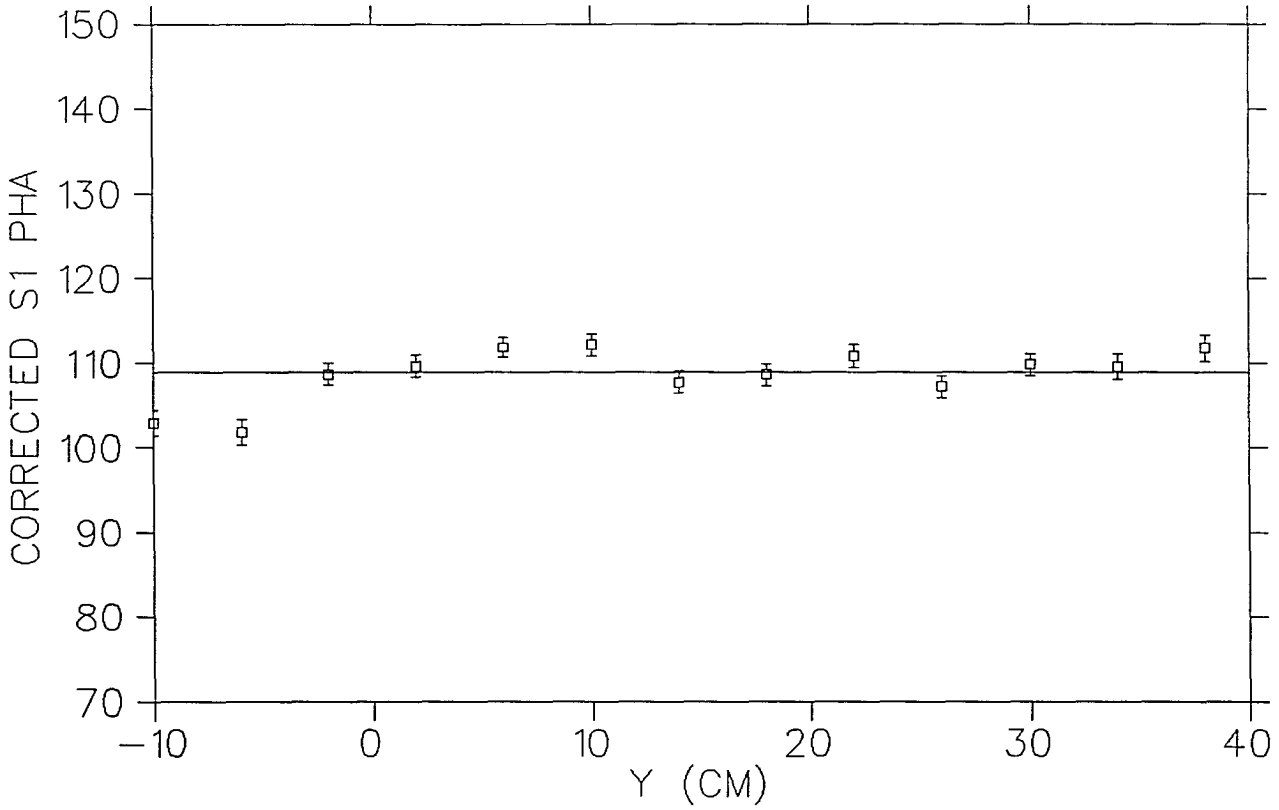

Fig. 26. The pulse height peak positions of the Z=1 peak as a function of y in the S1 counter (after correction). The average peak position of 109 channels is shown by the solid line.

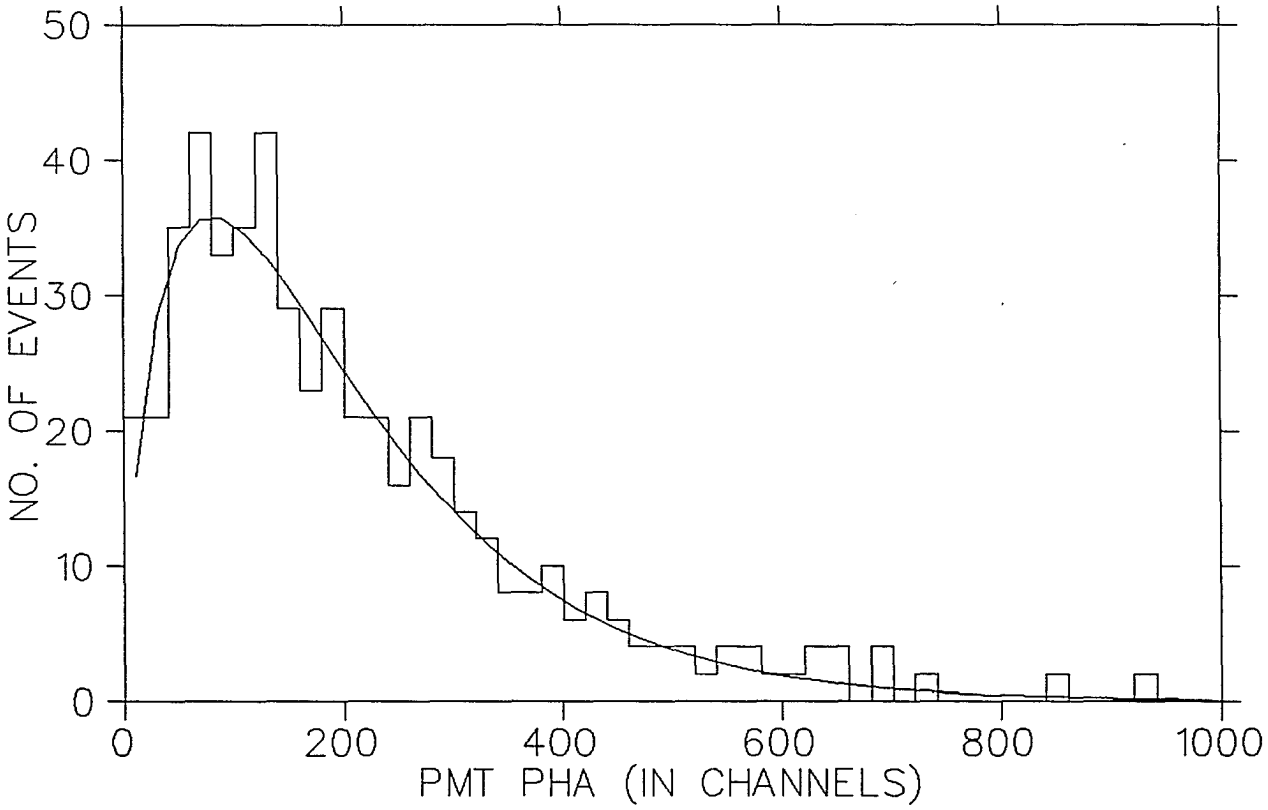

Fig. 27. An example of a single Cherenkov counter PMT pulse height distribution (the histogram) plotted against the corresponding Pearson's function fitted to the mean and standard deviation of the histogram.

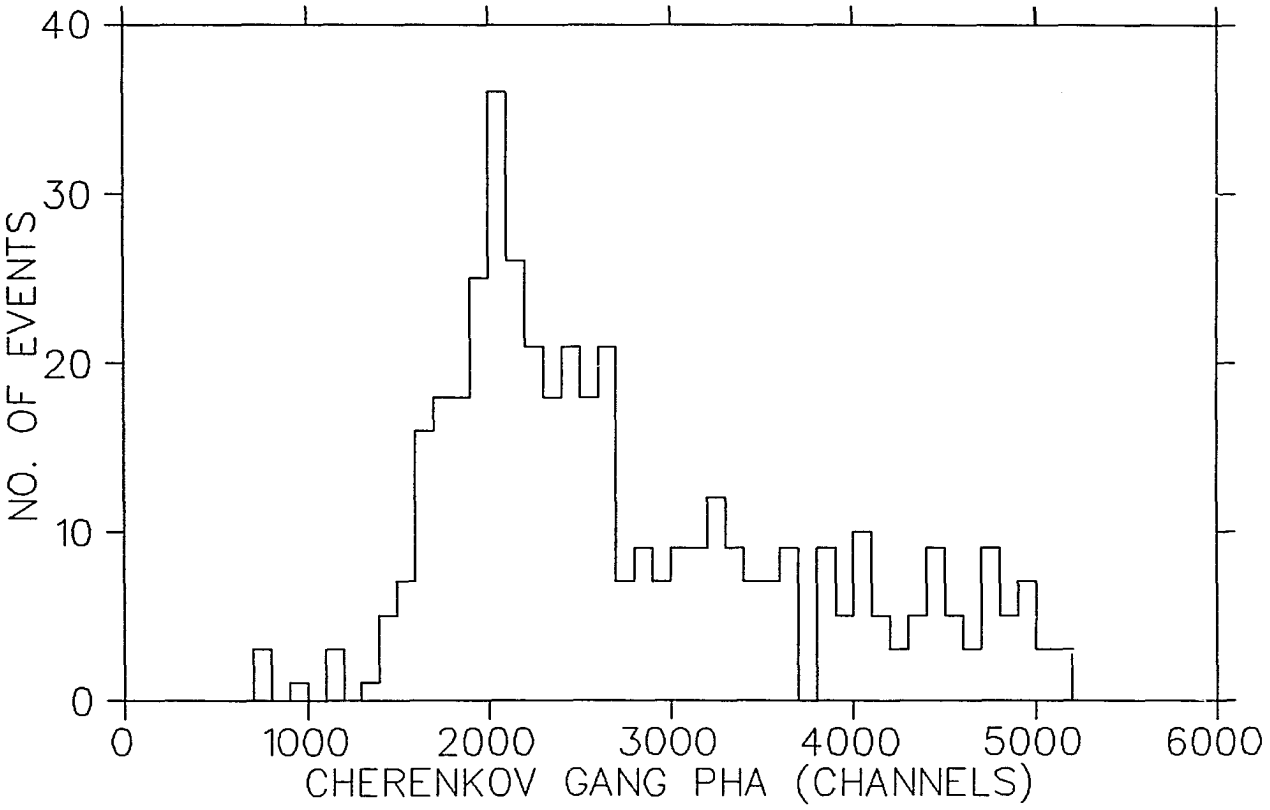

Fig. 28. The Cherenkov gang PHA from the central region of the counter for negative rigidities greater than 0.5 GV.

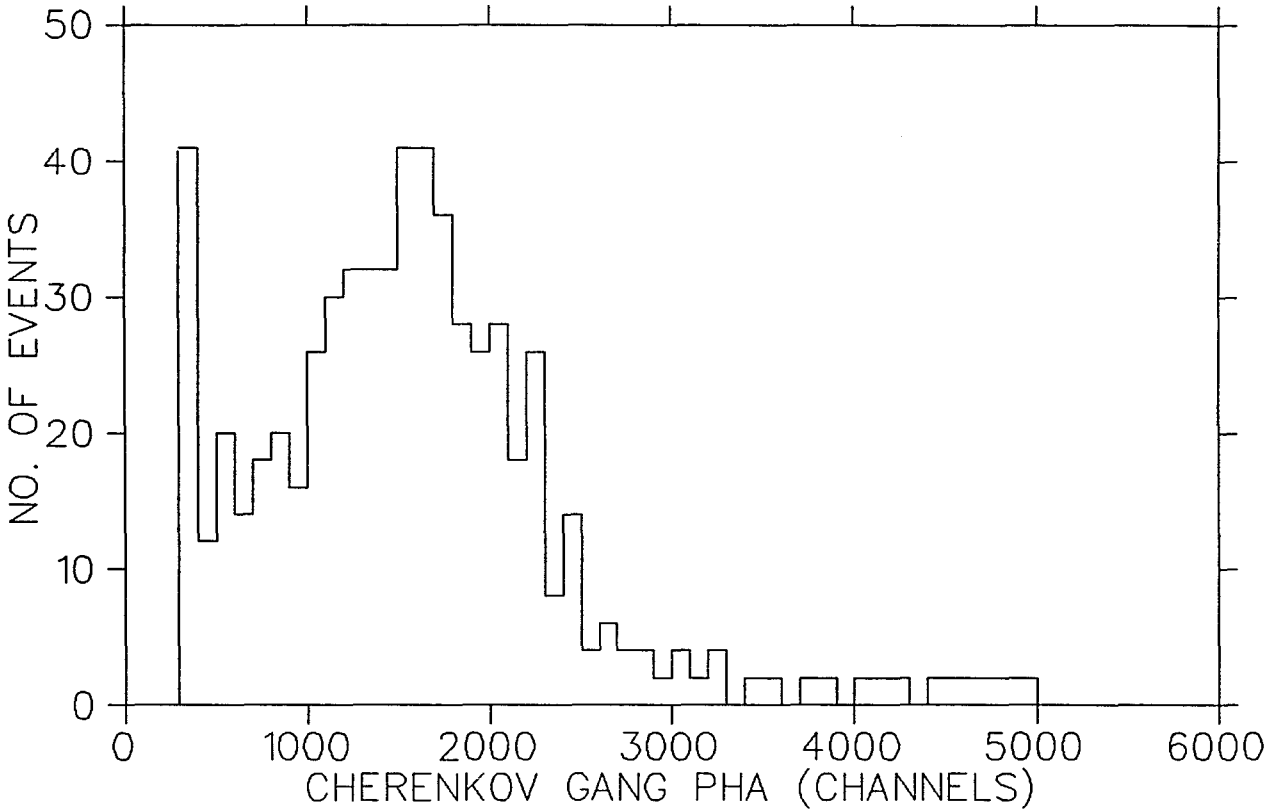

Fig. 29. The Cherenkov gang PHA from the central region of the counter for positive rigidities greater than 0.5 GV.

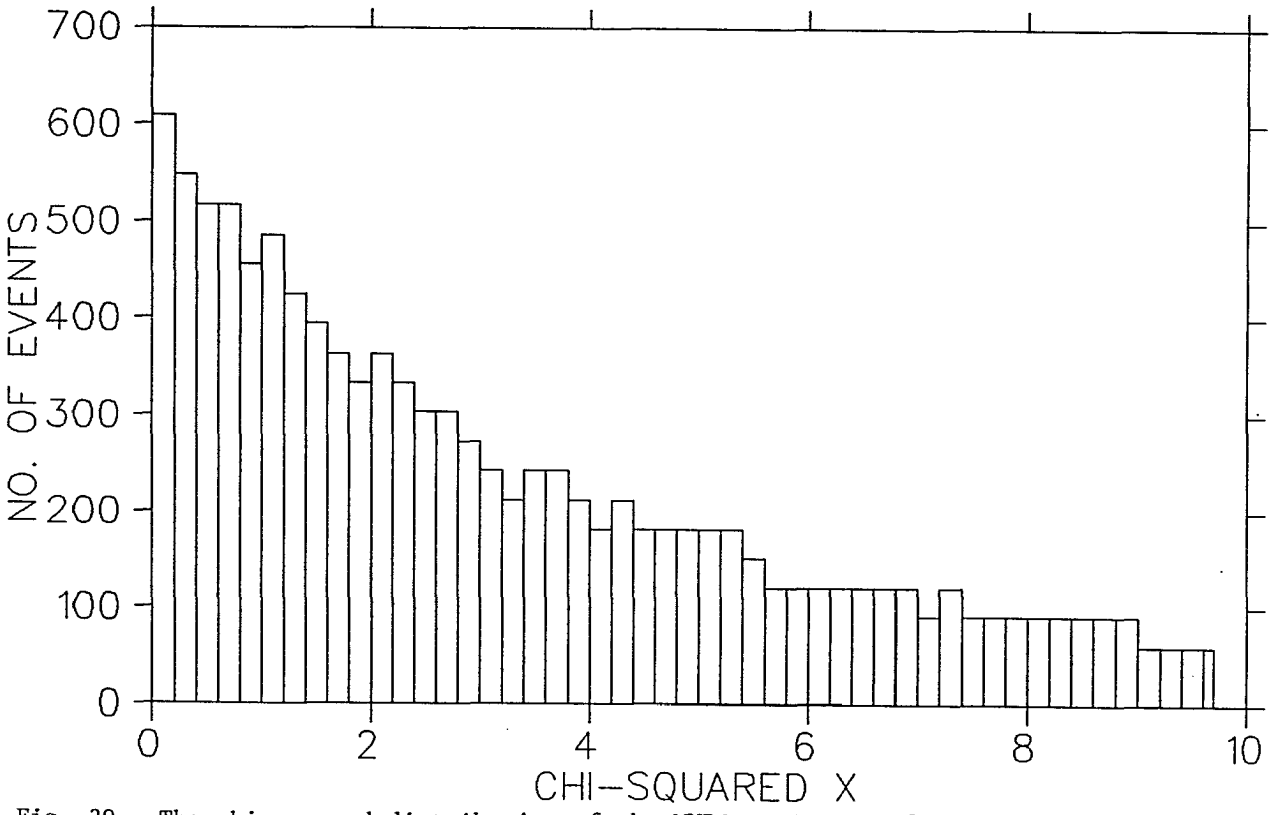

Fig. 30. The chi-squared distribution of the MWPC trajectory fits in the x direction for the 50,000 event subset. A total of 10,209 events are shown; 8309 events are offscale for chi-squared greater than ten. Only events where chi-squared were less than 6 were allowed for the antiproton search.

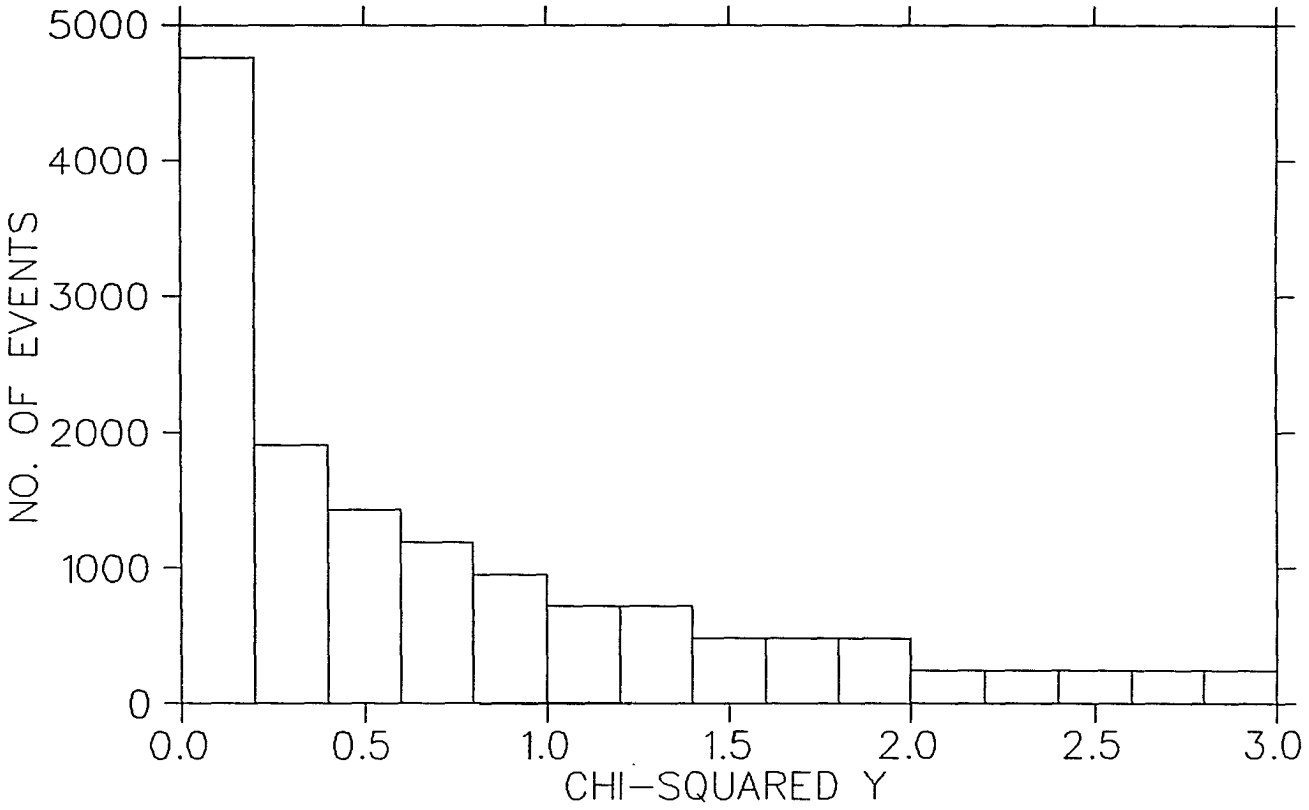

Fig. 31. The chi-squared distribution of the MWPC trajectory fits in the y direction for the 50,000 event subset. A total of 14,267 events are shown above; 4251 events are offscale with chi-squared greater than three. Only events where chi-squared was less than 1.5 were considered for the antiproton search.

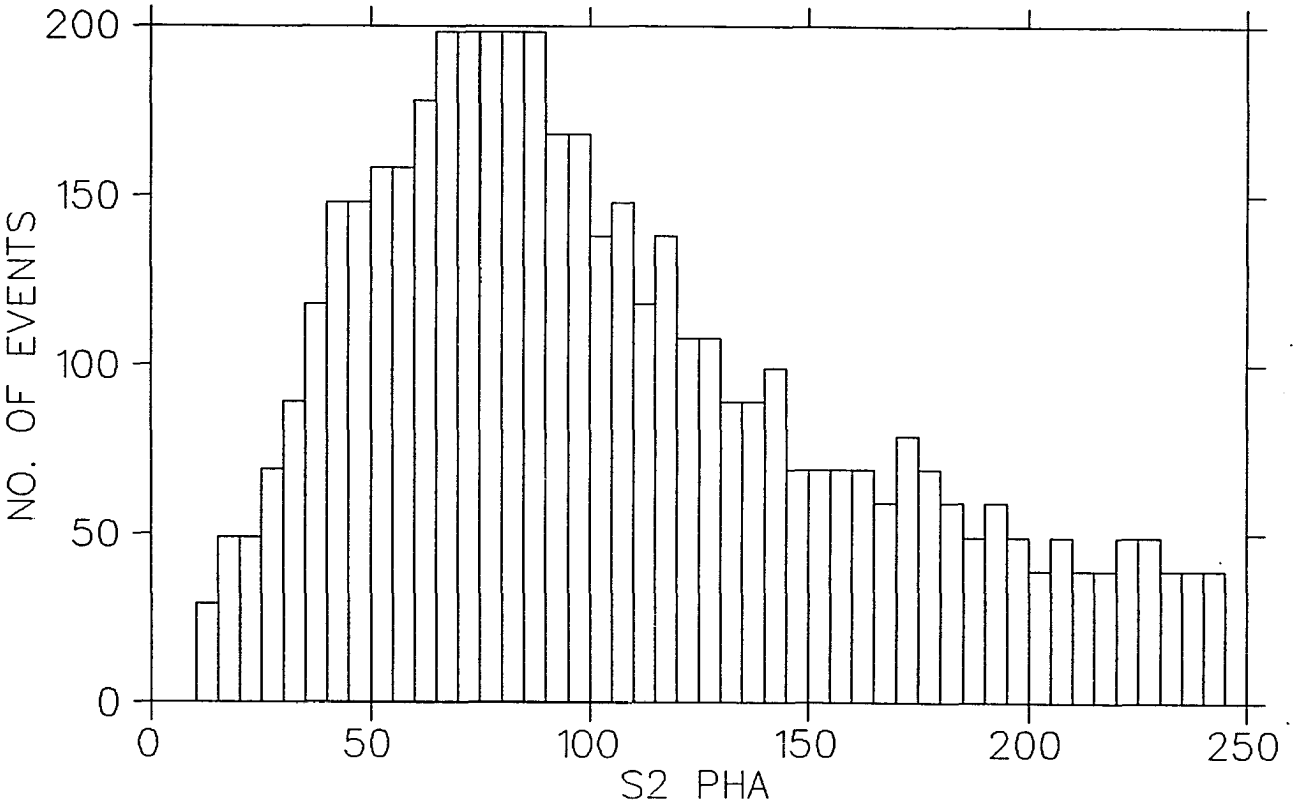

Fig. 32. The S2 pulse height distribution from the 50,000 event subset, exclusive of those saturating the PMT output. All events with S2 output less than channel 40 were excluded for the antiproton search.

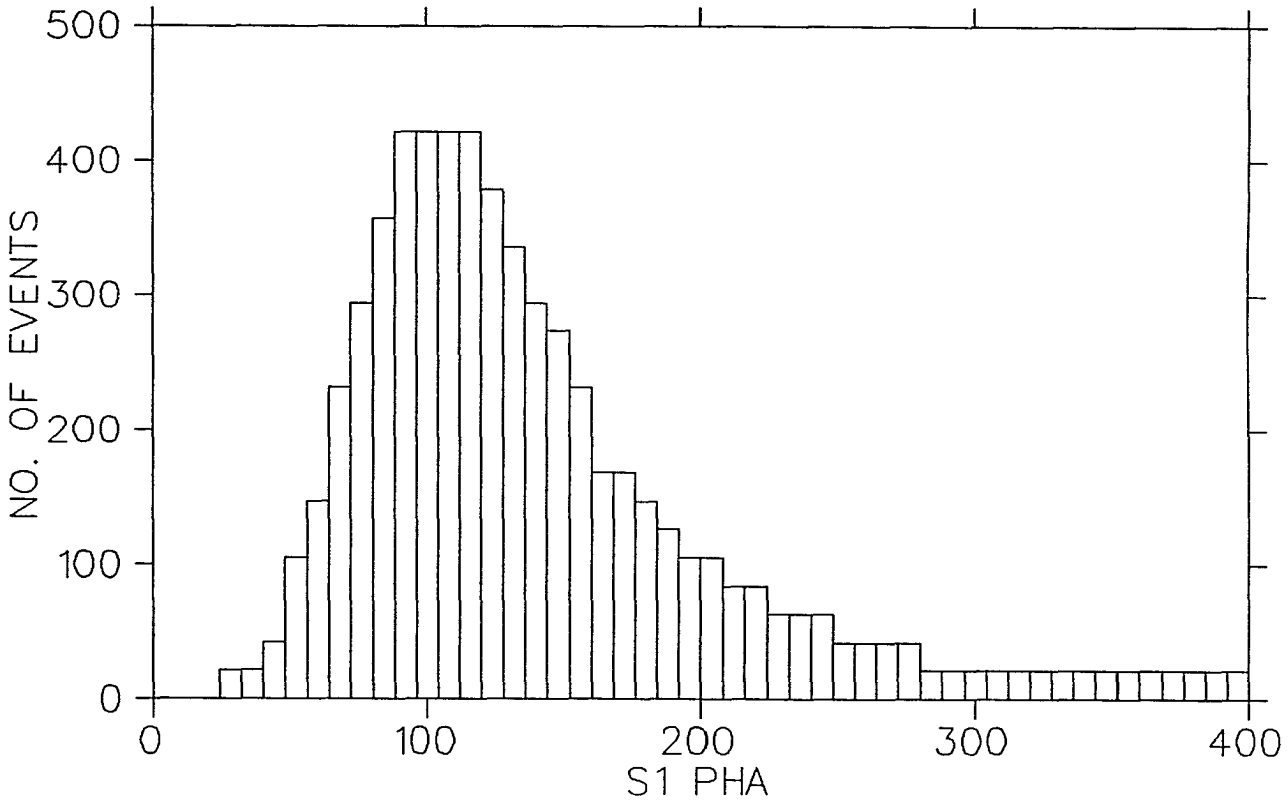

Fig. 33. The S1 pulse height distribution from the 50,000 event subset. We required the S1 signal to be between channels 64 and 200 for the antiproton search.

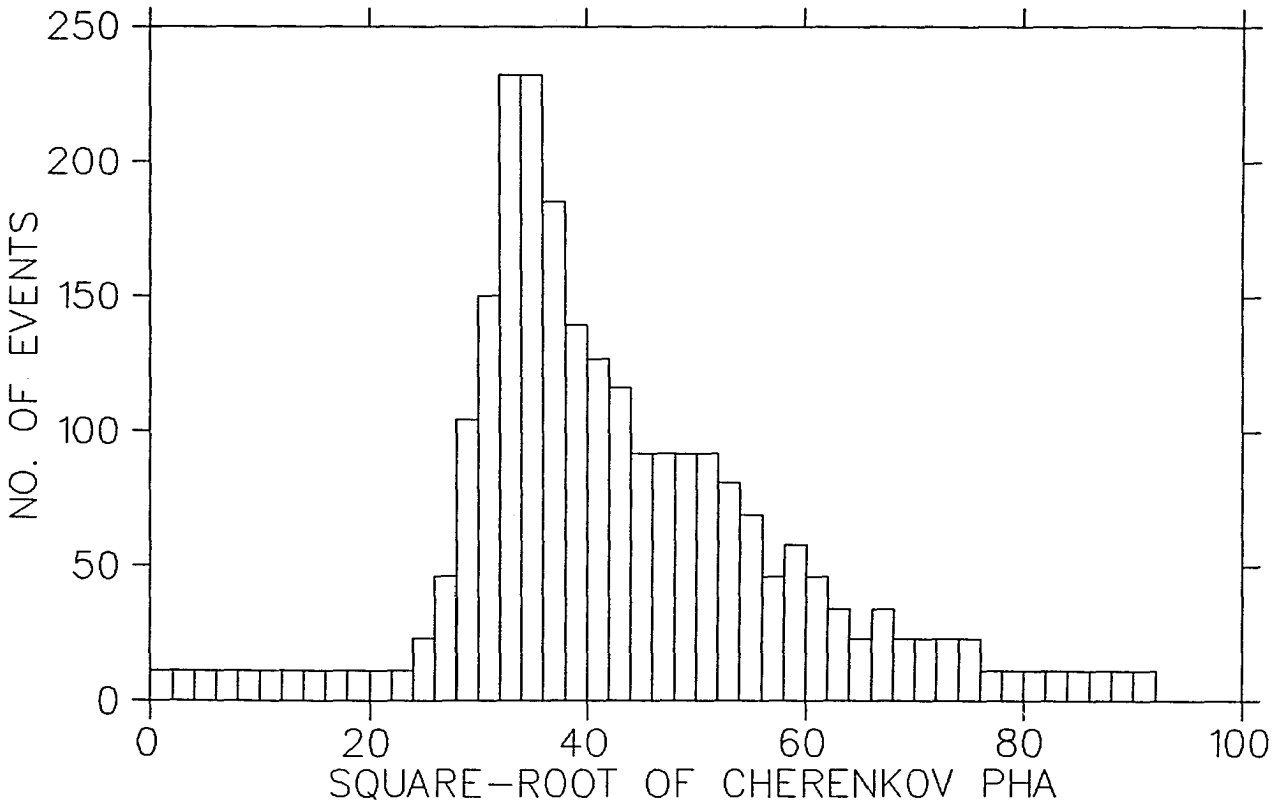

Fig. 34. The distribution of the square root of the Cherenkov counter response for the 50,000 event subset for negative rigidities between -0.5 GV and infinity. Only events less than 24 were included for the antiproton search.

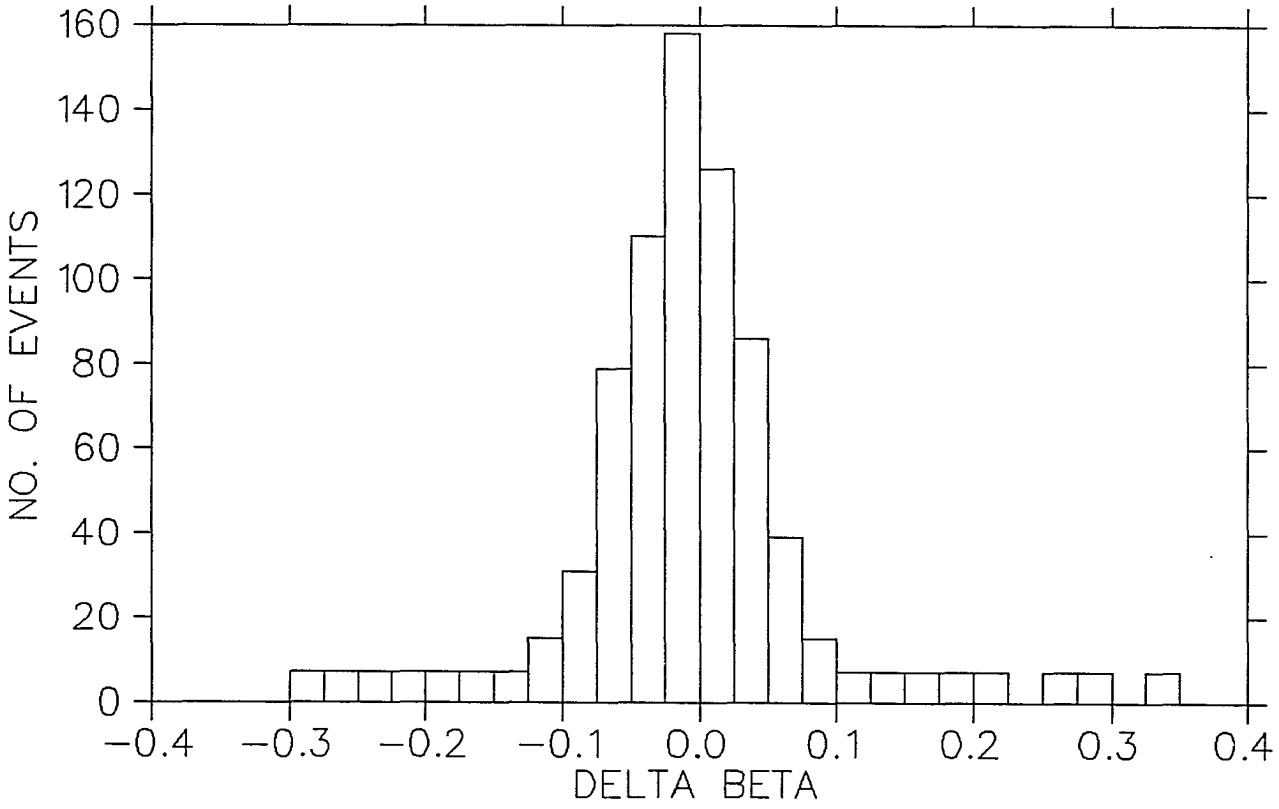

Fig. 35. Delta beta for the 50,000 event subset. Acceptable values of delta beta were within -0.075 and +0.05 for the antiproton analysis.

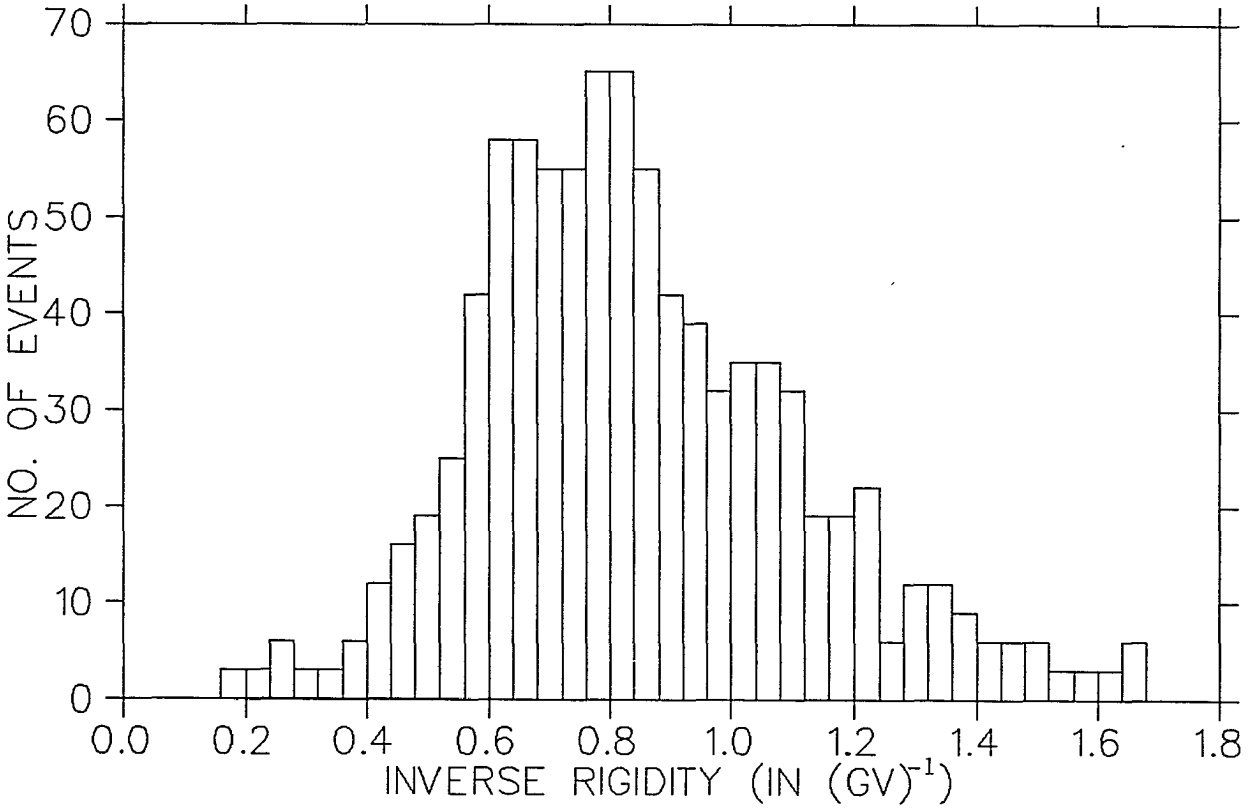

Fig. 36. The inverse rigidities of the 50,000 event subset used for calibration.

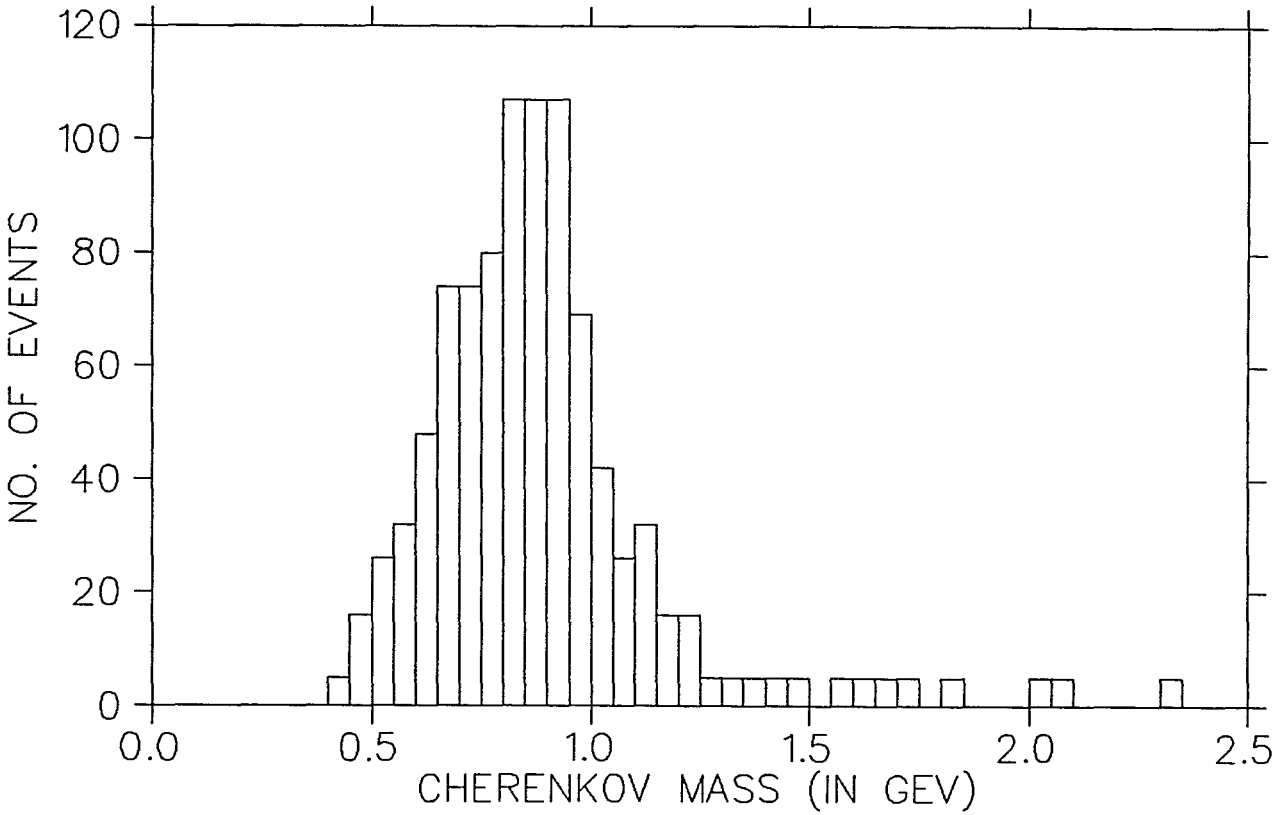

Fig. 37. The mass per unit charge for the 50,000 event subset as calculated from the Cherenkov counter response and the MWPC rigidity. Cut #10 required a calculated mass between 0.4 GeV and 1.25 GeV for the antiproton search. The distribution shown above are events that have already passed cuts #1 through #9.

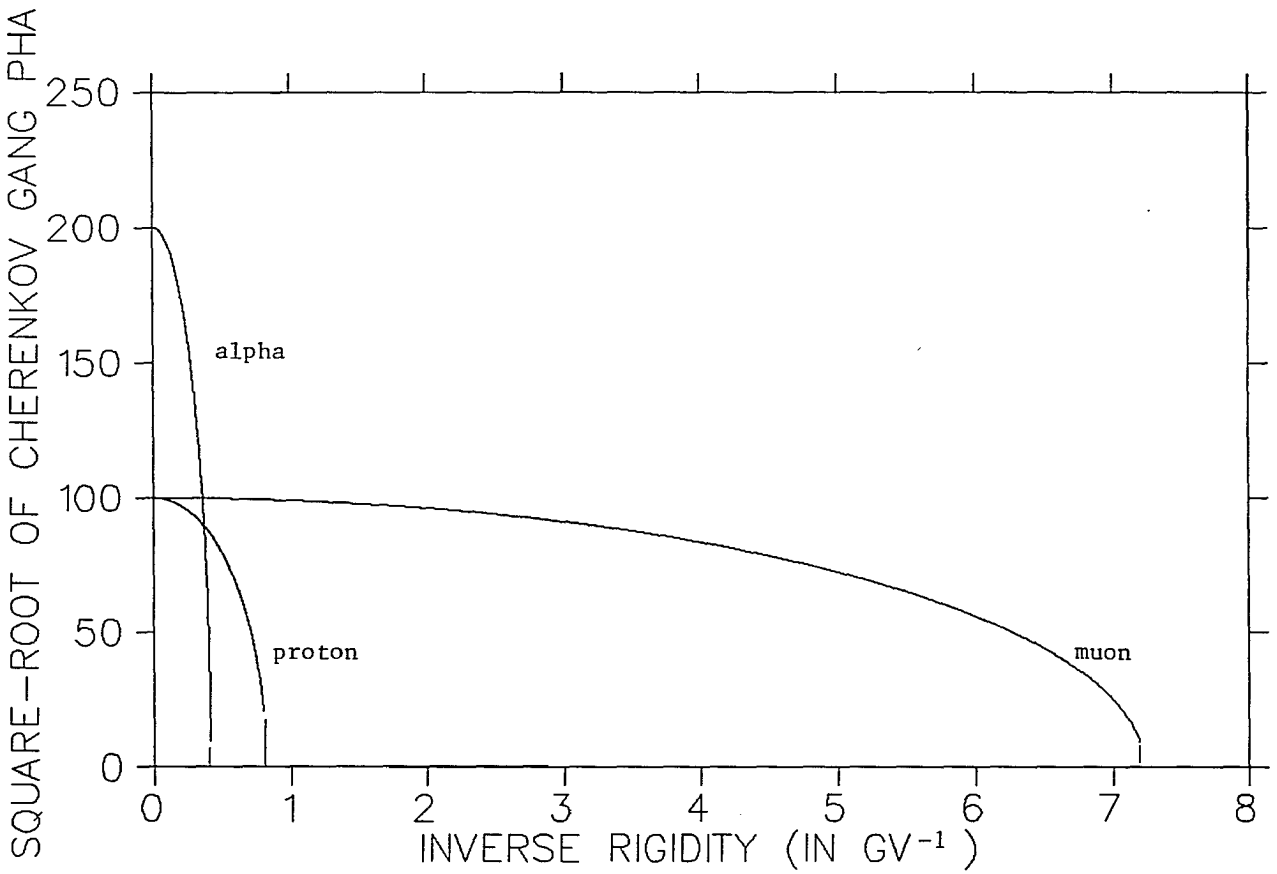

Fig. 38. The theoretical curves for the square-root of the Cherenkov signal as a function of the inverse rigidity. The alpha, proton, and muon ellipses are shown.

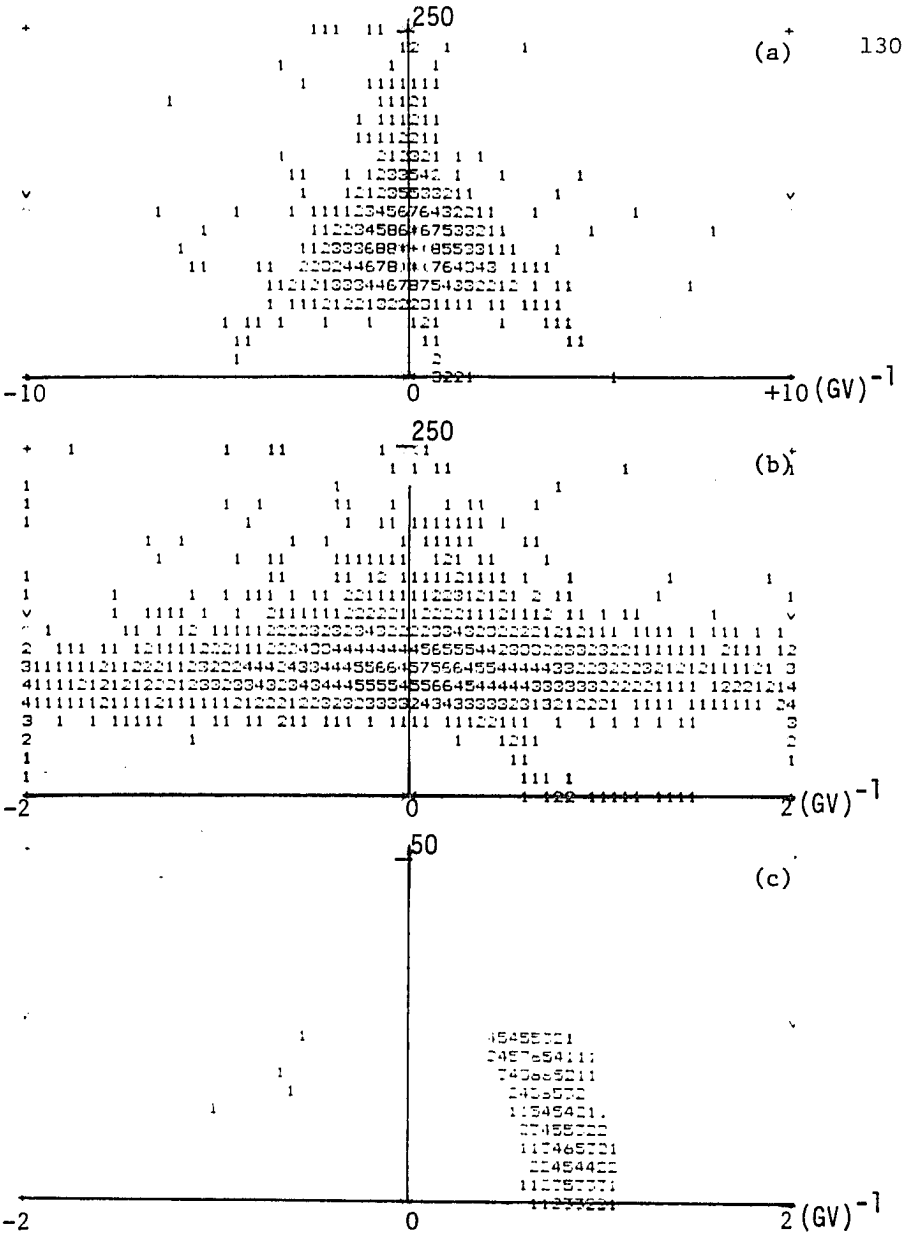

Fig. 39. Ellipses observed during flight and analysis. The x axis is the inverse rigidity. The y axis is the square-root of the Cherenkov gang PHA. (a) and (b) were observed during flight. (c) is the proton and antiproton candidate ellipses after all of the data cuts are taken. Each number represents the square-root of the number of events.

TABLE 2. DAT(500) Array

Location	Contents	Location	Contents
DAT (1-2)	Synch words.	DAT (400)	Pathlength in Cherenkov.
DAT (3)	Frame type.	(401-416)	C PMT PHA-norm. by pathlength.
(4-5)	Event number.	(417)	S2 PMT PHA-norm. by pathlength.
(6-25)	PHA of TOF PMT's.	(418)	Gang Cherenkov PHA-correct.
(26-41)	PHA of Cherenkov PMT's.	(419-424)	Combinations of C PHA's.
(42)	PHA of S1 PMT.	(425)	x in Cher.
(43)	PHA of S2 PMT.	(426)	y in Cher.
(44-63)	TDC output from TOF system.	(428)	x in S2.
(64-87)	TDC output from MWPC's.	(429)	y in S2.
(90)	TDC output from S1.	(430)	Gang C. Pha/ S2.
(91)	TDC output from S2.	(431)	Raw C. gang.
(95)	x at midplane of MWPC chamber 1.	(432-433)	Quadrant info on Cher. counter pos.
(96)	y at midplane of MWPC chamber 1.	(434)	Radial dist. r for Cher.
(97-99)	Fitted direction cosines.	(435)	Radial dist. r for S2.
(100)	Fitted deflection (inverse rigidity).	(436)	Chi-squared of Cher. PMT's.
(101-102)	# of MWPC chambers with good x or y sum.	(437)	Square-root of Cher. gang.
(103)	Chi-squared x from MWPC.	(440)	S1 PHA-corrected.
(104)	Chi-squared y from MWPC.	(441)	x in S1.
(105)	Integral of B.dL.	(442)	y in S1.
(131-138)	Fitted x values of MWPC.	(450)	Abs. value of Beta-rig.
(141-148)	Measured x values.	(453)	Delta beta.
(151-158)	Chi-x of x values.	(476-491)	Cher. PMT PHA -uncorr. with pedestal sub.
(161-168)	Fitted y values.	(499)	Rigidity.
(171-178)	Measured y values.		
(181-188)	Chi-y of y values.		
(191)	Rigidity fit status.		
(300-343)	Time differences and sums for TOF system.		
(344-345)	x and y in top TOF paddles.		
(346-347)	x and y in bottom TOF paddles.		
(350-361)	TOF quantities used in TOF analysis.		
(362)	Beta from TOF.		
(363-364)	Chisquared x and y for TOF system.		
(365)	Beta from rigidity-assuming proton mass.		
(367)	Mass from TOF system.		
(368-399)	Fitting parameters and flags for TOF system.		

TABLE 3. The Five Antiproton Candidate Events.

Event	1/Rig. $(GV)^{-1}$	Square Root of Cher. Gang	Cher. Mass (GeV)	x in Cher. (cm)	y in Cher. (cm)	Beta TOF*
1	-0.984	12.8	0.699	39.6	36.4	0.779
2	-0.576	16.6	1.113	40.6	35.0	0.819
3	-0.536	22.7	0.990	44.7	44.2	0.918
4	-0.678	18.2	0.910	36.1	35.9	0.813
5	-0.570	22.7	0.929	2.3	26.0	0.910

*TOF system is not calibrated to give accurate beta at these energies. Beta here is +/- 0.08.

CHAPTER 7

CONCLUSION

In this last chapter, I will consider the LEAP result and what it indicates about the low-energy antiproton flux in the cosmic-ray spectrum. I will compare our result to that of previous searches, and to a separate antiproton search (titled PBAR) conducted during the same time frame as LEAP and at the same Prince Albert location. I will also compare our results to the expected secondary antiproton spectrum and the spectra of various possible source models discussed in Chapter 4. Thus, LEAP can add its result to the data already collected and contribute to further understanding of galactic antimatter.

7.1. Comparison of LEAP Results to Previous Searches

In the LEAP energy range (below 1.2 GeV), our results for the antiproton/proton ratio is consistent with the upper limit of 3 x 10^{-3} from Rao and Yock (1987) in the 120 -220 MeV range. We are also consistent with the recent results announced by the Bogomolov group (1987). Their stated result of 6 (+14/-5) x 10^{-5} in the 200 MeV - 2 GeV range compares well with our result in the 500 MeV to 1.2 GeV range. Of course, the uncertainty of the Bogomolov group's results is quite large since only one antiproton event was observed, but it is gratifying to note that our result is consistent with theirs.

However, our upper limit of 3.5 x 10^{-5} in the 120 MeV to 360 MeV range is a marked departure from the results of the Buffington group (1981). As discussed in Chapter 2, they observed an antiproton/proton ratio of 2.2 (+/1 0.6) x 10^{-4} in the

130 MeV to 320 MeV energy range. Since both flights originated from the same general area of northern Canada and both were flown during solar minima, the antiproton/proton ratio should have been similar. Although there is a possible 18% change in the antiproton/proton ratio between the two solar minima due to charge-dependent drift in the solar magnetic field (Perko, 1987), this effect would have enhanced the antiproton flux during the LEAP flight. Thus, we are left with a large discrepancy between the two experiments and in no fashion can we view LEAP as having substantiated the surprising result of Buffington, Schindler, and Pennypacker.

7.2. Comparison of LEAP Results to PBAR Results

With this disagreement between Buffington's result and ours, it is fortunate that an independent experiment (Ahlen et al. 1988) was also launched from Prince Albert, Canada, in the summer of 1987. Their measurement would hopefully strengthen one side or the other.

The centerpiece of the PBAR experiment was a superconducting Helmholtz pair magnet and a drift tube hodoscope placed in the fairly uniform 9 kG central field in the bore of the magnet. The drift-tube hodoscope consisted of 323 drift tubes arranged in 8 planes perpendicular to the field and 16 planes parallel to the field. In this spectrometer, each particle could pass through the central field of the magnet without contacting the dewar and have its trajectory determined by the drift-tube hodoscope, revealing the charge sign and rigidity.

The charge and velocity (through time-of-flight analysis) of each particle was determined by two scintillating detectors positioned above and below the spectrometer. Each consisted of three and two 2.54 cm thick segments of fast Bicron

BC420 scintillator, respectively. Each end of each segment was viewed by a PMT connected through a twisted light-pipe.

A 15 centimeter thick water Cherenkov counter was set at the bottom of the experimental stack. Its purpose was very similar to the LEAP Cherenkov counter. In PBAR's case, the higher number of photoelectrons per event in this thicker and much heavier water Cherenkov counter compensated for the higher index of refraction in the water medium n(ref) = 1.33. The photoelectron statistics should allow them to clearly separate protons radiating even more than half the maximum Cherenkov intensity from pions and muons. However, the greater weight of their counter, with its heavily shielded conventional PMT's, contributed to the overall greater weight of the PBAR experiment, limiting the potential length of flight time due to the balloon lifting-weight limits and the need for ballast.

PBAR was launched on August 13, 1987, and enjoyed a 10 hour flight.

The trigger involved a fast trigger, generated by output from both scintillating counters, and an additional slow trigger generated by output from at least one tube in the top two planes and the bottom two planes of the drift tube hodoscope. The cuts performed on their data are presented in (Ahlen et al. 1988). As of this date, the Cherenkov counter has not been included in the data analysis.

They report no antiproton candidates in 52,000 proton tracks. Corrected to the top of the atmosphere, their energy range is reported to be 205 - 640 MeV. After atmospheric and apparatus corrections similar to ours, their 90% confidence level upper limit for the antiproton/proton ratio is 5.5 x 10^{-5}. From a private communication with M. H. Salamon, this upper limit will be pushed down to 3.8 x 10^{-5} based on 75,000 proton candidates in the most recent analysis.

This result is consistent with LEAP and, like LEAP, is at odds with the

results of Buffington, Schindler, and Pennypacker. Since LEAP and PBAR are independent experiments whose results appear to support each other, it is difficult to postulate conditions which would give rise to the Buffington group's high antiproton/proton ratio in this energy range. Thus, in the present absence of theoretical models in which such a short term enhancement of antiproton flux could occur, I conclude that the flux of antiprotons decreases sharply as the particle energy decreases below 1 GeV.

The next step is to compare the LEAP results showing a low antiproton flux to the theoretical predictions presented in Chapters 3 and 4.

7.3. Comparison of LEAP Results to Theoretical Predictions

As discussed in Chapter 3, the conventional model for the cosmic-ray antiproton flux is that of secondary products of high-energy p - p collisions in the interstellar medium. These high-energy protons are at a concentration compatible with the leaky-box model of propagation. Since there are so many uncertainties in the cross sections at these high energies and in the interstellar spectrum of cosmic-rays, the calculated secondary antiproton spectrum varies from author to author (Tan and Ng, 1983; Gaisser, 1982; Stephens, 1980; Szabelski, 1980; Proetheroe, 1981; Webber, 1987).

With these uncertainties in mind, it appears that the LEAP upper limit in the 500 MeV - 1.2 GeV range is compatible with the predictions of all secondary production calculations. I note here that the the results of the Golden and Bogomolov groups at higher energies lie somewhat above most predictions (see Fig. 8). However, the most recent calculation of Webber (1987) does agree with the data from the Golden and Bogomolov groups.

Thus, our present results are consistent with the secondary antiproton picture, with the proviso that there is still some disagreement on the exact predictions of the leaky box model.

Of course, the possibility is still open that there may be a primary antiproton component if the lower secondary flux predictions of other authors prove to be correct. I will now discuss our results in light of the various possible antiproton sources discussed in Chapter 4.

The most popular theories include models in which primordial supersymmetric particles annihilate in galactic halos. In this picture, there are numerous uncertainties such as the mass m_χ, which particle inhabits the halo (Majorana neutrinos, photinos, higgsinos?), their density in the universe, and the branching ratios in the annihilation reactions. With so many adjustable variables, a large number of primary antiproton spectra with both large and small low-energy antiproton fluxes could be proposed. What all of them have in common is a steep decline in the antiproton/proton ratio at some energy greater than 15 GeV which corresponds to the kinematic cutoff in the annihilation process. As of yet, no experimental information is available at those energies.

At lower energies, most authors have been attempting models in which the data of Buffington et al. could be reasonably accomodated. In Chapter 4, I show one model (Rudaz and Stecker, 1988) in which 15 GeV < m_χ < 20 GeV. In that particular model, the UA Cherenkov data at 500 MeV to 1.2 GeV is consistent, but the LEAP data below 500 MeV is not. From LEAP, it appears that there is a steep decline in the antiproton/proton ratio at lower energies which is not found in these models. Thus, although the higher energy data point reasonably fits a number of these models, it appears that the shape of the antiproton/proton ratio does not

favor a large antiproton flux from dark matter annihilations. It will be necessary to restrict such dark matter models to those which do not suggest a substantial low-energy antiproton flux below 500 MeV, as was indicated earlier in the data of Buffington et al..

The closed galaxy model, discussed in Chapter 4, was able to match the antiproton data above 500 MeV fairly well with a judicious choice of f (the fraction of cosmic-ray protons in the old component). However, many authors (Proetheroe, 1981; Stephens, 1981) found it difficult to obtain the needed high flux at the Buffington group's energy range. Various choices of f and $\lambda_{e,o}$ did succeed in fitting Buffington's data. Now, it appears that a high flux at energies below 500 MeV is not needed, and that puts an additional constraint on these unknown parameters. However, there are still so many unknowns that a more definite answer cannot be given.

Our LEAP result of an antiproton/proton ratio upper limit of approximately 2.3×10^{-4} above 500 MeV would be consistent with the baryon - antibaryon symmetric universe model. The null result at lower energies would have to be explained as a result of adiabatic deceleration due to the galactic wind if this picture is to be preserved. However, this is rather uncertain and unwarranted at this time in the light of simpler explanations such as secondary production. A more detailed analysis of this galactic wind modulation is needed in any case. As of present, the best way to investigate this theory would be a search for antihelium (an antialpha/alpha ratio of about 10^{-5} according to Stecker (1987)) which may be possible in future analysis of the LEAP data.

For the neutron - antineutron production in accretion onto compact objects (see Fig. 10), the low flux result definitely is not consistent with the theoretical

predictions. Even including a fair amount of solar modulation, it would be difficult to save such a model. The same can be said for the evaporating primordial black hole model.

Thus, for many of these models to continue being plausible, a strong modulation by the galactic wind would be necessary to explain the low flux of low-energy antiprotons.

It should be noted that most of these models were proposed initially in an effort to explain the unexpectedly large flux as reported by Buffington et al..

However, we have seen that, with a few modifications perhaps, the conventional picture of secondary antiproton production in high energy p - p collisions in the interstellar medium is a satisfactory explanation at present. Thus, without more data, this simpler picture seems to be adequate.

In the future, other surprising results may be reported that support these other possibilities. These include an anti-alpha sighting (baryon-antibaron symmetric universe) or a sharp high energy cutoff in the antiproton/proton ratio (the annihilating supersymmetric particle picture). It is definitely worthwhile to further investigate the antiproton and antimatter cosmic-ray flux.

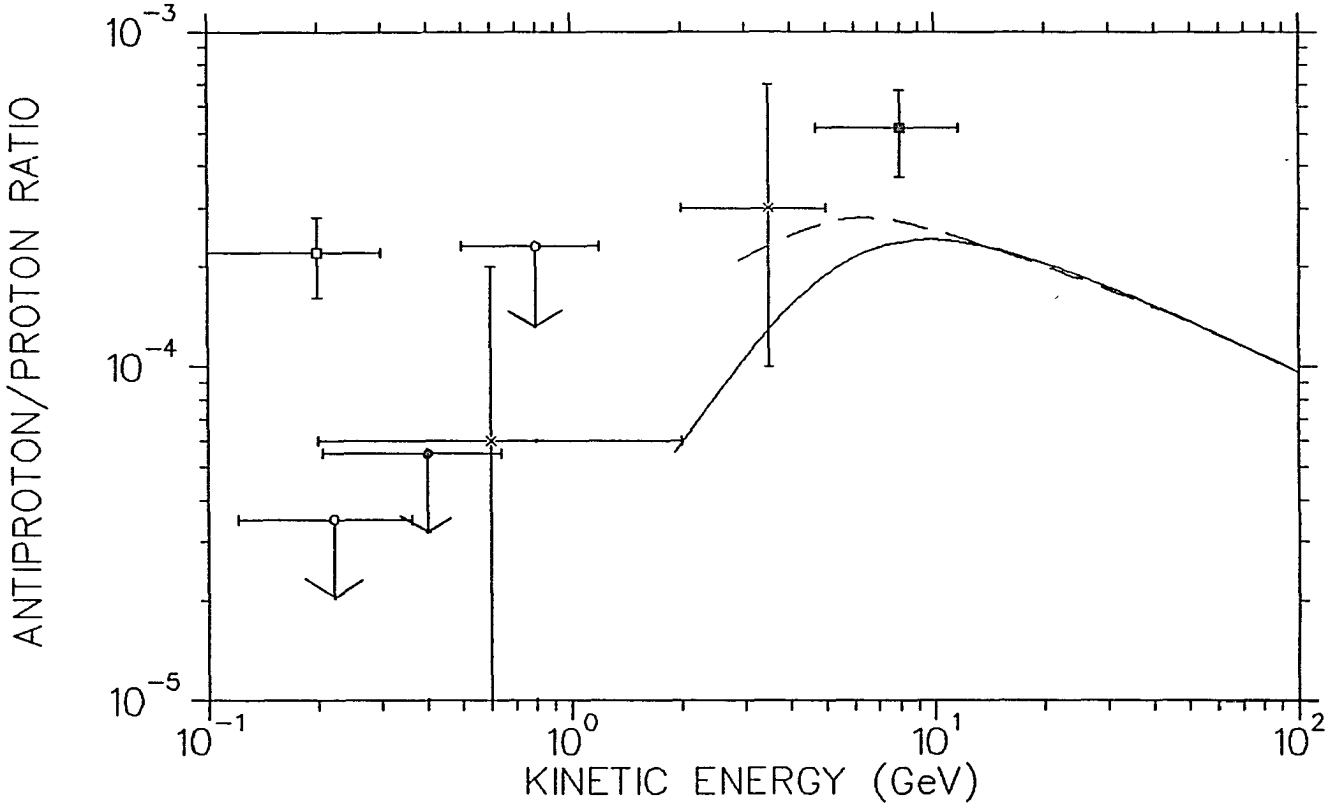

Fig. 40. Experimental measurements of the antiproton/proton ratio as of 1989. The data are from: Golden et al. (1979), filled square; Buffington et al. (1981), open square; Bogomolov et al. (1987), cross; PBAR, filled circle; LEAP, open circle. The solid curve is from Webber (1987), showing the calculated secondary antiproton flux. The dashed curve is from Perko (1987), showing the effect of solar modulation.

APPENDIX A

OPTICAL PROPERTIES OF FC72

In Chapter 5, I stated that I had made measurements of the index of refraction as a function of wavelength $n(\lambda)$ over the visible range and of the absorption coefficient in the visible and ultraviolet range for some candidates for the Cherenkov medium - namely FC72, FC75, FC84, and FC104. Here I will summarize the experimental procedures and results.

A Cary model 14R spectrophotometer measured the absorption coefficient α of these Cherenkov medium candidates. Light in the visible range emitted from a tungsten lamp or the ultraviolet range emitted from an H_2 lamp traveled through a series of monochrometers and was alternatingly directed through either a reference chamber or a sample chamber. The light intensity I_0 of the photons traveling through the empty reference chamber and the intensity I of the photons traveling through the sample chamber, containing a sample of the liquid to be analyzed in a sample cell, is measured with an appropriate visible or ultraviolet detector. When testing the sample in the visible range, the sample cell is glass; in the ultraviolet, the sample cell is necessarily quartz to allow the ultraviolet to pass through the sample cell. In both cases, the total path length through the liquid is one centimeter.

The transmittance T is defined as

$$T = \frac{I}{I_0} = e^{-\alpha t} \tag{A1}$$

where α is the absorption coefficient and t is the path length (equal to one

centimeter in this case). The optical density O.D. is defined as

$$0.D. = \frac{1}{2.3} \alpha t \qquad (A2)$$

In the spectrophotometer, the quantity I/I_0 is measured, a variable slit width compensating for any changes in I_0 due to changes in the intensity emmitted by the lamp itself, while the monochromaters slowly varies the wavelength sent through the chambers. Thus, a scan of the O.D. through wavelength is recorded.

I first measured the optical density of FC72 in the visible range (650 nm to 300 nm) in the glass cell and compared the optical density curve to that of distilled water in the same wavelength range and sample cell. Both appeared to be essentially identical, indicating little absorption in the visible range for FC72. The noise level in runs where nothing was placed in the sample chamber was less than an apparent O.D. of 0.01. In both water and FC72, there appeared to be a baseline absorption level. To test whether that constant loss is due to a reflectance loss from the sample cell walls, I calculated the expected reflectance loss R from each boundary, where

$$R = \left| \frac{n'-n}{n'+n} \right|^2 \quad . \qquad (A3)$$

and n' and n are the indices of refraction on each side of each boundary (normal incidence assumed) (Jenkins and White, 1976). Note that T = 1 - R, so that the expected O.D. is

$$O.D. = -\frac{1}{2.3} \ell n T \qquad (A4)$$

For water, the observed O.D. of 0.045 +/- 0.005, when compared to the calculated O.D. due to reflectance loss of 0.066 +/- 0.03, indicated that the smallest observable O.D. was 0.014. Most of the uncertainty in the calculated O.D. was a consequence of the unknown refractive index of the glass of the sample cell. Similarly, the smallest observable O.D. of the FC72 was 0.025. Thus, I concluded that the absorption coefficient for FC72 in the visible range is less than 0.025. This result was expected since the FC72 appeared colorless and the human eye is quite sensitive to absorption in the visible. I then assumed that all of my FC samples, being equally clear and colorless, did not absorb significantly in the visible region.

I then measured the optical density of water, FC72, FC75, FC84, and FC104 in the ultraviolet range (200 nm $\leq \lambda \leq$ 360 nm), each in the 1 cm thick quartz cell. The noise level was greater (+/- 0.01) but did not affect the results. In each case, the sudden ultraviolet cutoff characteristic of all liquids, in which the O.D. approaches infinity, was not seen for $\lambda \geq$ 200 nm. No absorption band appeared at around 250 nm as seen for FC88 (3M, 1985). In fact, there appears to be little significant absorption at all for $\lambda \geq$ 220 nm. As before, the baseline optical density for all four FC fluids and water from reflectance loss due to the sample cell walls indicated that the smallest measurable O.D. was approximately 0.06.

To measure the index of refraction $n(\lambda)$, I used H, He, and Hg gas-filled tubes as line sources. A model SP200 Spectrum Tube Power supply (5000 volts, 10 Amps) from Electro-Technic Products powered the line sources. The liquid sample was placed in a prism-shaped sample holder which was basically a "cup" with a triangle-shaped cross section. The sides were constructed of microscope-slide glass,

the bottom of aluminum; the container was assembled with quick-drying epoxy. According to information supplied by 3M, none of the FC fluids should react with any of these materials. The three glass side walls met at an approximate 60° angle. The sample holder was placed on the platform of a spectrometer, manufactured by J.W. Queen and Co., which basically consisted of a collimator through which the spectral lines of the line source passed, a swiveling platform on which the sample was placed, and a telescope with which the refracted lines were located. The platform could be rotated about an axis perpendicular to the collimator and telescope axis and the angle through which the telescope was rotated could be measured to the nearest 0.25′ of arc (0.004°).

To measure the index of refraction, the minimum angle of deviation was recorded for each spectral line. First, one angle of the prism-shaped holder was designated as α and the exact value of α was calculated by reflecting light off of the two glass faces composing α and measuring those two angles α_1 and α_2. From the geometry of the setup, the prism angle α was calculated. Then, the sample liquid was placed in the container and placed on the platform. The line source passes through the sample and, by sighting with the telescope and swiveling the platform, the minimum angle of deviation ζ_{min} is recorded for each spectral line. The value of $n(\lambda)$ is then (Jenkins and White, 1976)

$$n(\lambda) = \frac{\sin {}^1/_2(\alpha + \zeta_{min})}{\sin {}^1/_2 \alpha}$$

By using several lines from each source and several different gas sources, a fair number of data points for the curve $n(\lambda)$ could be obtained and plotted.

Of course, the index of refraction is also a function of temperature. Although

I did not control the temperature, I did monitor it with a Copper-Constantan thermocouple with a 0° C reference junction whose voltage was monitored with a Keithley 160B digital voltmeter. For each measurement of n(λ), I determined the average temperature.

I first measured n(λ) for water and compared these points to published data on n(λ). From this comparison, I feel confident that my procedure was correct and that this method yielded accurate results for n(λ).

I then measured n(λ) for FC72, FC75, FC84, and FC104 (see Figs. 41, 42, 43, and 44). On the graphs, the line source used and the temperature range are noted.

An empirical formula for n(λ) is

$$n(\lambda) = A + \frac{B}{\lambda^2} + \frac{C}{\lambda^4} \quad , \tag{A.5}$$

where A, B, and C are material dependent (Jenkins and White, 1976). For each FC fluid, I fitted this function to the data; this function is also shown in Figs. 41, 42, 43, and 44.

When comparing these curves to the data for water (Fig. 45), it is easily seen that for the FC fluids, n(λ) is a relatively weak function of wavelength. This is encouraging, since it appears likely that n(ref) will stay low through a wide range of wavelengths. Also, when comparing these results with the "average" n(ref) published by 3M, it appears my results are consistent for FC72, FC84, and FC104. 3M quoted indices of refraction of 1.251, 1.261, and 1.271, respectively in the visible range at 25° C. However, my results appear too low when compared with 3M's value of 1.276 for FC75. My results for FC75 also appear low when compared to 3M's curve for n(λ) at 20° C and for n(ref) versus temperature at

546.1 nm. At this point, I am not certain where the discrepany arises. It is possible that my sample of FC75 was not pure. However, I am reasonably certain that my other curves are correct.

It was in the end not possible to control the FC fluid temperature precisely, so we made an estimate for the index of refraction as a function of temperature. We set

$$n - 1 \propto \rho \tag{A6}$$

where ρ is the fluid density (n = 1 for vacuum). The coefficient of expansion for FC72 (from 3M) was 0.016 $cm^3/(cm^3\ ^oK)$. For a 10% decrease in temperature, the effective index of refraction n_{eff} at 25° C increased from 1.26 to 1.264.

This effective index of refraction is for the visible and ultraviolet ranges and is calculated by reducing equation (5.6):

$$N = \frac{e^2 \ell}{\hbar c^2} \int_{\beta n>1} \left[1 - \frac{1}{\beta^2 n^2(ref)}\right] d\omega \quad . \tag{A7}$$

Since

$$I \propto N = \frac{e^2}{\hbar c}\, \ell\, \frac{2\pi}{c} \int_{\beta n>1} \left[1 - \frac{1}{\beta^2 n^2}\right] d\nu \quad . \tag{A8}$$

Thus,

$$I \propto \int \left[1 - \frac{1}{\beta^2 n^2}\right] d\nu \quad . \tag{A9}$$

If β = constant,

$$I = (\nu_2 - \nu_1) - \frac{1}{\beta^2} \int_{\nu_1}^{\nu_2} \frac{d\nu}{n^2} \quad . \tag{A10}$$

For n(ref)=n_{eff},

$$I = (\nu_2 - \nu_1) - \frac{1}{\beta^2 n_{eff}^2} \int_{\nu_1}^{\nu_2} d\nu \quad . \tag{A11}$$

Looking at the previous 2 equations,

$$n_{eff} = \left[\frac{1}{\nu_2 - \nu_1} \int_{\nu_1}^{\nu_2} \frac{d\nu}{n^2(ref)} \right]^{-1/2} \quad . \tag{A12}$$

The value of n_{eff} was then found numerically using n(λ) data.

These measurements of the FC fluids were performed to analyze their suitability for a Cherenkov medium for the LEAP experiment. In Chapter 5, I stated the requirements for the Cherenkov detector was a suitable range of refractive indices ($1.10 < n(ref) < 1.27$) over a wide range of wavelengths and a very low absorption coefficient over the sensitive range of a PMT. These requirements arose because of the need to distinguish antiprotons from the large

background flux of negative pions, etc., and the need for a high efficiency in photon emission and collection. As can be seen from my results, all four of the FC fluids tested absorbed very little in the visible and ultraviolet range above 220 nm. In addition, for at least two of them (FC72 and FC84), the index of refraction was in the correct range and varied little over the visible range. After considering the cost and density of these two fluids, FC72 was deemed the most suitable medium for the UA Cherenkov counter.

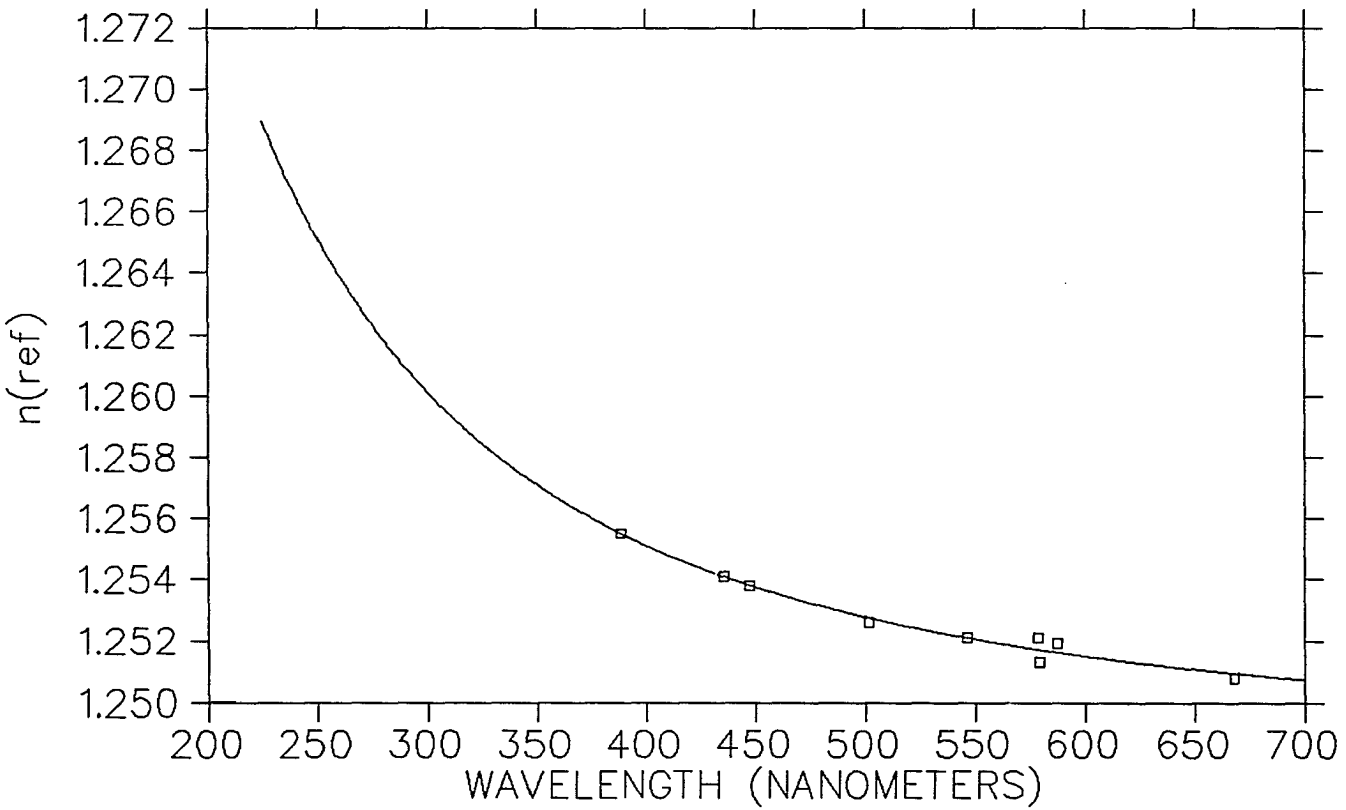

Fig. 41. The index of refraction as a function of wavelength of FC72 at 24.0°C +/- 0.2°C. The experimental data is shown as boxes.

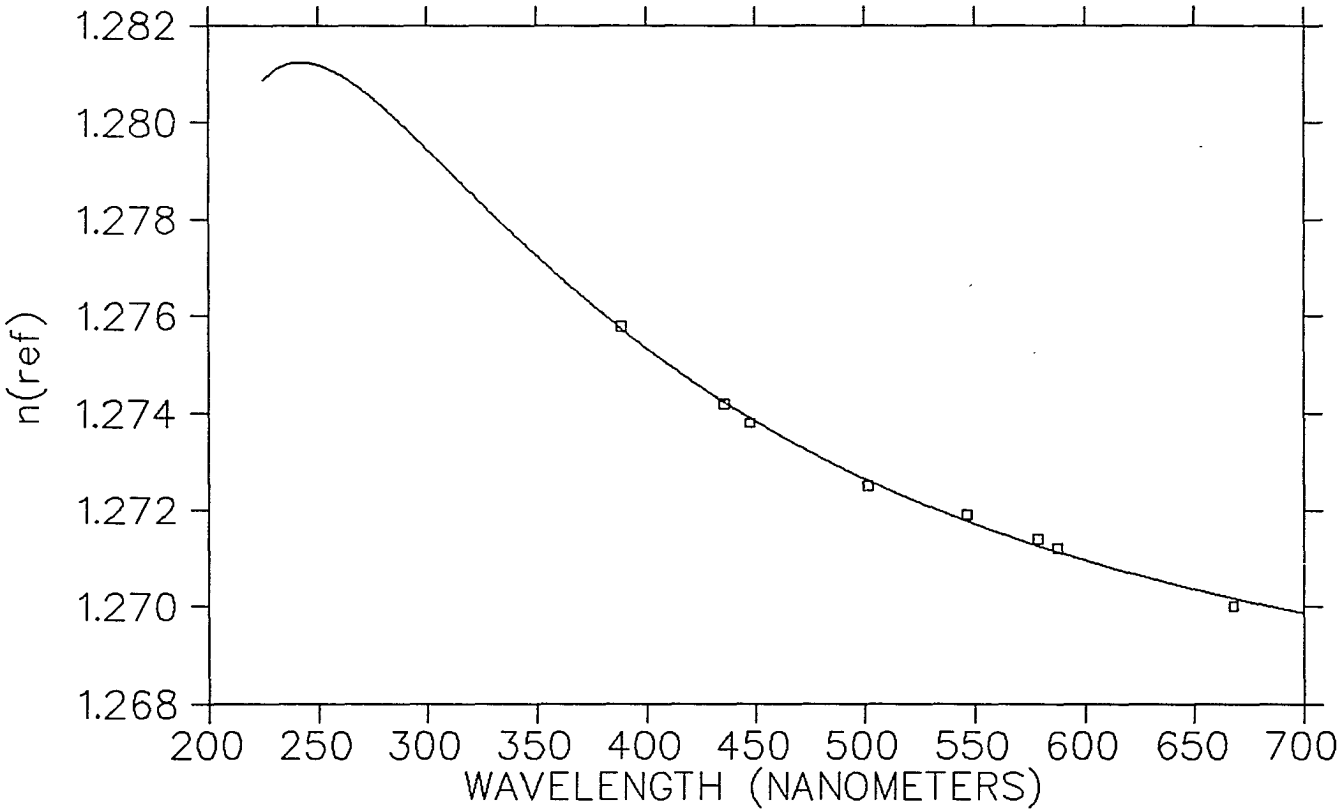

Fig. 42. The index of refraction as a function of wavelength of FC75 at 24.7°C +/- 0.1°C. The dip in the curve below 250 nm is an artifact of the curve fitting.

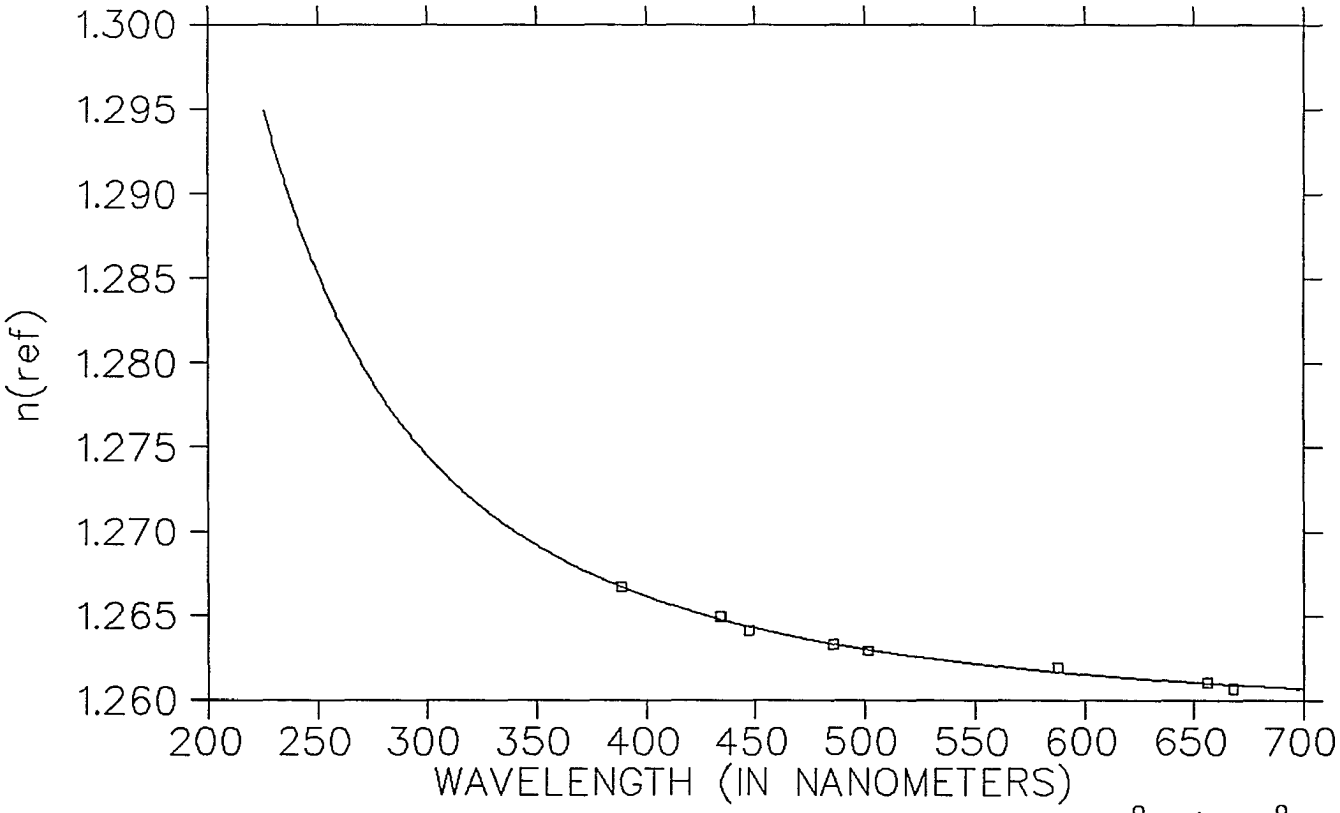

Fig. 43. The index of refraction as a function of wavelength of FC84 at 24.7°C +/- 0.1°C.

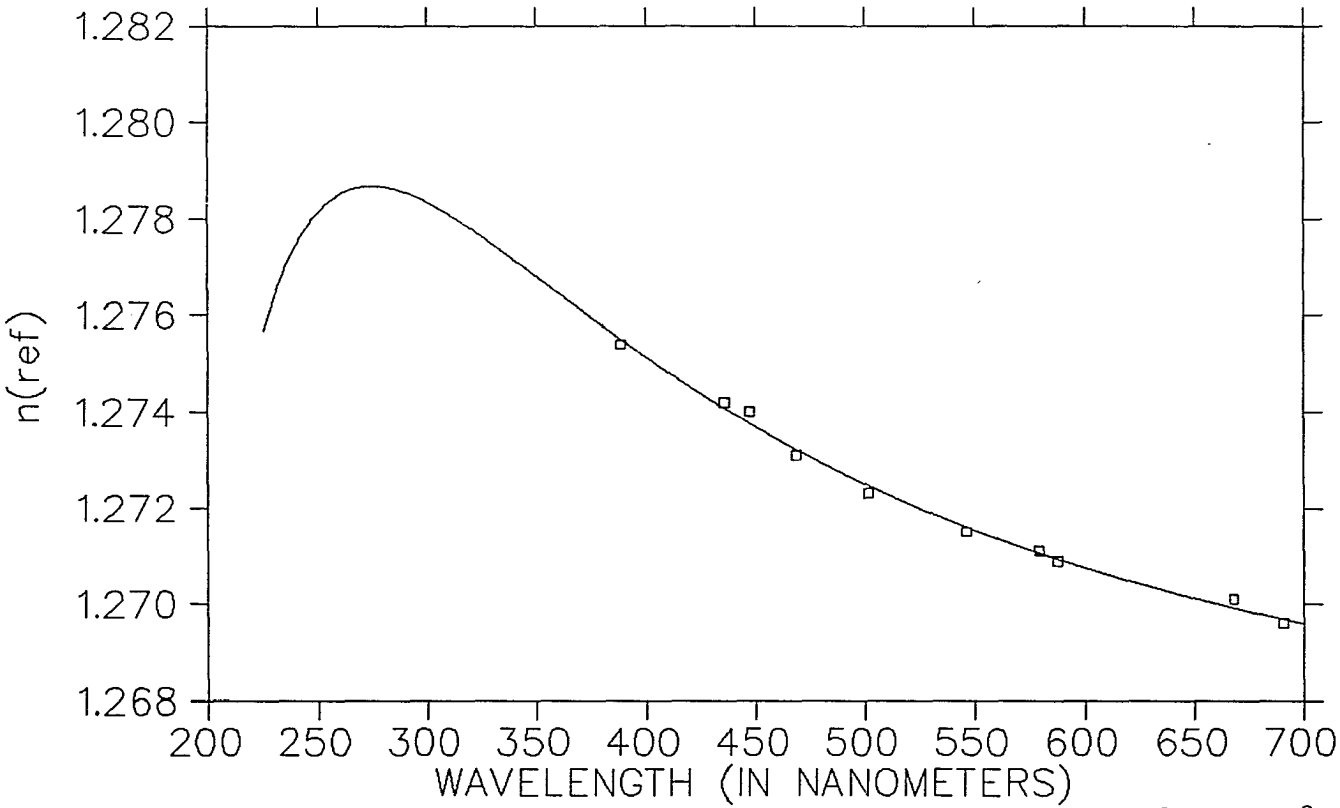

Fig. 44. The index of refraction as a function of wavelength of FC104 at 24.9°C +/- 0.1°C. The decrease in the function for wavelengths less than 250 nm is an artifact of the curve fitting.

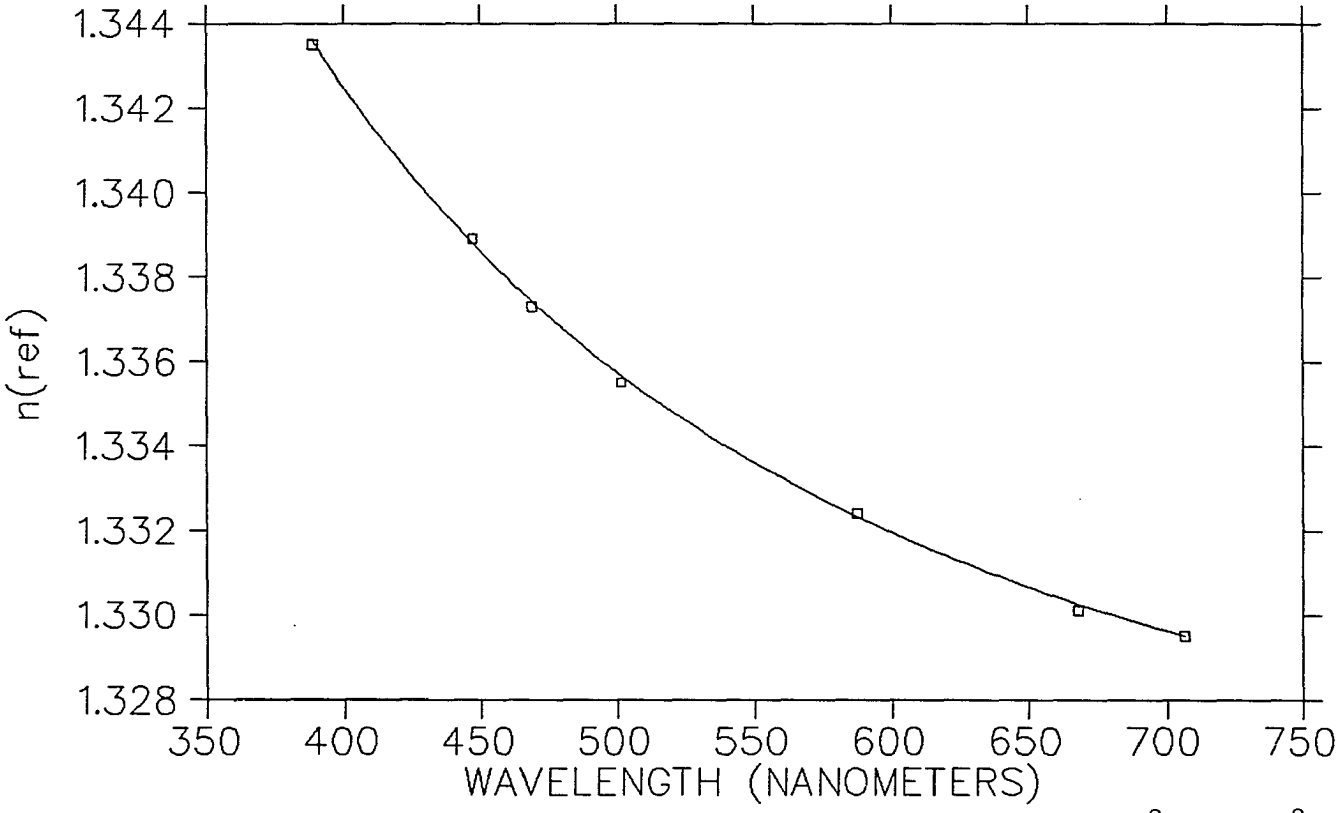

Fig. 45. The index of refraction as a function of wavelength of water at 24.5°C +/- 0.1°C. The experimental data is shown as boxes.

APPENDIX B

MAGNETIC FIELD CALCULATIONS

To position the Hamamatsu R2490-01 PMT's in the magnetic field of the NMSU magnet spectrometer correctly, it was necessary to calculate the magnitude and, more importantly, the direction of the magnetic field in space. It would have been impractical to physically measure $\vec{B}$ at any significant number of points in the experimental region.

These calculations were simplified by the extensive use of non-magnetic materials (aluminum, plexiglas, etc.) in the LEAP experimental stack. The distortions in the magnetic field due to surrounding magnetic materials could then be ignored in these calculations.

For this purpose, the NMSU magnet could be considered a single-turn copper coil with an outer diameter of 0.6096 meters, an inner diameter of 0.3556 meters, and a thickness of 0.0763 meters with a rectangular cross section. This thick coil was designed to carry up to 1.3×10^6 amps-turns.

Since there is no analytical way to calculate the field from a current traveling through a thick coil such as this, I approximated the current I as an array of infinitesimally thin current loops, each of current δI. For this particular calculation, I used 100 current rings of current

$$\delta I = \frac{I}{100} \quad . \tag{B1}$$

These loops of current δI were arranged in an array that approximated the extent in space of the actual thick current loop I.

I then calculated $\vec{B}$ at an observation point P(x,y,z) due to one current loop of

δI. Because of the symmetry of the situation, there is no component of $\vec{B}$ in the $\hat{\phi}$ direction (spherical coordinates are used) and I thus chose to do all of my calculations in the x,z plane. Because of cylindrical symmetry, the magnetic field in all space could be reproduced by rotating the solution in the $x > 0$ and $z > 0$ quarter plane about the z axis (the z axis being the axis of the magnet).

The magnetic field $\vec{B}$ at observation point $P(\vec{\rho})$ due to a current loop of radius a, centered at x=0, y=0, z=0, can be calculated as follows (Jackson, 1975)

$$B_\rho = \frac{2\pi(\delta I)a}{c\rho} \sum_{n=0}^{\infty} \frac{(-1)^n(2n+1)!!}{2^n n!} \frac{r_<^{2n+1}}{r_>^{2n+2}} P_{2n+1}(\cos\theta) \quad , \tag{B2}$$

$$B_\theta = \frac{-\pi(\delta I)a^2}{c} \sum_{n=0}^{\infty} \frac{(-1)^n(2n+1)!!}{2^n(n+1)!!} \alpha P^1_{2n+1}(\cos\theta) \quad . \tag{B3}$$

Here, spherical coordinates are used throughout. The radius of the loop is a; $r_<$ and $r_>$ are the smaller and larger of ρ and a respectively. $P_m(\cos\theta)$ and $P^n_m(\cos\theta)$ are the Legendre polynomial and associated Legendre polynomial. The factor α is the following:

$$\alpha = \begin{cases} \frac{-(2n+2)}{(2n+1)} \frac{1}{a^3} \left[\frac{\rho}{a}\right]^{2n} & \text{for } \rho < a \\ \frac{1}{\rho^3} \left[\frac{a}{\rho}\right]^{2n} & \text{for } \rho > a \quad . \end{cases} \tag{B4}$$

As usual, $\rho = \sqrt{x^2 + z^2}$ and $\cos\theta = (z/\rho)$.

In the numerical code, I noted that (Arfken, 1970)

$$P_0(x) = 1 \tag{B5}$$

$$P_1(x) = x \tag{B6}$$

and used

$$P_{n+1}(x) = 2xP_n(x) - P_{n-1}(x) - \frac{[xP_n(x) - P_{n-1}(x)]}{n+1} \tag{B7}$$

and

$$P^1_{2n+1}(x) = (-1)(1-x^2)^{1/2} \frac{d}{dx} P_{2n+1}(x) \tag{B8}$$

$$\left[\text{where } \frac{dP_{2n+1}(x)}{dx} = (2n+1)\, P_{2n}(x) + x \frac{dP_{2n}(x)}{dx} \text{ and } \frac{dP_1(x)}{dx} = 1\right]$$

to calculate values for the Legendre and associated Legendre polynomials in an iterative process for each value of cos(θ).

In actuality, I could not calculate the full series to n = ∞ so I used an adjustable parameter for the number of terms n and tested the convergence of the series by trying different values of n_{final}. Thus, I actually used the series

$$\beta_\rho \cong \sum_{n=0}^{n=n_{final}} \cdots ,$$

In most cases, n_{final} = 10 was sufficient for these purposes; results varied by less than 1% in both magnitude and direction when n_{final} = 10 and n_{final} = 20.

I then calculated the magnetic field due to the current loops of varying radii a and various values of z of the current-loop array and added these 100 values of $\vec{B}$ vectorially at the point P. Thus, a final magnitude $|\vec{B}_x|$, $|\vec{B}_z|$, and

$$| \vec{B} | = \sqrt{B_x^2 + B_z^2} \tag{B9}$$

can be calculated for observation point P.

Thus, for any point observation point P(x,y,z), we could calculate the expected magnitude and direction of the magnet's field by calculating the distance from the observation point P and the magnet center and the angle θ between the magnet axis $\vec{z}$ and $\vec{\rho}$.

This calculation is accurate to any distance, barring any field distortion due to magnetic materials or the influence of the earth's 1/2 gauss magnetic field. However, these results necessarily are not accurate within the actual coil since then the δ I loops typically behave as a delta function and the above equations are no longer accurate or analogous to the physical situation.

REFERENCES

1. Ahlen, S. P., Barwick, S., Beatty, J. J., Bower, C. R., G. Gerbier, G., Heinz, R. M. Lowder, D., McKee, S., Mufson, S., Musser, J. A., Price, P. B., Salamon, M. H., Tarle, G., Tomasch, A., and Zhou, B. 1988, (submitted to Phys. Rev. Letters.).

2. Apparao, K. M. V. 1967, Nature, 215, 727.

3. Apparao, K. M. V., et al. 1986, Proc. 19th Internat. Cosmic Ray Conf. (La Jolla, CA), 2, 326.

4. Arfken, G. 1970, Mathematical Methods for Physicists, (Academic Press, Inc., N. Y.) 534.

5. Barber, H. B., Bowen, T., Delise, D. A., Jenkins, E. W., Jones, J. J., Kalback, R. M., and Pifer, A. E. 1980, Phys. Rev. D., 22, 2667.

6. Bellettini, G., Cocconi, G., Diddens, A. N., Lillethun, E., Matthiae, G., Scanlon, J. P., and Wetherell, A. M. 1966, Nucl. Phys., 79, 609.

7. Bogomolov, E. A., et. al. 1979, Proc. 16th Internat. Cosmic Ray Conf. (Kyoto), 1, 330.

8. Bogomolov, E. A., Lubyanaya, N. D., Romanov, V. A. 1971, Proc. 12th Internat. Cosmic Ray Conf., 5, 1730.

9. Bogomolov, E. A., Vasilyev, G. I., Krut'kov, S. Yu., Lubyanaya, N. D., Romanov, V. A., Stepanov, S. V., and Shulakova, M. S. 1987, Proc. 20th Internat. Cosmic Ray Conf. (Moscow), 2, 72.

10. Bowen, T., and Moats, A. 1986, Phys. Rev. D., 33, 3, 651.

11. Bruge, G. 1984, Symposium on Nucl. Spectroscopy and Nucl. Interactions (Osaka), report D Ph-N-Saclay No. 2136 (unpublished).

12. Buffington, A., Schindler, S. M., and Pennypacker, C. R. 1981, Ap. J., 248, 1179.

13. Caldwell, T. H. 1977, Ap. J., 218, 269.

14. Carr, B. J. 1976, Ap. J., 206, 8.

15. Carter, B., et al. 1976, Astr. Astrophys., 52, 427.

16. Clover, M. R., DeVries, R. M., DiGiacomo, N. J., and Yariv, Y. 1982, Phys. Rev. C., 26, 2138.

17. Clover, M. R., McGaughey, P. L., and Yariv, Y. 1988, private

communication.

18. Cowsik, R., and Gaisser, T. K. 1981, Proc. 17th Internat. Cosmic Ray Conf. (Paris), 2, 218.

19. Cowsik, R., and Wilson, L. 1975, Proc. 14th Internat. Cosmic Ray Conf. (Munich), 2, 659.

20. Dermer, C. D., and Ramaty, R. 1986, Nature, 319, 6050, 205.

21. Dermer, C. D., and Ramaty, R. 1986, Proc. VIth Moriond Astrophys. Meeting, .

22. DiGiacomo, N. J., DeVries, R. M., and Peng, J. C. 1980, Phys. Rev. Letters, 45, 527.

23. Eichler, D. 1982, Nature, 295, 391.

24. Englemann, J. J., et al. 1983, Proc. 18th Internat. Cosmic Ray Conf. (Bangalore), 2, 17.

26. Flaminio, V., Moorhead, N. G., Morrison, D. R. O., and Rivoire, N. 1984, CERN-HERA Report No. 84-01.

27. Gaisser, T. K. 1982, Proc. 2nd Moriond Astrophys. Meeting (Les Arcs, France).

28. Gaisser, T. K., and Levy, E. H. 1974, Phys. Rev. D., 10, 6, 1731.

29. Gaisser, T. K., and Mauger, B. G. 1982, Ap. J., 252, L57.

30. Gaisser, T. K., and Maurer, R. H. 1973, Proc. 13th International Cosmic Ray Conf. (Colorado), 1, 562.

31. Glashow, S. L. 1961, Nucl. Phys., 22, 579.

32. Golden, R. L. 1985, Particle Astrophysics Laboratory Description.

33. Golden, R. L. 1987, LEAP Configuration Guide, Particle Astrophysics Laboratory, New Mexico State University (Las Cruces, NM).

34. Golden, R. L., Badhwar, G. D., Lacy, J. L., and Zipse, J. E. 1978, Nucl. Instrum. Methods, 148, 179.

35. Golden, R. L., Horan, S., Mauger, B. G., Badhwar, G. D., Lacy, J. L., Stephens, S. A., Daniel, R. R., and Zipse, J. E. 1979, Phys. Rev. Letters, 43, 16, 1196.

36. Golden, R. L., Mauger, B. G., Nunn, S., and Horan, S. 1984, Ap. J. (Letters), 24, 75.

37. Grum, F., and Luckey, G. W. 1968, App. Optics, 7, 2289.

38. Hagelin, J. S., and Kane, G. L. 1986, Nucl. Phys. B263, 399.

39. Hawking, S. W. 1974, Nature, 248, 30.

40. Hillas, A. M. 1983, in Proceedings of the Cosmic Ray Workshop, Univ. Of Utah, Jan. 1983, ed. T. Gaisser (Bartol Research Foundation, Newark, DE).

41. Jackson, J. D. 1975, Classical Electrodynamics, 2nd ed. (John Wiley and Sons, N. Y.), 638-641.

42. Jelley, J. V. 1958, Cerenkov Radiation and its Applications, (Pergamon Press, Inc., U. K.) 1-31.

43. Jenkins, F. A., and White, H. E. 1976, Fundamentals of Optics, (McGraw-Hill, Inc., U. S. A.), 526.

44. Jokipii, J. R. 1985, private communication.

45. Juliusson, E. 1974, Ap. J., 191, 331.

46. Julliusson, E., Meyer, P., and Müller, D. 1972, Phys. Rev. Letters, 28, 926.

47. Khazan, Y. M., and Ptuskin, V. S. 1977, Proc. Internat. Cosmic Ray Conf. (Plovdiv), 2, 4.

48. Kiraly, P., Szabelski, J., Wdowczyk J., and Wolfendale, A. W. 1981, Nature, 293, 120.

49. Ormes, J. F., and Protheroe, R. J. 1983, Ap. J., 272, 756.

50. Page, D. F., and Hawking, S. W. 1976, Ap. J., 206, 1.

51. Particle Data Group, 1986, Phys. Letters, 170B.

52. Perko, J. S. 1987, NASA preprint 87-012 (submitted to Astron. and Astrophys. (Letters)).

53. Peters, B., and Westergaard, N. J. 1977, Astrophys. Space Science, 48, 21.

54. Protheroe, R. J. 1981, Astrophys. J., 206, 1.

55. Rao, A. C. R., and Yock, P. C. M. 1987, Europhys. Letters, 3, 9, 1049.

56. Rudaz, S., and Stecker, F. W. 1988, Ap. J., 325, 16.

57. Salam, A. 1968, in Elementary Particle Theory, ed. N. Svartholm

(Almquist and Forlag, Stockholm), 367.

58. Sembroski, G. H., Bowen, T., Jenkins, E. W., Jones, J. J., and Pifer, A. E. 1986, Phys. Rev. D., 33, 639.

59. Shai, C. M., and Schutt, J. B. 1971, Goddard Space Flight Center Print, X-762-71-266.

60. Silk, J., and Srednicki, M. 1984, Phys. Rev. Letters, 53, 624.

61. Simon, M., Spiegelhauer, H., Schmidt, W. K., Siohan, F., Ormes. J. F., Balasubrahmanyan, V. K., and Arens, J. F. 1980, Ap. J., 239, 712.

62. Smith, L. H., Buffington, A., Smoot, G. F., Alvarez, L. W., and Wahlig, M. A. 1973, Ap. J., 180, 987.

63. Stecker, F. W. 1981, Ann. N. Y. Acad. Sci., 375, 69.

64. Stecker, F. W. 1987, Proc. of the Antimatter '87 Internat. Symp. (Karlsruhe, Fed. Rep. Germany) in press.

65. Stecker, F. W. 1988, Phys. Letters B., 201, 4, 529.

66. Stecker, F. W., Rudaz, S., and Walsh, T. F. 1985, Univ. of Minnesota print UMN-TH-520/85.

67. Stecker, F. W., and Wolfendale, A. W. 1984, Nature, 309, 37.

68. Stephens, S. A. 1981, Astrophys. and Space Science, 76, 87.

69. Streitmatter, R., and Stochaj, S. 1987, private communication.

70. Streitmatter, R. E., Stochaj, S. J., Ormes, J. F., Golden, R. L., Stephens, S. A., Bowen T., Moats, A., and Lloyd-Evans, J. L. 1989, Advances in Space Research, in press.

71. Streitmatter, R. E., et. al. 1982, NASA preprint 1982, presented at the Washington APS Metting, April, 1982.

72. Szabelski, J., Wdowczyk, J., and Wolfendale, A. W. 1981, Nature, 285, 386.

73. Szabelski, J., and Wolfendale, A. W. 1986, private communication.

74. Tan, L. C., and Ng, L. K. 1981, J. of Phys. G: Nucl. Phys., 7, 123.

75. Tan, L. C., and Ng, L. K. 1983, J. Phys. G: Nucl. Phys., 9, 227.

76. 3M Product Manual: Fluorinert Electronic Liquids, 1985, Commercial Chermical Division/3M.

77. Viehmann, W., and Frost, R. L. 1979, Nucl. Instr. and Methods, 167, 405.

78. Webber, W. R. 1987, Proc. 20th Internat. Cosmic Ray Conf. (Moscow), 2, 80.

79. Weinberg, S. 1967, Phys. Rev. Letters, 19, 1264.